Improvements in Numerical Modeling Methodology of Dry Woven Fabrics for Aircraft Engine Containment Systems

by

Jonathan Fein

A Thesis Presented in Partial Fulfillment
of the Requirements for the Degree
Master of Science

Approved April 2012 by the
Graduate Supervisory Committee:

Subramaniam Rajan, Chair
Hanqing Jiang
Barzin Mobasher

ARIZONA STATE UNIVERSITY

December 2012

ABSTRACT

Woven fabric composite materials are widely used in the construction of aircraft engine fan containment systems, mostly due to their high strength to weight ratios and ease of implementation. The development of a predictive model for fan blade containment would provide great benefit to engine manufactures in shortened development cycle time, less risk in certification and fewer dollars lost to redesign/recertification cycles. A mechanistic user-defined material model subroutine has been developed at Arizona State University (ASU) that captures the behavioral response of these fabrics, namely Kevlar® 49, under ballistic loading.

Previously developed finite element models used to validate the consistency of this material model neglected the effects of the physical constraints imposed on the test setup during ballistic testing performed at NASA Glenn Research Center (NASA GRC). Part of this research was to explore the effects of these boundary conditions on the results of the numerical simulations. These effects were found to be negligible in most instances.

Other material models for woven fabrics are available in the LS-DYNA finite element code. One of these models, MAT234: MAT_VISCOELASTIC_LOOSE_FABRIC (Ivanov & Tabiei, 2004) was studied and implemented in the finite element simulations of ballistic testing associated with the FAA ASU research. The results from these models are compared to results obtained from the ASU UMAT as part of this research. The results indicate an underestimation in the energy absorption characteristics of the Kevlar

49 fabric containment systems. More investigation needs to be performed in the implementation of MAT234 for Kevlar 49 fabric.

Static penetrator testing of Kevlar® 49 fabric was performed at ASU in conjunction with this research. These experiments are designed to mimic the type of loading experienced during fan blade out events. The resulting experimental strains were measured using a non-contact optical strain measurement system (ARAMIS).

DEDICATION

To my family…

ACKNOWLEDGMENTS

First off I would like to thank my family, as without all of their support this work would not have been possible. I would like to thank my advisor, Dr. Subby Rajan for the opportunity to work on this project and for all of the support throughout graduate school. I would also like to thank the other members of my graduate committee, Dr. Barzin Mobasher and Dr. Hangqin Jiang for their feedback and guidance in preparing this report. My appreciation also goes out to the laboratory staff at ASU, namely Peter Goguen and Dallas Kingsbury, KC, Masoud and Joel at the AIMS lab for their knowledge and for letting me in the door. Thank you to Duane Revilock and Mike Peiriera at NASA Glenn Research Center for your support with the ARAMIS system and for all of your hard work on this project. Lastly, my thanks goes out my fellow graduate students for all of their support and assistance.

Table Of Contents

Page

CHAPTER Page

CHAPTER Page

LIST OF TABLES

Table Page

Table Page

Table Page

Table Page

LIST OF FIGURES

Figure Page

Figure Page

Figure Page

1 INTRODUCTION

In today’s highly competitive economic climate, the trend in product design is to create higher quality, lower cost products faster and more reliably. These stringent customer requirements cannot be met utilizing the design principles from decades past. The need for predictive tools in the design cycle is becoming ever apparent. The ability to determine a performance of a proposed design prior to prototyping and testing results in a shortened research and development cycle and a decreased risk of performance failure. This ultimately means less testing during development, fewer failed certification tests and less redesign work, allowing for faster product delivery at a reduced cost to the manufacturer.

In response to expressed industry demand, research has been conducted at Arizona State University (ASU) to develop a user defined material model for dry woven fabrics. This model is intended for use in predictive simulations of aircraft engine fan blade containment system performance during a fan blade out (FBO) event. The research detailed in this report was conducted to validate and improve this material model.

1.1 Project Motivation and History

1.1.1 FAA Project Motivation

Dry woven fabrics such as Kevlar® (DuPont) are widely used in aircraft propulsion engine fan blade containment systems due to their high tensile strength to weight ratios and good flexibility. Kevlar® belongs to the Aramid family of materials. The term Aramid is assigned to the Aromatic Polyamides, referring to the structure of this family of materials, which consist of long, highly axially oriented chains of polyamides attached to aromatic rings. This structure is obtained through a spinning process, where short chains of polymers are drawn through a solvent bath into a spinnarette, where the long chain structure is formed. This orientation creates the highly isotropic behavior of these materials, being much stiffer in the axial direction than the transverse direction (Chawla, 2011). Engine fan blade containment structures are designed to prevent an engine fan blade from penetrating the fan casing structure and compromising the integrity of the aircraft fuselage in the event of a FBO event.

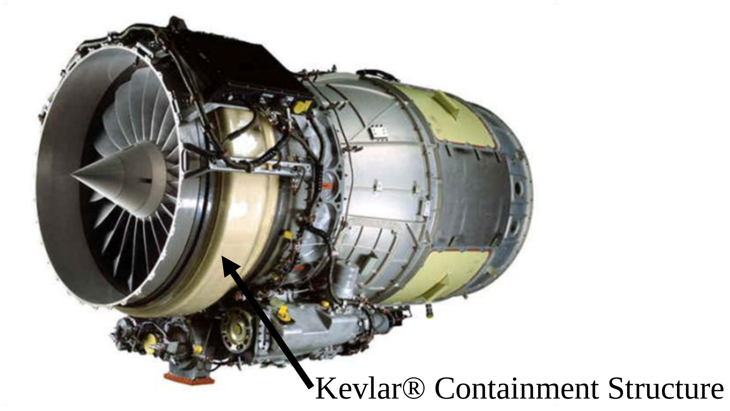

Figure 1. Honeywell HTF7000 Turbofan Engine

The Federal Aviation Administration (FAA) requires that each new turbofan engine successfully passes a containment system certification test prior to release for use. These tests are expensive to develop and perform while, due to the high velocity and high variability of the impact loading, the risk of non-compliance is elevated for anything less than A conservative containment system design. Due to these high cost and risk issues, and in response to industry interest, the FAA's Aircraft Catastrophic Failure Prevention Program funded research to develop a robust, reliable predictive methodology to determine the performance of a woven fabric composite engine containment system prior to destructive testing. The research initiative formed was a joint effort involving ASU, Southwest Research Institute (SRI), Honeywell Aerospace and the National Aeronautics and Space Administration's Glenn Research Center (NASA GRC) and consisted of both experimental testing and numerical simulations using the explicit finite element code LS-DYNA. The project was divided into three (3) distinct phases. The intent and results of each phase are outlined below.

1.1.2 FAA Project History

1.1.2.1 Phase I

Phase I of the FAA project was a collaborative effort between ASU, SRI, NASA GRC and Honeywell Engines. The work performed in association with this Phase included;

- Mechanical Testing (ASU) (Rajan, et al. 2004) : Static mechanical testing of Kevlar® 49 and Zylon AS composite fabrics was performed to characterize the response of these materials under load. Static tension testing was performed to determine the response of the fabric in the principal directions under tensile load. Static penetrator testing was performed to quantify the behavior of woven fabric materials under penetrator type loading.
- Ballistic Testing (NASA GRC) (Pereira, et al., 2004): Ballistic testing of both Kevlar® 49 and Zylon AS materials was performed at NASA GRC.

The intent of this testing was to simulate an engine containment structure under the loading experienced during a fan blade out event.

- Material Modeling Development (SRI) (Simmons, et al., 2004): Using the results from the mechanical testing, a mechanistic based material model was developed at SRI that attempted to capture the fabric material behavior for use in the explicit non-linear finite element code LS-DYNA for use in engine fan blade out simulations. Results from the static penetrator testing and the ballistic testing were used in validating the accuracy and robustness of the material model.
- Engine Simulations (Honeywell Engines)(Gomuc, 2004) : Full scale engine fan blade out finite element simulations were prepared at Honeywell Engines implementing the material model developed at SRI. The results from these models were compared against results from engine fan blade out testing for validation.

1.1.2.2 Phase II

Work associated with Phase II of the FAA project included:

- Improvements to Material Modeling (Rajan, et al. 2009) Adjustments were made to the response of Kevlar® 49 and Zylon AS to improve the predictive capability of the material model for these fabrics.
- Multilayer modeling: The ability to perform multilayer finite element simulations was achieved as part of Phase II. Previous models utilized one layer of shell elements to represent all fabric layers, ignoring the

effect of the interaction between the fabric layers (mainly friction) on the FE model results.

- 1500D Zylon Characterization: Efforts were made to characterize the behavior of 1500D Zylon fabric and compare these results with Kevlar® 49. Previous studies on Zylon fabric showed promising results, indicating a substantial increase in the strength to weight ratio when compared to Kevlar® fabric. Results from this study showed a marked deterioration of the strength properties of Zylon with humidity and temperature. It was determined to focus all future research efforts on Kevlar® fabric.
- Full Scale Engine Simulations: Additional engine simulations were performed utilizing the improved material model. The FE model results were compared against the engine hardware data.
- Ballistic Testing (NASA GRC)(Revilock, et al., 2007): Ballistic testing of both Kevlar® 49 and Zylon AS materials was performed at NASA GRC. The ballasting testing associated with Phase II varied from the testing performed in Phase I in both projectile velocity and orientation.

1.1.2.3 Phase III

All current work being performed on the FAA project is associated with Phase III. Phase III work performed to date includes:

- Mechanical Testing: Additional mechanical testing was performed in an attempt to more accurately capture the behavior of Kevlar® 49 fabric. Static tension tests were run and compared to previous results. Picture frame shear testing was performed to capture the response of the fabric to shear deformation loading. High strain rate testing was performed to validate assumptions made regarding the effect of elevated strain rates on the fabric response. Single yarn testing, yarn pullout testing and fabric geometry studies were performed in support of the development of a micromechanical material model. Additional ballistic testing was performed at NASA GRC and the results were added to the ballistic test results from previous phases (Bansal, 2007)(Vaidya, 2010)(Zhu, 2009).

- FE Modeling: Improvements made to the numerical simulations included the determination of the effect the modeled fabric wrapping scheme on the accuracy of the model (both spiral and concentric fabric configurations were considered). Sensitivity studies were performed on various parameters to determine their effect on the FE model results. A micromechanical model was developed modeling the interaction between the fabric yarns and the evolution of the fabric geometry during loading (Vaidya, 2010).

1.1.2.4 Thesis Objectives

The first portion of this report explores the effects that the simulation of physical boundary conditions has on the results of finite element simulations of ballistic testing of Kevlar® 49 fabric. The second portion of this report compares the results from FE simulations of the NASA GRC ballistic testing utilizing the user defined material model UMAT48 developed at ASU to the results from the same models when utilizing another material model for dry woven fabric, MAT234(Ivanov, et al., 2004). Finally, static penetrator testing of Kevlar® 49 fabric was performed at ASU and the resulting strains were measured using a non-contact optical strain measurement system.

2 STATIC TENSION TESTING

2.1 Overview

In May 2010, a series of static tension tests were conducted on samples of dry woven fabric including Kevlar® 49 and Kevlar® 149 fabric. All tests were performed on a 22 kip servo-hydraulic load frame under closed-loop conditions. The load/deflection curves of the fabrics were recorded and utilized in determining the stress strain response of the fabrics. Tests were performed in the warp and fill directions to determine E_{11} and E_{22}, respectively.

2.1.1 Specimen Details

2.1.1.1 Material Properties

Material properties for the materials Kevlar® 49, Kevlar® 149 and Goldflex (another woven fiber composite material) were determined using both direct measurement techniques and through derivation using known material properties. The basic material properties are listed below in Table 1.

Table 1: Basic Material Properties

Material	Ave. Thickness (in)	Areal Density (psi)	c/s Area (sq in)
Kevlar® 49	0.0030	1.60E-05	0.0061
Kevlar® 149	0.0054	2.96E-05	0.0107
Goldflex	0.0088	3.43E-05	0.0175

Calipers were used to determine the average thickness of each material. Five samples were measured at three locations on each sample (one in the middle and at each end). To calculate the areal density of the materials, fabric samples of known size were prepared and measured. The mass of these samples was then determined on a scale. The Areal Density is calculated using Equation 1 below.

$$Areal\ Density = m/(lw) \tag{1}$$

where m is the mass of the sample, l is the measured length and w is the measured width. The values reported in the in Table 1 represent the average determined values for the five samples. The cross sectional area of the samples was calculated by Equation 2 below.

$$A = m/(\rho l) \tag{2}$$

where A is the cross sectional area, m is the sample mass, ρ is the density of the material and l is the sample length, measured with a ruler.

2.1.1.2 Specimen Nomenclature

Samples of Kevlar® 49 originating from two (2) different manufacturers were tested. The manufacturers are listed below in Table 2.

Table 2: Kevlar® 49 Manufacturer Information

Material	Manufacturer	Date Received
Kevlar® 49 (1)	Lincoln Fabrics	April 2004
Kevlar® 49 (2)	JPS Composites	July 2009

Samples from Kevlar® 49 (1) were tested in conjunction with the fabric aging study.

Previous tension tests were conducted at ASU on the following dates: Sept 2004 (aging study and new fabric tests, warp only), Feb 2005 (new fabric tests, fill only), Feb 2008 (aging study only), Sept 2009 (new fabric tests).

2.1.2 Test Setup and Procedure

2.1.2.1 Apparatus

Tension testing was conducted per American Society for Testing Materials (ASTM) procedure, Tensile Testing of Polymer Matrix Composites – ASTM D 3039 “Standard Test Method for Tensile Properties of Fiber-Resin Composites.” under open loop conditions with a rate of actuator displacement (stroke) of 0.1”/min. Digital data acquisition was used to collect data at every 0.5 second. The test was continued until complete failure of the specimen was achieved (complete failure considered reaching a post peak load of approximately 15 lb, see Figure 2 below).

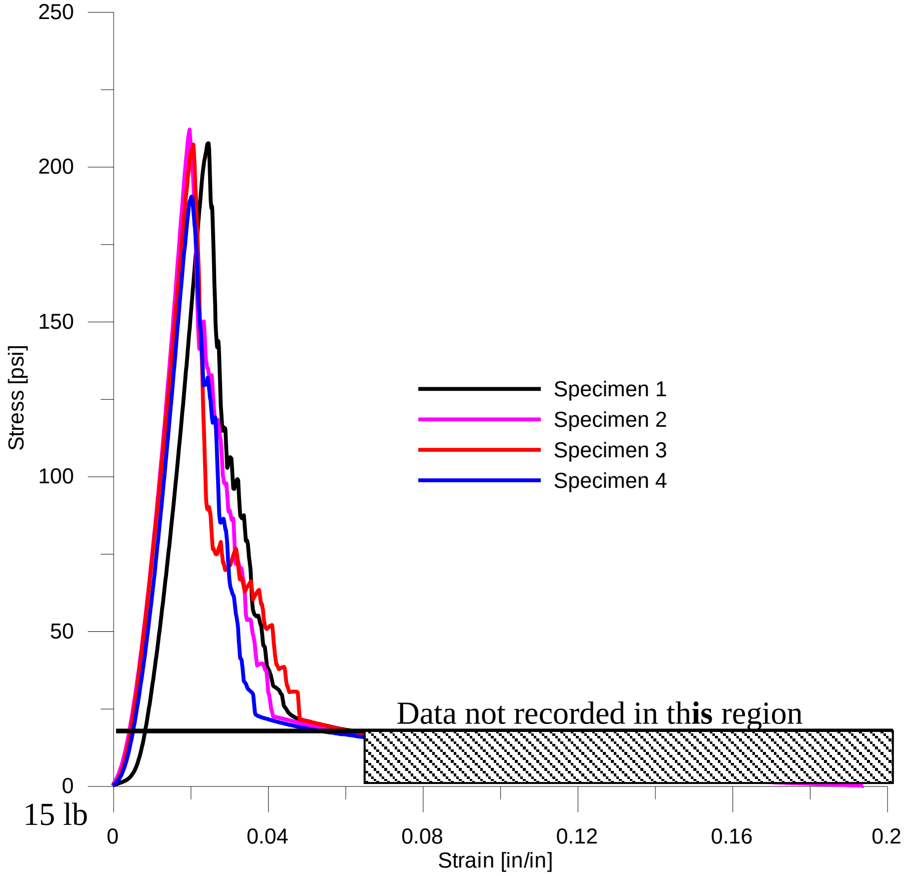

Figure 2. Static tension test failure definition

The load-deformation results were used to calculate the stress-strain response of the material. The overall deformation of the specimen was measured by the stroke movement of the actuator. Figure 3 below depicts a fabric specimen in the typical test setup.

Figure 3. Typical static tension test setup

2.1.2.2 Grips

In order to ensure that slipping of the specimens (from the grips) did not influence the deflection values, the gripping fixture developed during Phase I of the research was used (see Figure 4 below). Flat steel plates 2.5” wide, 2” long, 0.25” thick are used to grip the specimen at both ends. At each end, one of the two pieces has a curved groove at the center of the plate throughout its width, which is half the thickness of the plate. The other plate has a V-notch cut in the same position about half the thickness of the plate. A round aluminum rod is cut along the length to the shape of the groove to match the existing grooves in the steel plate. The fabric was held between the V-notch and the aluminum piece so that the notch pinches against the fabric and prevents from slipping with respect to the end plates. The two plates were pressed with hydraulic grips thereby ensuring uniform pressure application to minimize, if not prevent, any fabric slipping. Figure 4 shows the specimen gripping system utilized during testing.

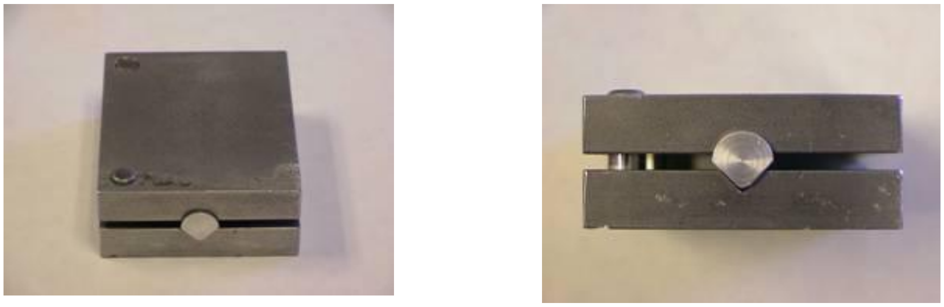

(a) End Plates for Gripping

(b) Side View

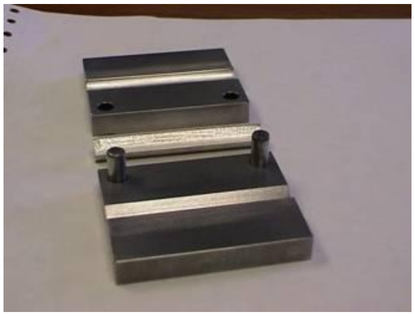

(c) Inner View

Figure 4: Specimen Gripping System

2.1.3 Test Results

2.1.3.1 Kevlar® 49 (1) (For Aging Study, E_{11} Only)

The results from testing of Kevlar® 49 (1) samples are presented below. Note the naming convention used to identify the samples; Kevlar® 49 (1)_Date of Manufacture_Test Date. For example, Kevlar® 49 (1)_April 2004_ May 2010 indicates a sample of Kevlar® 49 manufactured in April of 2004 and tested in May of 2010. Results from testing performed in May 2010 as well as previous test results are presented below. Note that units of stress for the aging study are presented in ksi to remain consistent with results from previous testing.

2.1.3.2 Kevlar® 49 (1)_April 2004_Sept 2004

Table 3: Tension Test Results Data Kevlar® 49 (1)_April 2004_Sept 2004

Specimen	Max Stress (ksi)	Max Ult. Strain (in/in)	Stiffness (ksi)
1	241.99	0.0274	13608
2	223.93	0.0287	13187
3	235.96	0.0295	13525
4	244.32	0.0365	13154
5	227.41	0.0319	13380
Average	234.72	0.0308	13371

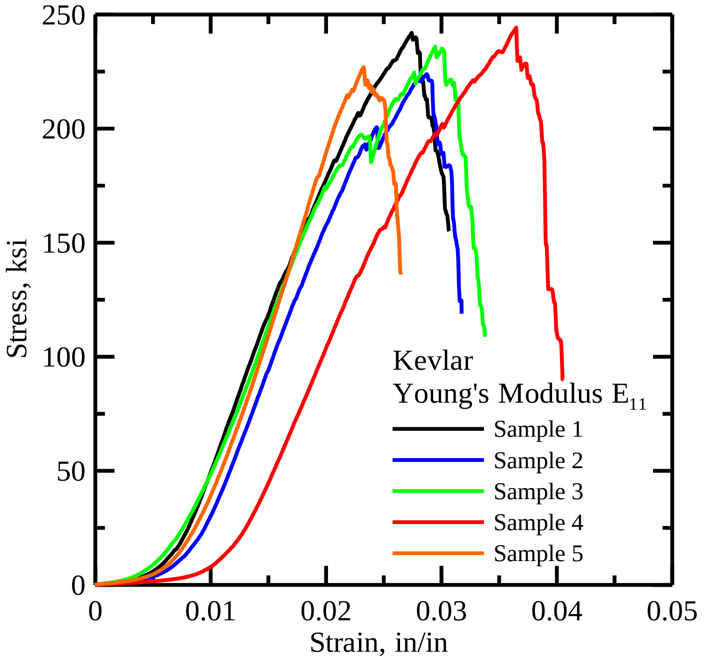

Figure 5: Stress/Strain Curves for Kevlar® 49 (1)_April 2004_Sept 2004

2.1.3.3 Kevlar® 49 (1)_April 2004_Feb 2008

Table 4: Tension Test Results Data Kevlar® 49 (1)_April 2004_Feb 2008

Specimen	Max Stress (ksi)	Max Ult. Strain (in/in)	Stiffness (ksi)
1	241.14	0.02345	14075
2	232.17	0.01891	15786
3	236.17	0.02423	14258
4	236.70	0.02487	13022
Average	236.55	0.02286	14285

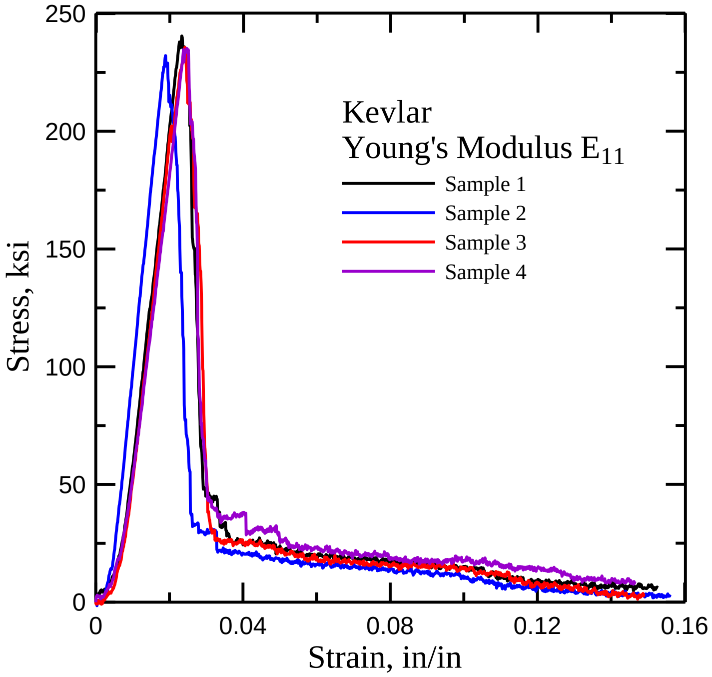

Figure 6: Stress/Strain Curves for Kevlar® 49 (1)_April 2004_Feb 2008

2.1.3.4 Kevlar® 49 (1)_April 2004_May 2010

Table 5: Kevlar® 49 (1) _ April 2004 _ May 2010 Tension Test Results

Specimen	Maximum Stress (ksi)	Max. Ult. Strain (in/in)	Stiffness (ksi)
1	207.43	0.0248	13630
2	211.86	0.0199	12269
3	207.04	0.0208	13349
4	190.22	0.0204	12806
Average	204.13	0.0215	13013

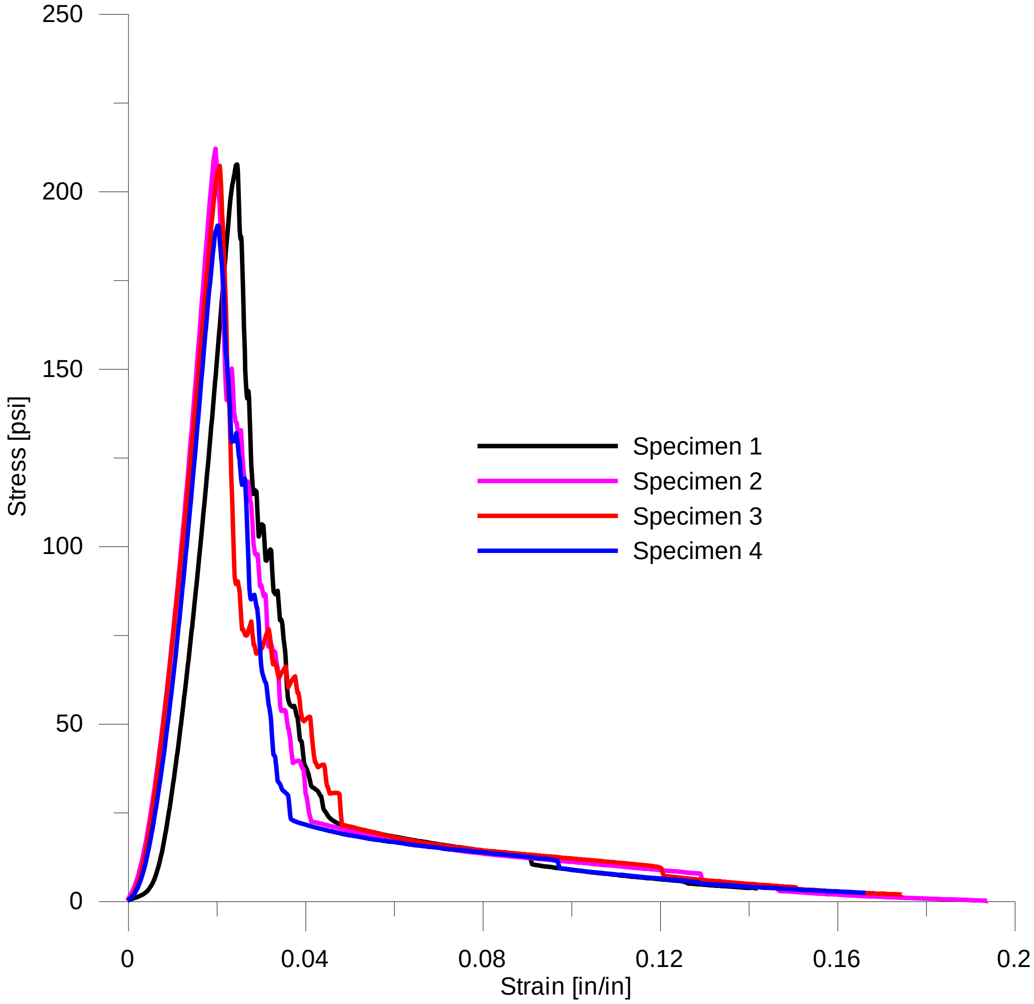

Figure 7: Stress/Strain Curves for Kevlar® 49 (1)_April 2004_May 2010 E_{11}

2.1.4 Results Comparison

Results obtained associated with the fabric aging study are presented below in Table 6.

Table 6: Kevlar® 49 (1) Results Comparison

Date Tested	Max Stress (ksi)	Max Ult. Strain (in/in)	Stiffness (ksi)
Sept 2004	234.72	0.03	13371
Feb 2008	236.55	0.0229	14285
May 2010	204.14	0.0215	13014

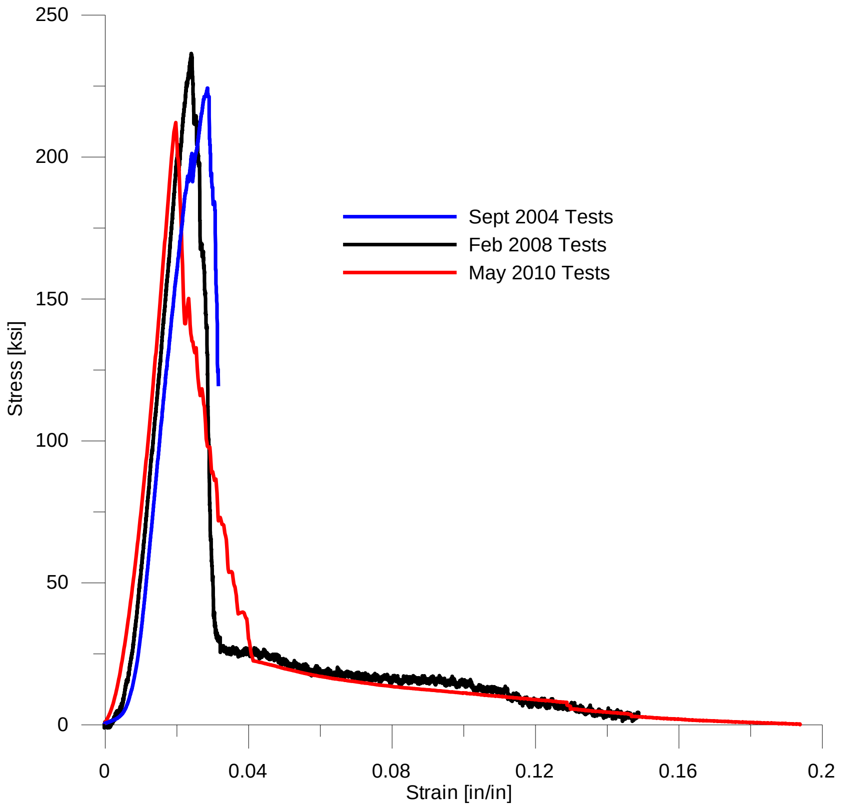

Figure 8: Comparison of Stress/Strain Response for Kevlar® 49 Fabric

The following observations can be made based on the test results obtained: aging of Kevlar® 49 fabric has little effect on the attainable peak stress, there is no degrading effect on the stiffness due to aging of the fabric, and the strain realized at peak stress decreases with age.

2.1.4.1 Kevlar® 49 (2)

The results from testing of Kevlar® 49 (2) samples are presented below.

2.1.4.1.1 Fill Direction (E_{22})

Table 7: Kevlar® 49 (2) Tension Test Results, Fill Direction

Specimen #	Max Load (lb)	Modulus (psi)	Toughness (psi)	Max Stress (psi)	Strain at Max Stress (in/in)
1	1269	14440361	5130	209685	0.0254
2	1452	14285561	4731	239842	0.0285
3	1635	15191795	4655	270105	0.0294
4	1525	13731977	4417	251924	0.0275
5	1599	15946139	4681	264166	0.0297
Average Values	1496	14719166	4723	247144	0.0281

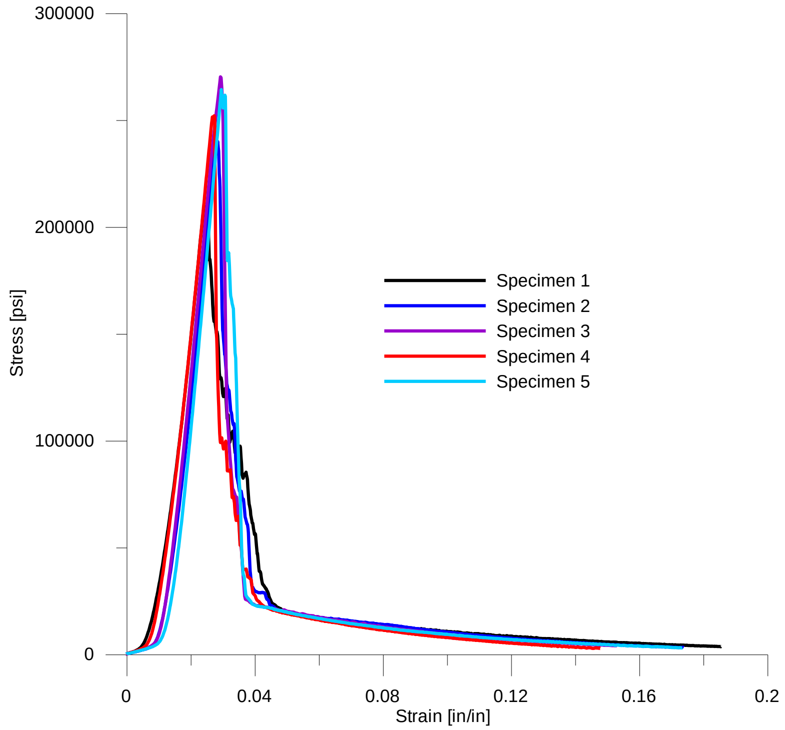

Figure 9: Stress/Strain Curves for Kevlar® 49 (2) E_{22}

2.1.4.1.2 Warp Direction (E_{11})

Table 8: Kevlar® 49 (2) Tension Test Results, Warp Direction

Specimen #	Max Load (lb)	Modulus (psi)	Toughness (psi)	Max Stress (psi)	Strain at Max Stress (in/in)
1	1586	15717959	4382	261996	0.0192
2	1489	15145317	4737	245977	0.0208
3	1592	16517904	4869	263005	0.0191
4	1446	14476876	4915	238944	0.0222
5	1558	15673663	5179	257497	0.0223
Average Values	1534	15506344	4817	253484	0.0207

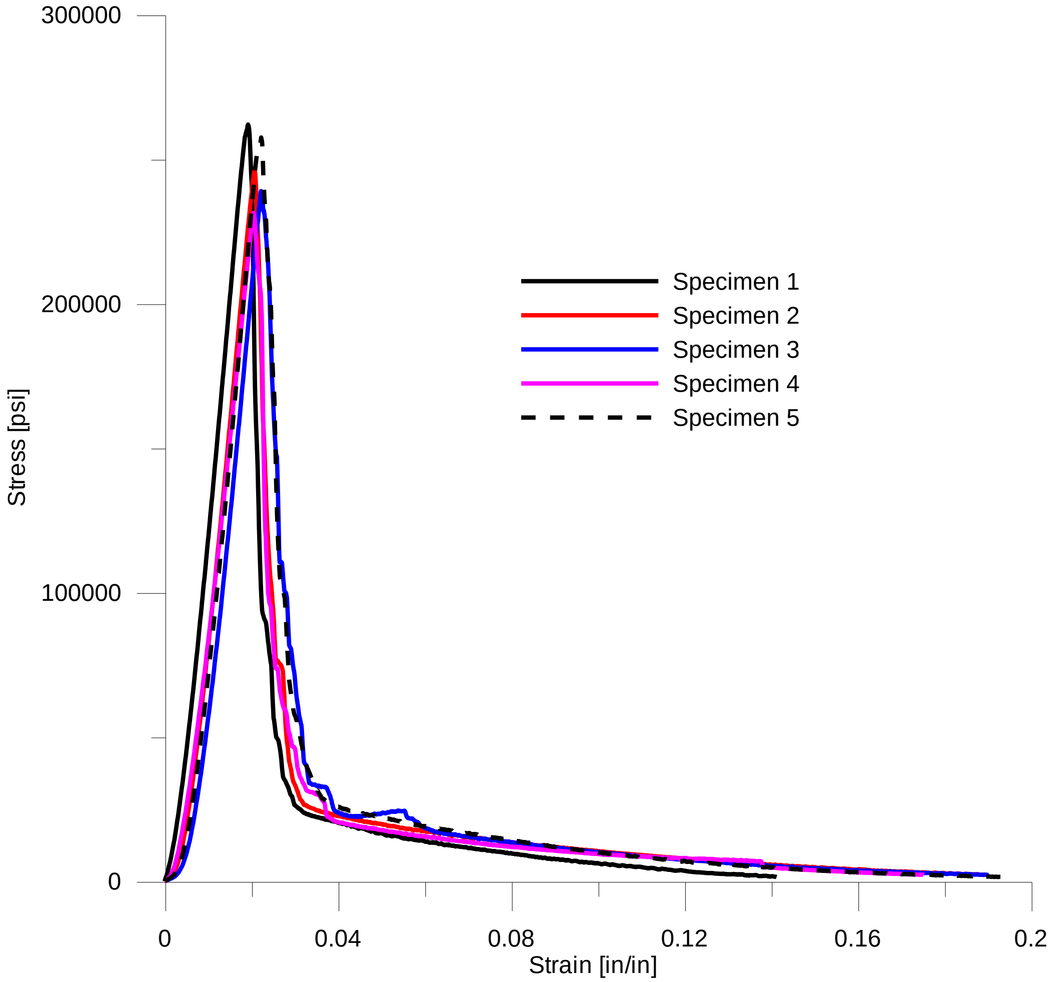

Figure 10: Stress/Strain Curves for Kevlar® 49 (2) E_{11}

2.1.4.1.3 Comparison with Previous Results

Comparisons of results from tension testing of Kevlar® 49 fabric obtained in May 2010 with results from previous testing in both the warp and fill directions are shown below in Figure 11 and Figure 12. Data sets included in the following comparison are representative of the average results obtained for each set of tests.

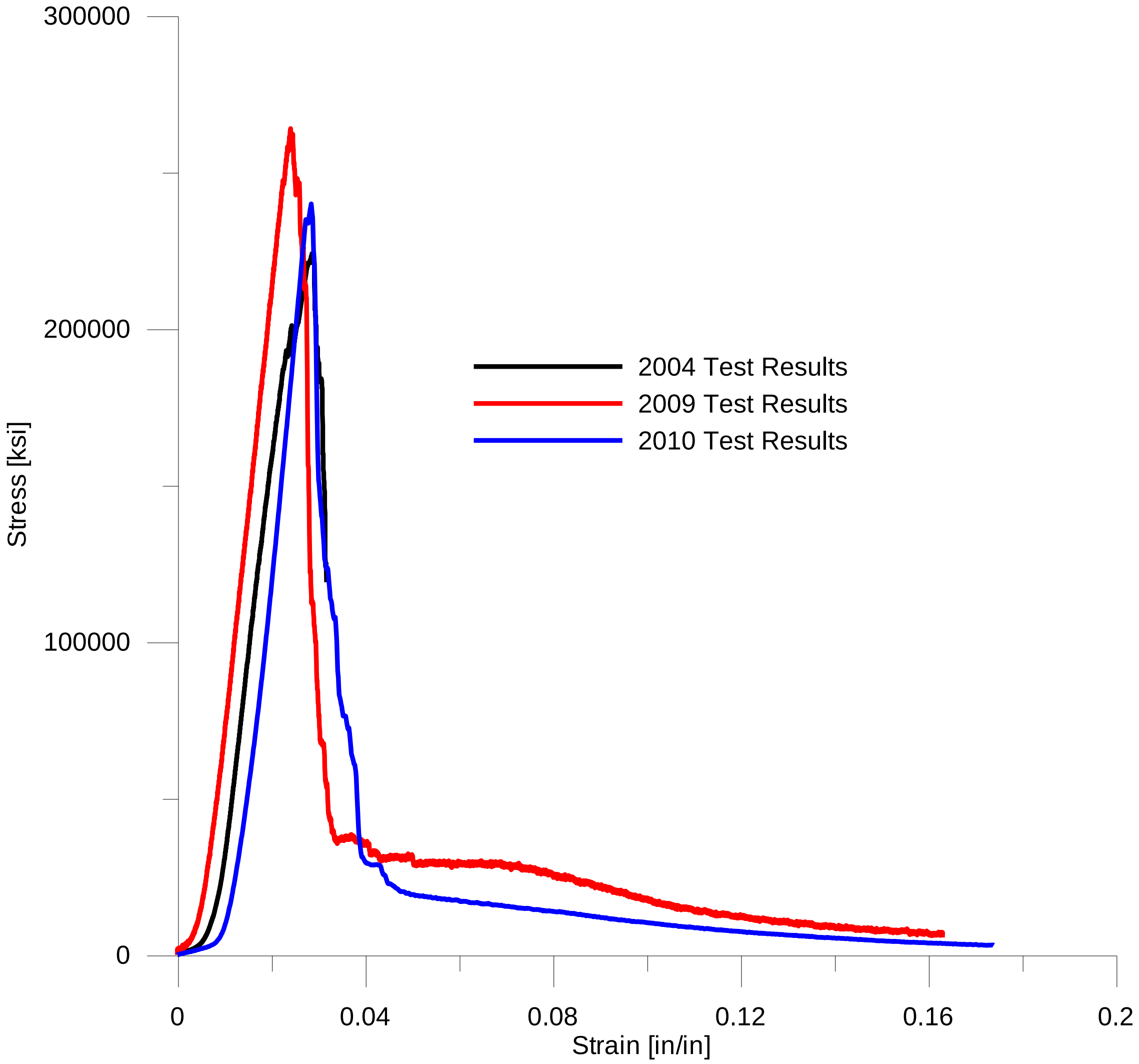

Figure 11: Comparison of Tension Test Results of Kevlar® 49 Fabric E_{11} (Warp)

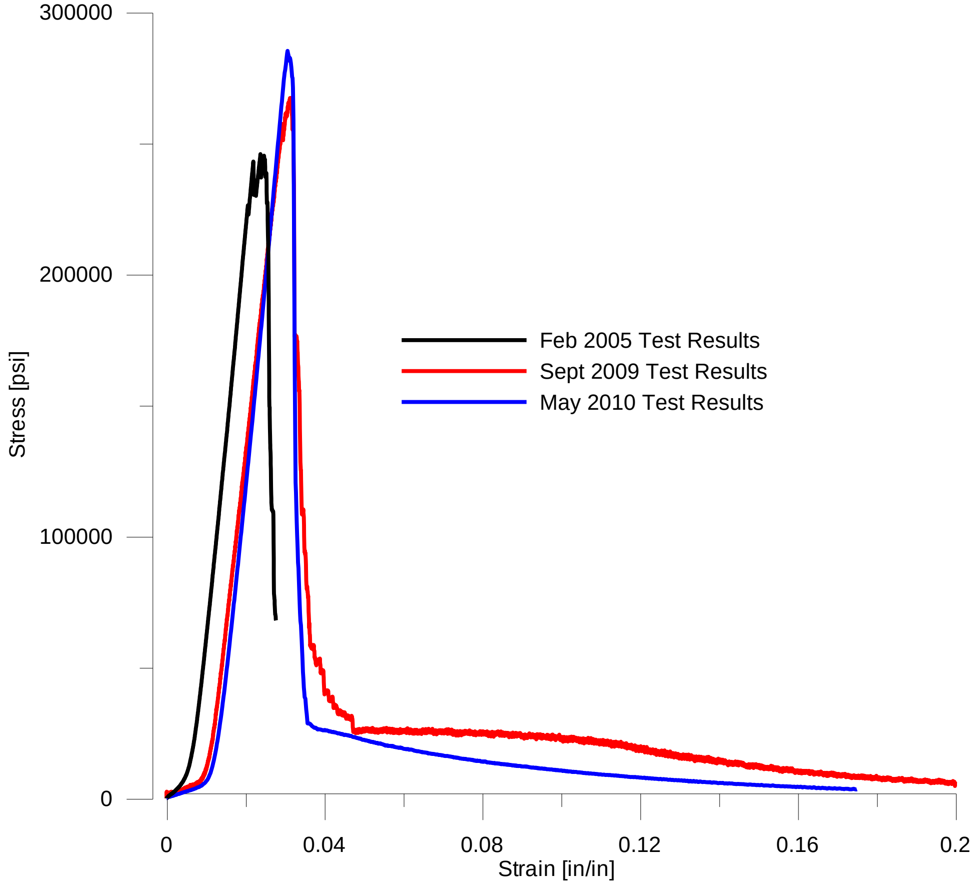

Figure 12: Comparison of Tension Test Results of Kevlar® 49 Fabric E_{22} (Fill)

As previously noted, fabrics tested in February 2005 originated from a different manufacturer than those tested in September 2009 and May 2010. This may account for some differences found in test results.

2.1.4.2 Kevlar® 149

The results from testing of Kevlar® 149 samples are presented below.

2.1.4.2.1 Fill Direction (E_{22})

Table 9: Kevlar® 149 Tension Test Results, Fill Direction

Specimen #	Max Load (lb)	Modulus (psi)	Toughness (psi)	Max Stress (psi)	Strain at Max Stress (in/in)
1	1693	1123964	478	24468	0.0285
2	1839	1146544	540	26580	0.0300
3	1749	1091860	460	25268	0.0360
4	1615	1016108	480	23336	0.0370
5	1722	1071119	486	24888	0.0377
Average Values	1724	1089919	489	24908	0.0338

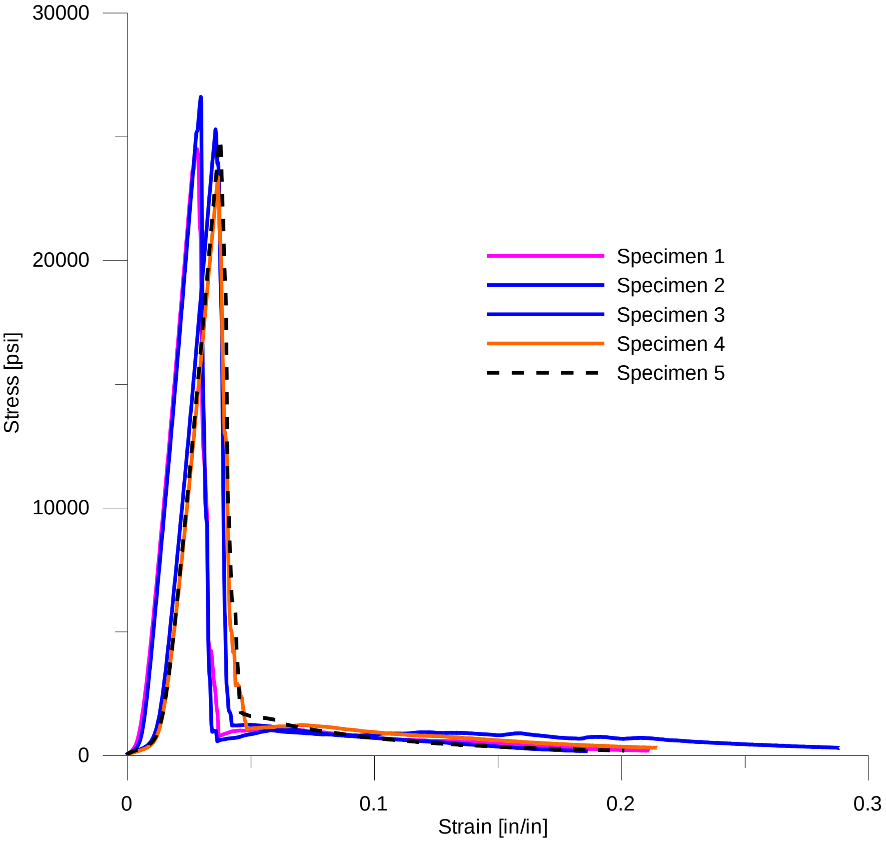

Figure 13: Stress/Strain Curves for Kevlar® 149 E_{22}

2.1.4.2.2 Warp Direction (E_{11})

Table 10: Kevlar® 149 Tension Test Results, Warp Direction

Specimen #	Max Load (lb)	Modulus (psi)	Toughness (psi)	Max Stress (psi)	Strain at Max Stress (in/in)
1	1675	1107494	504	24210	0.0406
2	1671	1100742	468	24145	0.0388
3	1577	966366	453	22788	0.0450
4	1697	1056392	471	24525	0.0430
5	1633	1039351	468	23601	0.0400
Average Values	1651	1054069	473	23854	0.0415

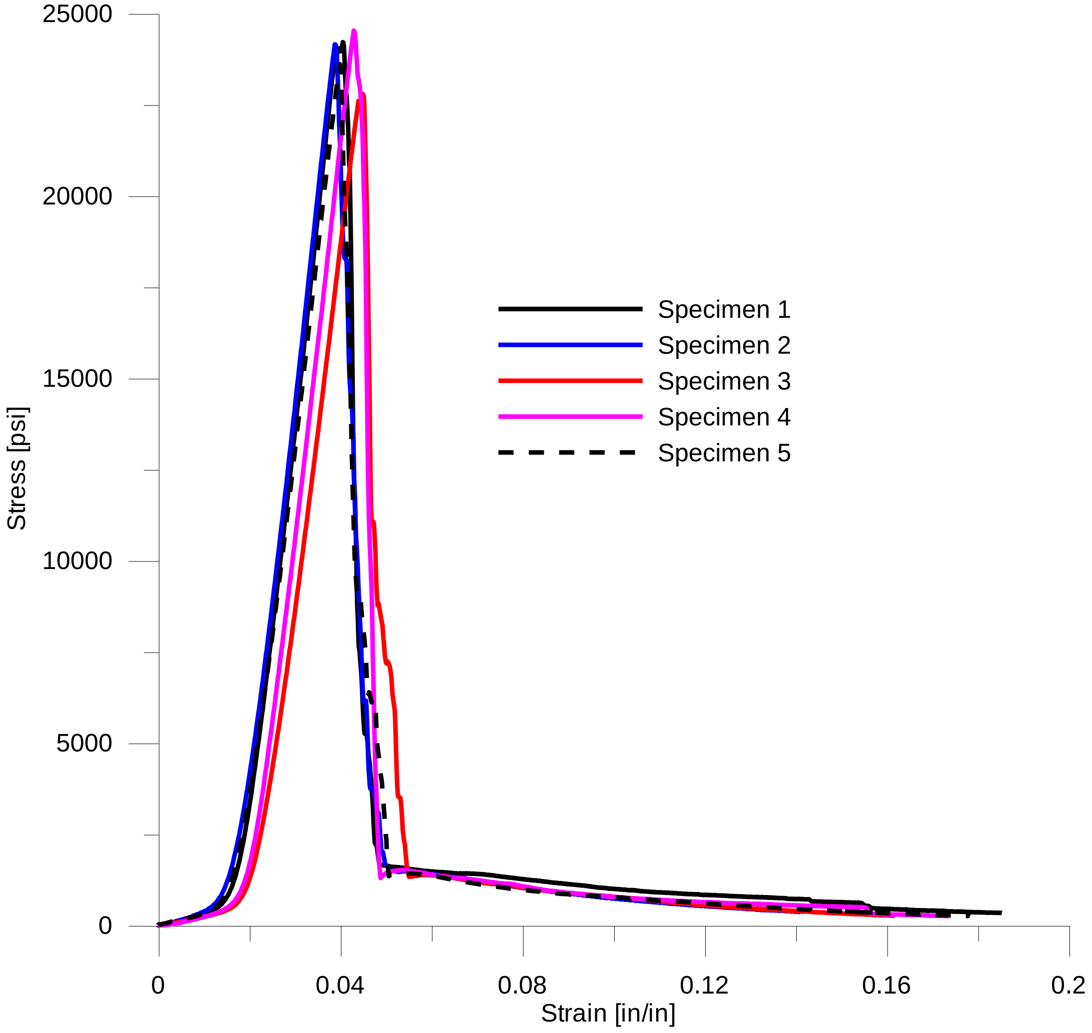

Figure 14: Stress/Strain Curves for Kevlar® 149 E_{11}

3 STATIC PENETRATOR TESTING

3.1 Overview

Quasi-static penetrator testing of Kevlar® 49 fabric was performed at ASU in an attempt to capture the stress strain response of the material under similar loading conditions to those experienced during ballistic testing. The experiments were performed on an Instron 55 Kip servo-hydraulic test frame under open-loop displacement controlled conditions. Strains experienced by the fabric during testing were measured using an optical non-contact measurement system (ARAMIS).

3.2 Experimental Setup

The static penetrator test consisted of the following equipment:

- (1) 1” thick x 40” dia. Steel Ring with Support Frame
- (1) 2” x 2” x 8” Steel Penetrator
- (1) Steel Penetrator Housing Box
- 7”x9” First Surface Mirror
- Mirror Support Frame
- Threaded Mounting Rods/Collars
- (1) 50 Kip Instron Servo-hydraulic Load Frame
- 4” Wide Kevlar® 49 Fabric
- 5 Minute Epoxy
- Electric Fabric Shears
- ARAMIS Computer Software Station
- ARAMIS Camera System

The steel ring and support frame were installed on the lower actuator of the load frame. After the ring was in place, the penetrator housing box (PHB) was constructed around the upper portion of the ring and installed into the upper crosshead of the load frame. A small metal support frame was developed to hold the mirror in place inside of the PHB. The support frame was designed to keep the mirror at a 45 degree angle from the horizontal to ensure that the images captured by the ARAMIS system were normal to the surface of the Kevlar® fabric.   A diagram depicting the mirror setup configuration is shown in Figure 15.

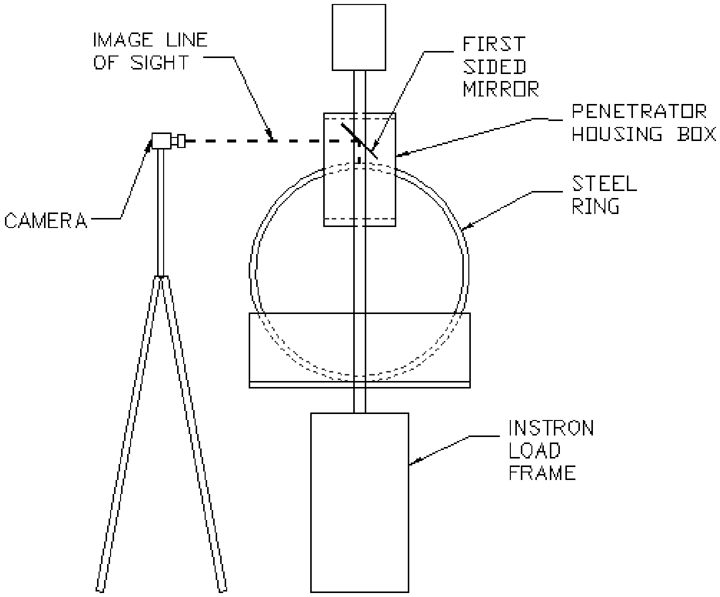

Figure 15. Schematic of Static Penetrator Testing Setup

A painted pattern was applied to the full width of approximately 12 inches of all fabric test specimen prior to installation. The pattern was created by first applying white primer to the fabric. Once the white coat was dry, black paint was applied using either an aerosol spray can or an airbrush system. This paint pattern is utilized by the ARAMIS optical measurement system to determine the displacements/strains throughout the sample during testing. An example of the paint pattern applied to the fabric is shown below in Figure 16.

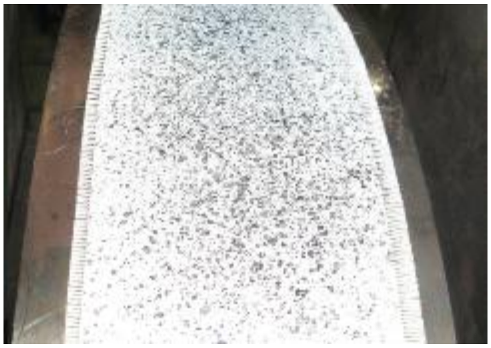

Figure 16. Paint Pattern Applied to Fabric Surface

The process and theory behind the ARAMIS measurement system is discussed in greater detail in the ARAMIS Software Manual (GOM, 2007) and Hardware Manual (GOM, 2007). Once the steel ring, PHB and mirror apparatus were in place, a Kevlar® test specimen was wrapped around the ring and secured using five minute quick set epoxy. The first edge of the Kevlar® fabric was taped to the steel ring. The fabric was then wrapped around the ring and pulled taut using a wooden block to remove any slack that may be present in the fabric. The second end of the fabric was then secured to the ring using a C-clamp. Six (6) inches of overlap between the ends of the fabric specimen was provided to ensure adequate bonding between the fabric layers to prevent potential slippage. Five minute epoxy was applied to the bottom layer of fabric until the material appeared saturated, then the outer layer of fabric was placed on top and itself saturated with epoxy. A straight screed bar was used to press the outer layer onto the inner layer to ensure uniform adhesion throughout the bond region. The epoxy was left to cure in place for a minimum of two hours. Once the epoxy had set, the C-clamp was removed and the fabric was oriented on the ring so that the painted surface was at the top of the ring, bringing it within the field of view of the cameras. The fabric was then clamped in the lower half of the ring on either side as shown below in Figure 17.

Figure 17. Kevlar® Fabric Clamped to Steel Test Ring

With the fabric in place, the lower actuator/ring assembly was adjusted to the point when the surface of the fabric just touched the tip of the penetrator keeping the penetrator centered in the ring opening. The penetrator was oriented so that the long dimension of the tip was parallel to the transverse axis of the fabric as shown below in Figure 18.

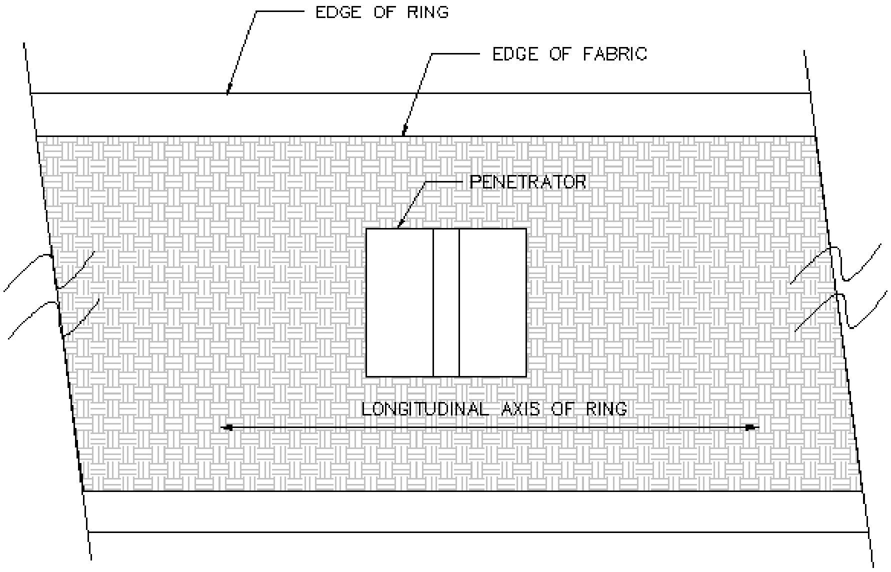

Figure 18. Penetrator Orientation During Testing

The PHB, ring apparatus and mirror support frame were then adjusted to ensure that each component was oriented correctly with respect to the measurement systems. First, the height of the mirror was set by placing a sheet of white paper on the surface of the mirror closest to the ARAMIS cameras. The paper had previously been cut to match the size of the mirror and the center of the mirror had been marked on the surface of the paper. The mirror was adjusted to align the laser with the center of the mirror.

The ARAMIS camera system was placed on a camera tripod support and secured. The tripod was then set on a support table to achieve the height necessary to capture images of the procedure. The tripod was centered on the test ring at a distance sufficient enough to obtain the measurement parameters required by the ARAMIS system for a particular measurement volume. Care was taken to ensure that the camera support bar was level and square to the PHB.

Using the laser indicator on the ARAMIS support bar, the orientation of the camera support bar was verified to ensure that the camera system was aligned with the center of the mirror. The mirror system was then removed from the load frame and the ARAMIS system was calibrated. The calibration procedure was followed without the use of the mirror for simplicity (refer to the ARAMIS Software Manual for a detailed description of the calibration procedure. Once the system was calibrated, the mirror was set in place back on the load frame and the measurement system was checked for accuracy by running a simple rigid body displacement test. The penetrator was removed from the PHB and the ring apparatus was moved down at a constant rate while capturing images with the ARAMIS system. After processing the images, the displacement of the system was verified and the ring apparatus was returned to its initial position and the penetrator was replaced back into the PHB. The test procedure was then run while recording images taken by the ARAMIS system.

3.2.1 Test Procedure

All testing was performed under open-loop, displacement controlled conditions at a stroke rate of 0.4 in/min. Due to limitations of the load frame and the large size of the ring apparatus, all tests were performed through a total stroke of 1.75 in, which was determined to be ample distance to develop sizeable strains in the fabric specimen. Images were taken by the ARAMIS system at a rate of 12 images per minute or 1 image every 5 seconds. This frequency proved to be sufficient to capture the displacements of the fabric and subsequently calculate the strains.

The test procedure and the image collection were started simultaneously. The force measured by the load cell of the test frame and the stroke of the actuator were recorded by the load frame control computer Once the predetermined maximum stroke value was reached, the test procedure was stopped and the lower actuator was returned to the starting position. The clamps were then removed, the fabric specimen was taken off of the ring apparatus and the next specimen was installed.

Testing was performed on ten (10) fabric specimen; five (5) consisting of a single wrap of fabric and five (5) consisting of a double wrap of fabric.

3.3 ARAMIS Overview

The ARAMIS system by GOM Optical Measuring Techniques is a non-contact, 3-dimensional strain measurement system. The system utilizes an image correlation algorithm to measure the displacements experienced by a material under load. Images (stages) of experimental tests are taken at a specified frequency for a set time duration. The ARAMIS software identifies groups of pixels of a specified dimension in the initial stage (undeformed state) called “facets”. These facets must be identifiable from both cameras to formulate the 3-D image correlation necessary.

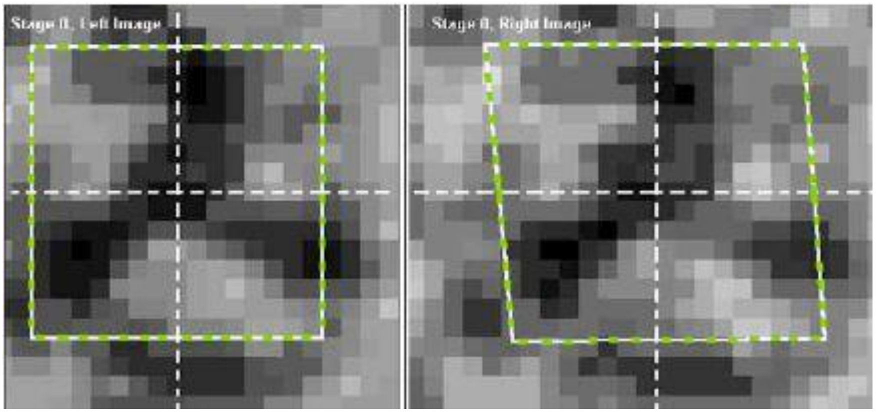

Figure 19. Example of Image Facet Utilized by ARAMIS Software

These facets are tracked from stage to stage and the measured distances between the centers of the facets in the three principal directions are recorded. Using these measured distances, the system software is able to calculate the three dimensional strain field of the sample, providing the user with a great deal of information regarding the materials load response characteristics.

3.3.1 ARAMIS Setup

To use the ARAMIS system for testing, the measurement volume of the specific test to be performed must be determined. The measurement volume represents the three-dimensional space in which the testing will be located. Figure 20 below shows a graphical depiction of the measurement volume and the associated parameters required for the setup and calibration of the ARAMIS camera system.

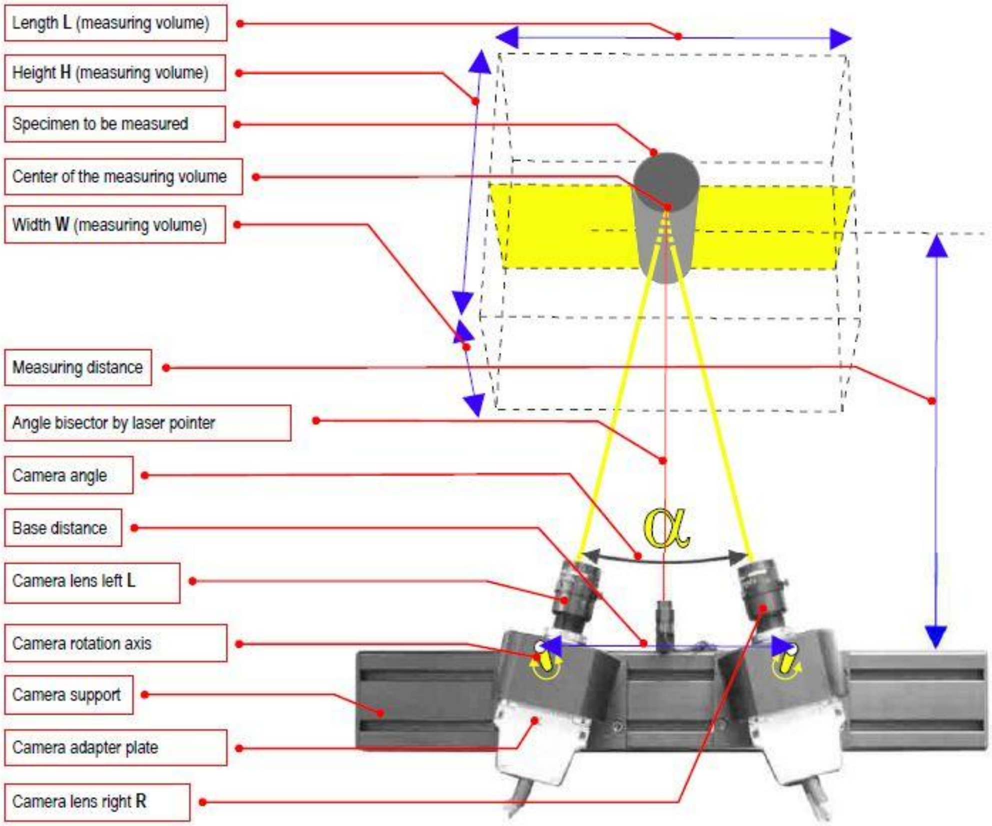

Figure 20. ARAMIS Measurement Volume

The parameters associated with the setup of the camera system are dependent on the measurement volume desired, which in turn is a function of the lens type used in analysis. For this analysis, a 50 mm lens was used. The system recognizes two (2) different classifications of 50 mm lenses, Lens Family B and Lens Family C. These classifications are shown below in Figure 21.

Aperture setting ring with manual locking screw. Note: In the example shown, aperture value 11 means aperture closed and aperture value 1.4 means aperture open.

Screw thread; tighten carefully by hand in the housing!
While doing so, lock focus locking ring!

Focus locking ring with hex socket head locking screw

Focal length.
In this example 17 mm.

(a) Lens Family B


Screw thread; tighten carefully by hand in the housing!
While doing so, lock focus locking ring!

Focus setting ring with locking screw

Aperture setting ring. Note: The lowest possible aperture value (e.g. 2.8) means the aperture is max. opened and the highest value indicates that the aperture is max. closed.

(b) Lens Family C

Figure 21. ARAMIS Lens Family Classifications

The attainable measurement volume is also dependent on the size of the calibration object available. Based on the large scale of the testing to be performed, the largest calibration object available was the coded object C120x96. Based on this calibration object, the following dimensional properties provided in Table 11 were required to obtain the necessary measurement volume for this procedure.

Table 11. ARAMIS Configuration Dimensional Properties

M.V. (mm^3)	Base Dist. (mm)	Meas. Dist. (mm)	Camera Angle (°)	Field Depth (mm)
120 x 96	400	900	25	40

As the test configuration used mirrors to take measurements normal to the surface of the fabric, care was taken to ensure that the total distance from the camera housing to the surface of the fabric corresponded to the measurement distance required by the ARAMIS system. The distance from the camera housing to the center of the mirror was added to the distance from the center of the mirror to the surface of the fabric with the ring/fabric system in the initial position. To obtain the required measurement distance, the initial position of the ring/fabric was adjusted as needed. The test setup was verified by performing a rigid body displacement test where a series of stages were recorded while moving the ring/fabric through the measurement volume at a known rate of displacement. The displacements measured were compared against the stroke of the actuator and were found to be in good agreement.

A first surface mirror was utilized to reflect the images to and from the ARAMIS camera system. Second-surface mirrors will introduce additional optical refraction as the image passes through the first surface of the mirror to the reflective backing and then again as the image passes through the first surface on its way back to the camera lens. These refractions will lead to erroneous measurement results. The additional refractions are illustrated below in Figure 22.

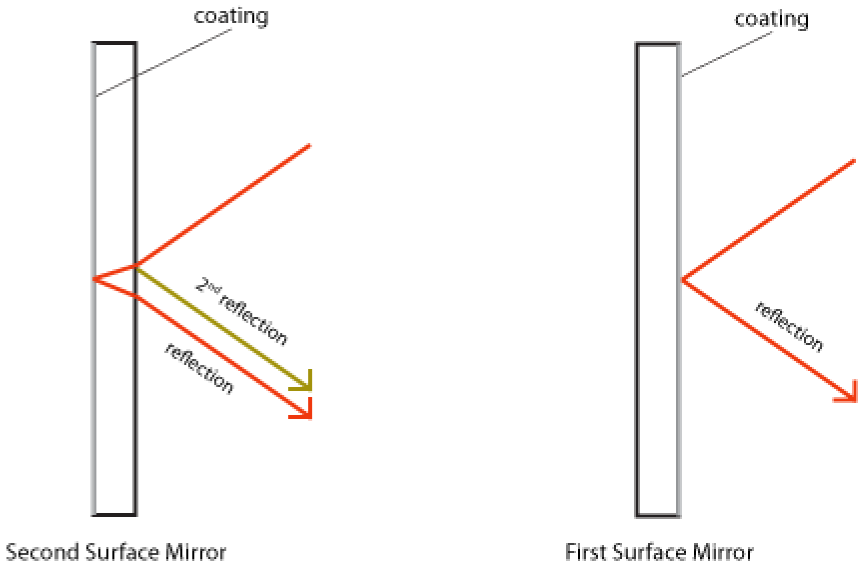

Figure 22. Image Reflection: First vs. Second Surface Mirrors (Image Courtesy of www.FirstSurfaceMirrors.com)

Figure 23 below shows the ARAMIS cameras installed on the support bar. Lighting during testing was provided by halogen flood lights placed directly behind and above the camera housings. Due to the high heat released by the flood lights, it was necessary to place the lighting above the camera housings to prevent excessive heating of the camera bodies.

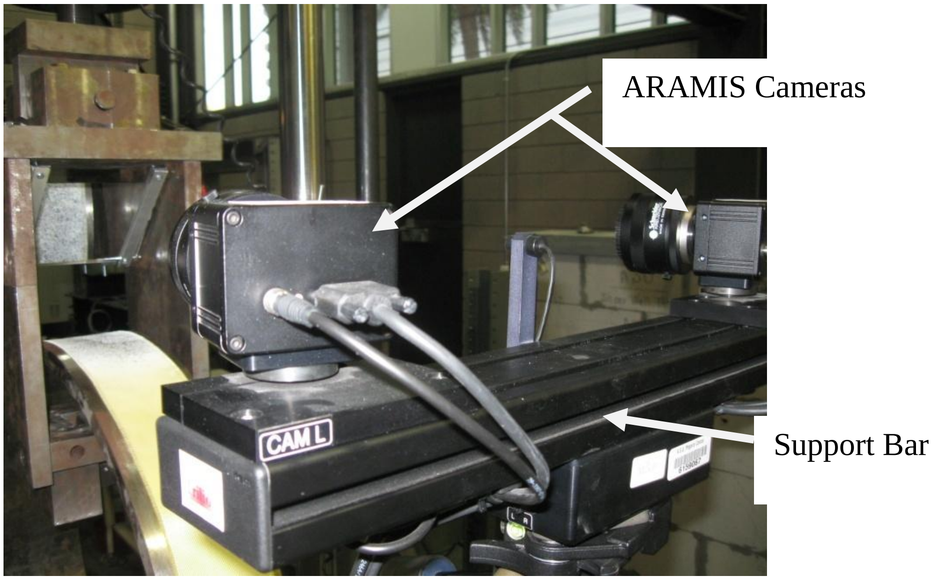

Figure 23. ARAMIS Cameras Mounted on Support Bar

Once the camera system was in place and the mirror support frame removed, the ARAMIS system was calibrated. The calibration procedure involved taking a series of images of the calibration object at a variety of orientations. By tracking the dots on the calibration object, the software is able to define the measurement volume space. With the calibration procedure completed, the mirror support frame was placed back onto the load frame, the ring apparatus was moved to its initial test position and the penetrator was placed back into the PHB.

3.4 Test Data Processing

Force and displacement data were collected from load frame’s load cell and LVDT at ½ second intervals during testing via the Labview software. This data was smoothed using a 5-point smoothing procedure in Matlab to mitigate the effect of any outlier data points. The MATLAB algorithm for the 5-point smoothing procedure is provided with this report in APPENDIX A.

3.5 Experimental Test Results

The results from five (5) single layer specimen and five (5) double layer specimen of Kevlar® 49 are presented here.

The load/displacement curves for the single layer specimen tests are provided below in Figure 24. Similarly the load/displacement curves for the double layer specimen tests are provided below in Figure 25. The load plots indicate the presence of an initial low modulus, uncrimping region (characteristic of woven fabric composite materials).

For both the double and single layer specimen, the fabric completes the uncrimping process at an actuator stroke of approximately 0.8 in and begins to take on more load during a region of relatively linear elastic loading. Due to the geometry of the experimental setup, namely the presence of the mirror required by the ARAMIS system and the limited depth of field available for strain measurement, the testing could not be run until failure of the fabric (found during previous testing to occur at stroke values greater than approximately 4”, (Bansal, 2007)), therefore the response curves only provide data up through the linear elastic loading region, up to an actuator stroke of 1.75”.

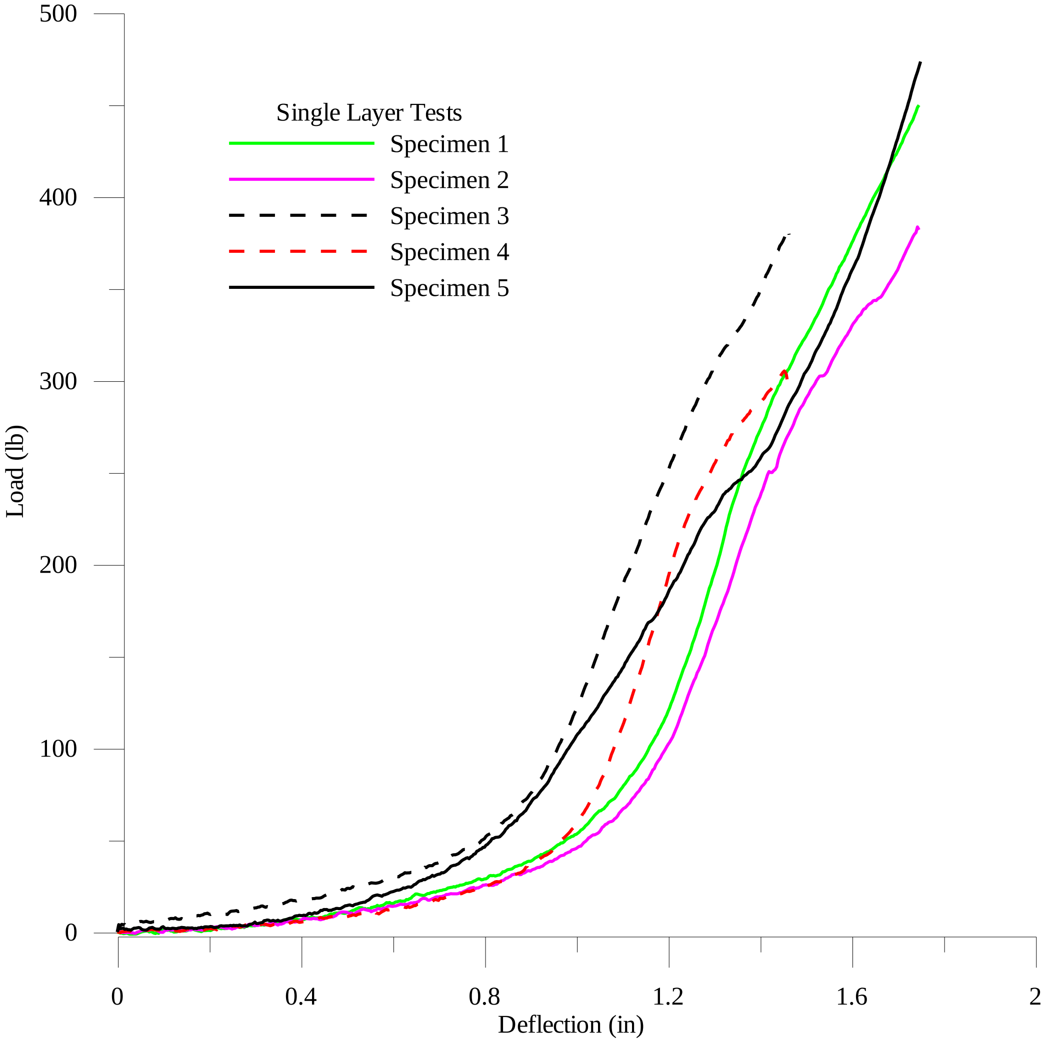

Figure 24. Load/stroke plots for single layer penetrator test specimen

Table 12. Load/Stroke Data: Single Layer Penetrator Test Specimen

Replicate	Max Stroke (in)	Max Load (lb)
1	1.75	449
2	1.75	383
3	1.46	383
4	1.45	305
5	1.75	473

Single layer specimens 3 and 4 experienced slippage of the penetrator at the fabric interface. These runs therefore were stopped short of the full 1.75” stroke specified for the test. Variation in the peak stresses attained by the single layer specimen were observed (mean peak stress = 435 lb, standard deviation = 46.6 lb). This variation was most likely due to inconsistent slack in the fabric at the beginning of the test. Other characteristics observed in the load/stroke response of the fabric agree with this explanation, such as the location of the "elbow" of the plot (the strain at which the fabric specimen begins to take substantial load, representing the end of the uncrimping region).

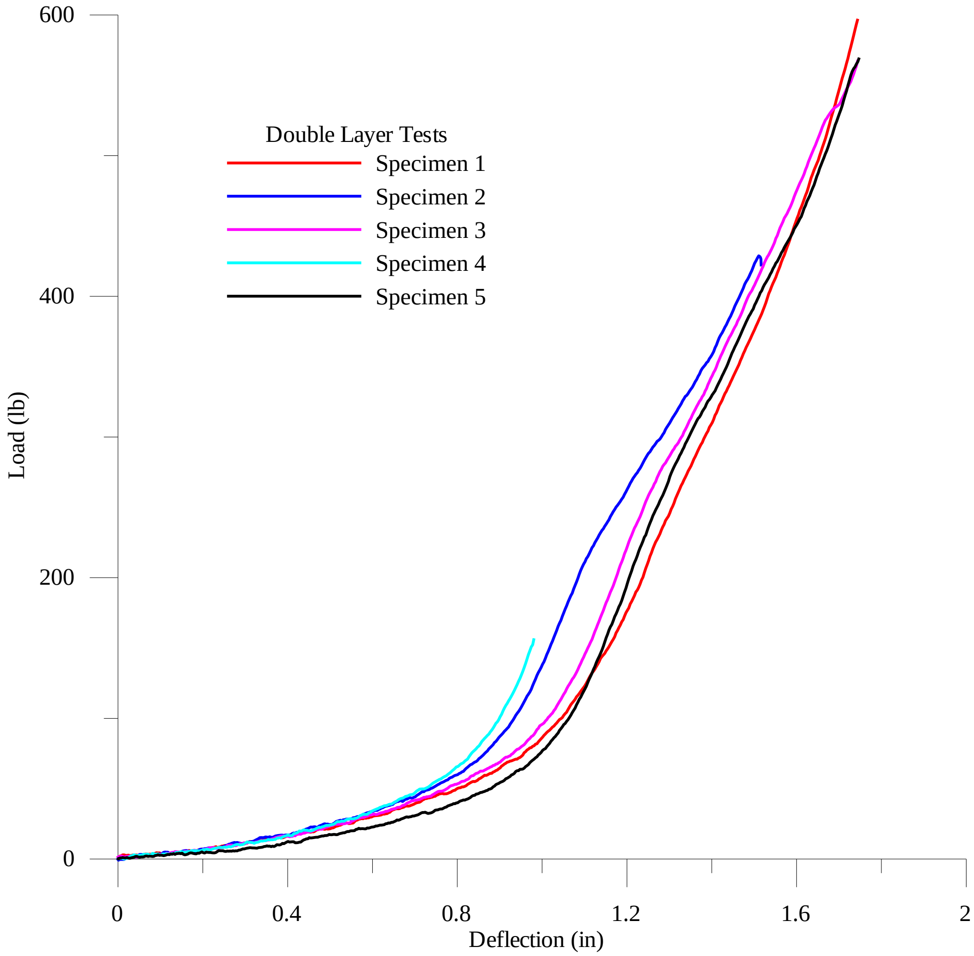

Figure 25. Load/Stroke Data: Double Layer Specimen

During the testing of Specimen 4, the penetrator slipped from its vertical position and the test procedure was stopped as can be seen in Figure 25. Slight variations in the load deflection response curves were observed in the double layer specimen results as in the single layer results. These are mainly due to variability in the fabric pretension applied to each sample.

3.5.1 ARAMIS Strain Measurements

3.5.1.1 Single Layer Specimen

ARAMIS strain measurements in the X (transverse) direction at 30 second intervals for a representative single layer specimen are provided below in Figures 26 thru 32

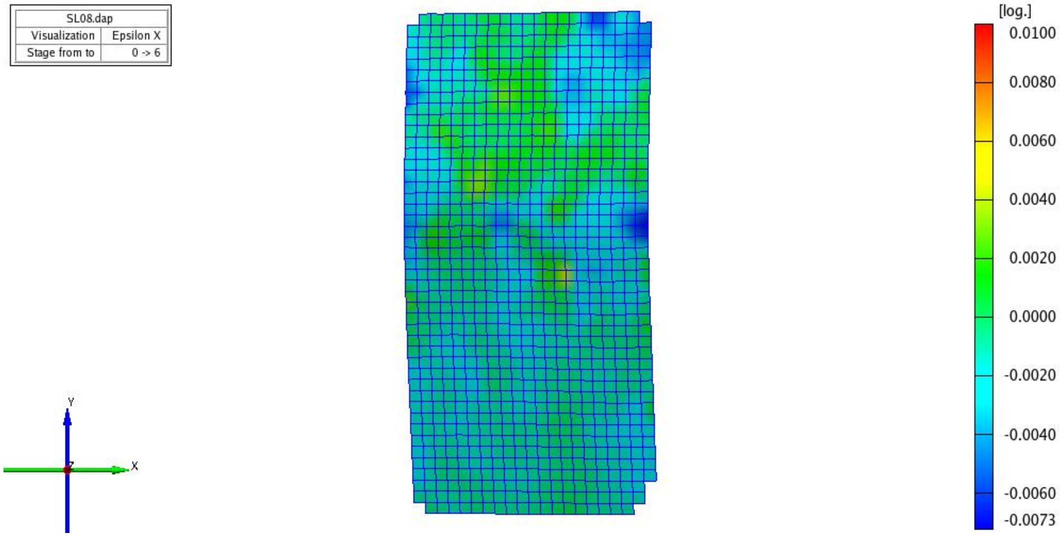

Figure 26. Single layer transverse strain (Time = 30 sec)

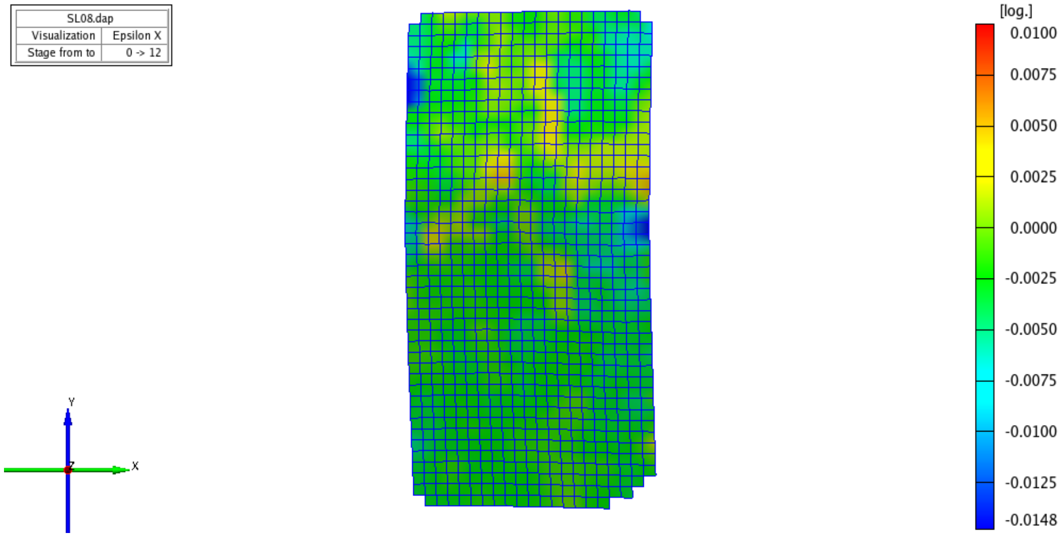

Figure 27. Single layer transverse strain (Time = 60 sec)

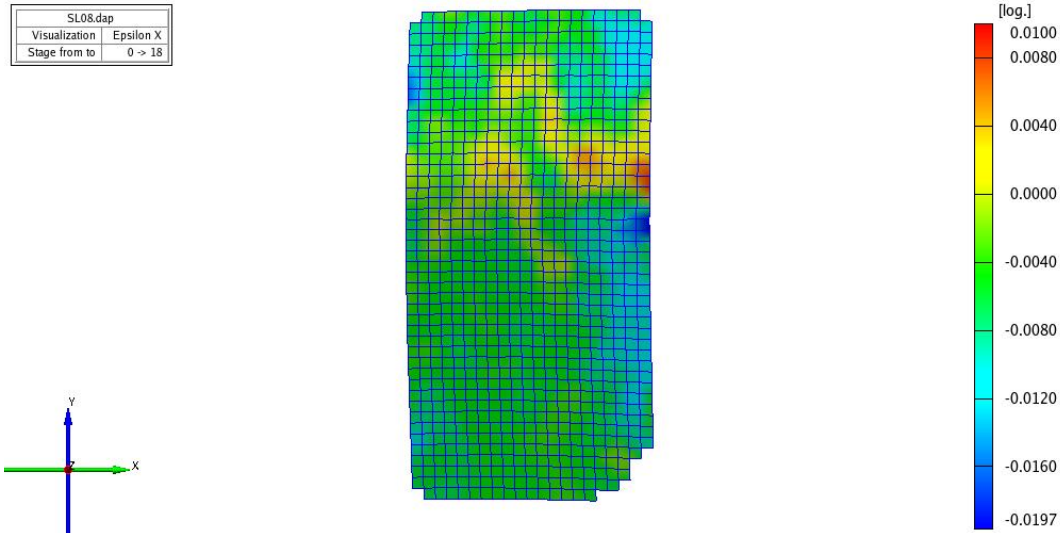

Figure 28. Single layer transverse strain (T = 90 sec)

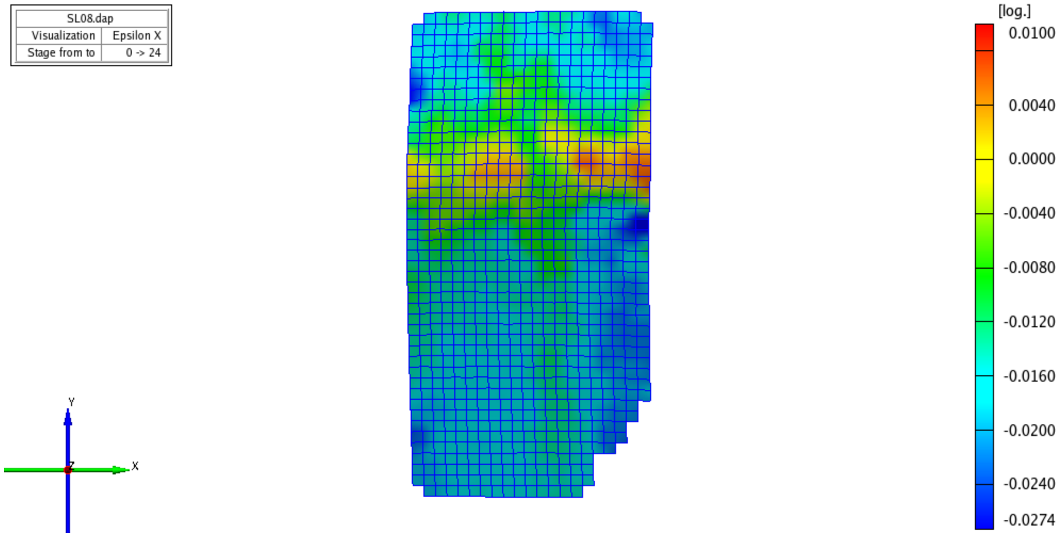

Figure 29. Single layer transverse strain (Time = 120 sec)

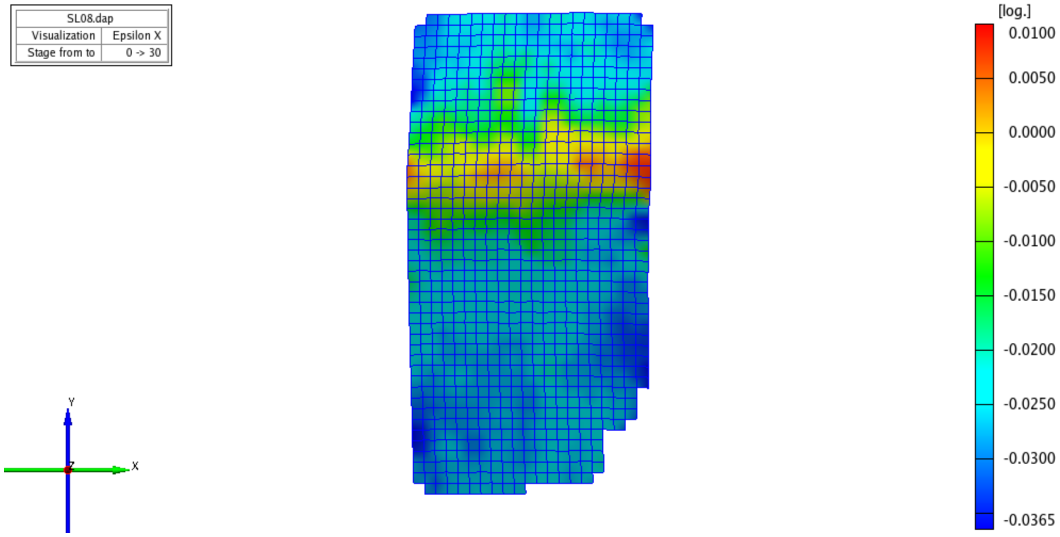

Figure 30. Single layer transverse strain (Time = 180 sec)

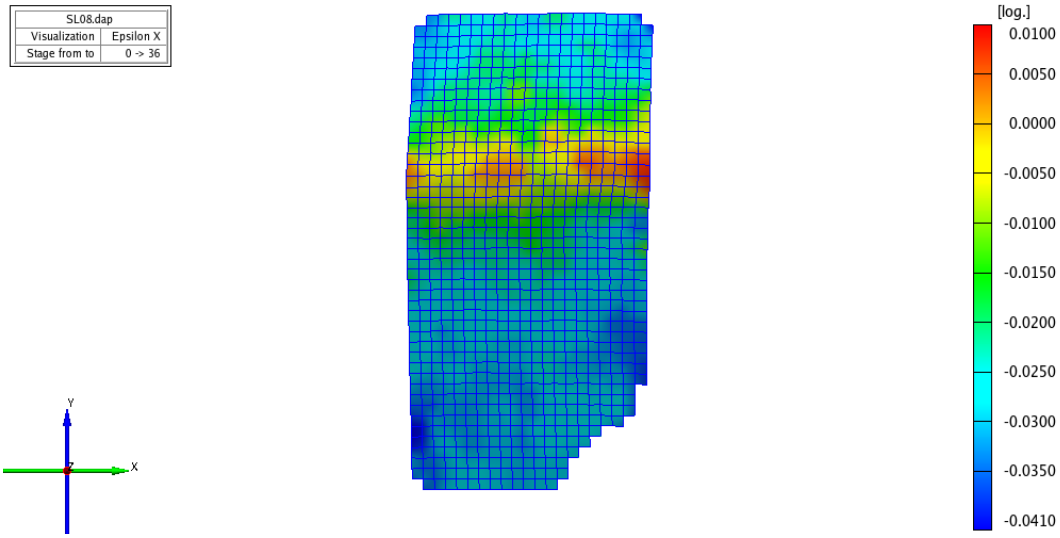

Figure 31. Single layer transverse strain (Time = 210 sec)

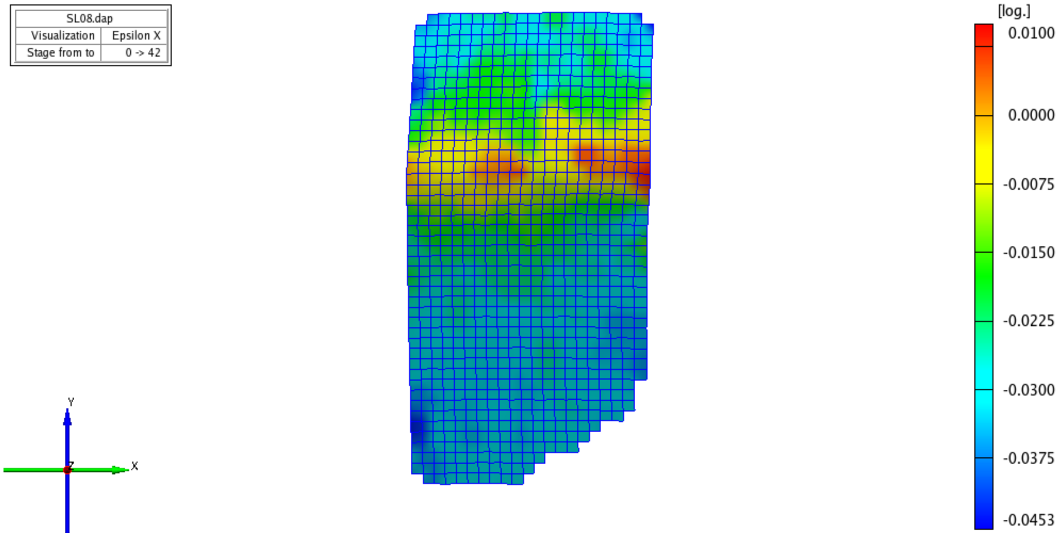

Figure 32. Single layer transverse strain (Time = 240 sec)

The mean strain values in both the transverse and longitudinal directions were estimated in the ARAMIS software and are presented below in Table 13.

Table 13. Single layer specimen average strain values

Stage	Mean Transv. Strain	Mean Long Strain
0	-0.001	0.000
6	-0.002	0.001

12	-0.006	0.001
18	--	0.003
24	-0.016	0.006
30	-0.026	0.010
36	-0.022	0.010
42	-0.023	0.011

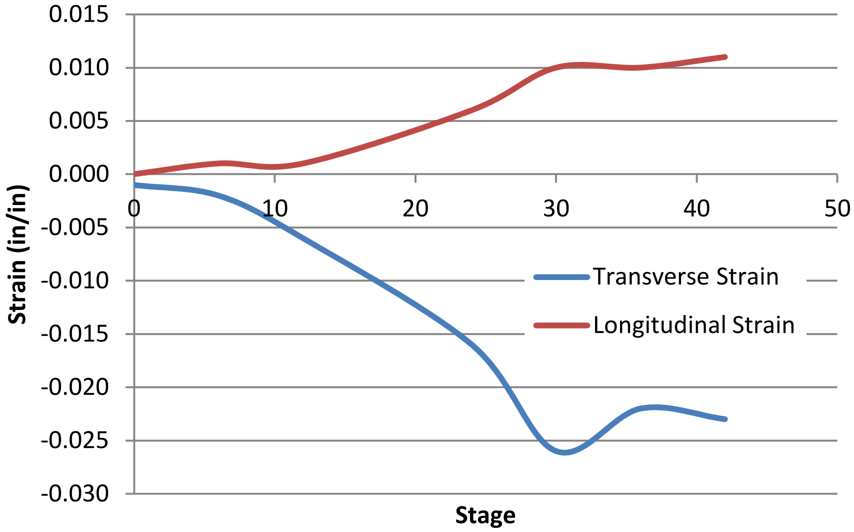

Figure 33. Single layer specimen strain vs. stage

Table 14. Single layer specimen strain values

Stage	Mean Transv. Strain	Mean Long Strain
0	-0.001	0.000
6	-0.002	0.001
12	-0.006	0.001
18	--	0.003
24	-0.016	0.006
30	-0.026	0.010
36	-0.022	0.010

3.5.1.2 Double Layer Specimen

ARAMIS strain measurements in the Y (longitudinal) direction at 30 second intervals for a representative double layer specimen are provided below in Figures 24 thru 40.

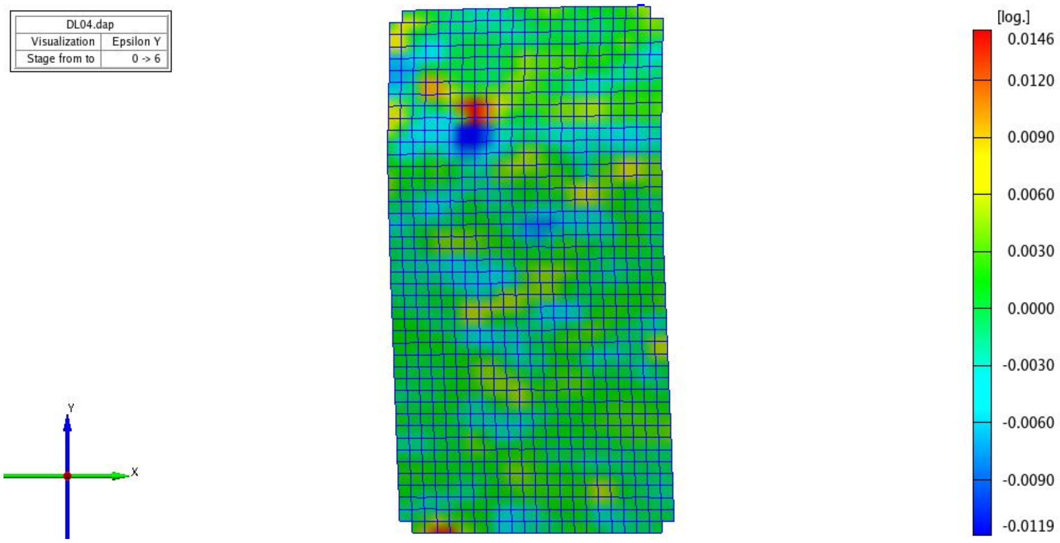

Figure 34. Double layer longitudinal strain (Time = 30 sec)

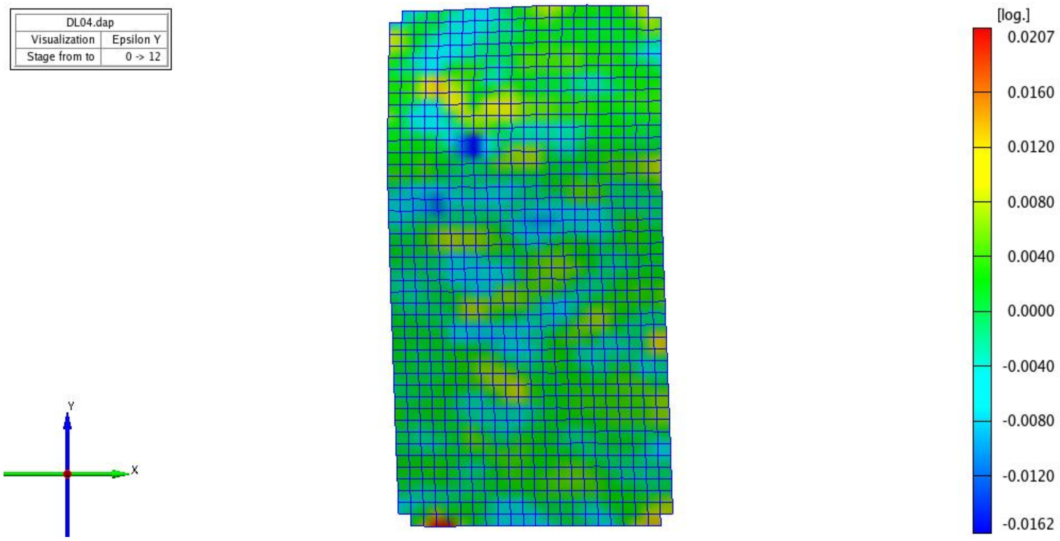

Figure 35. Double layer longitudinal strain (Time = 60 sec)

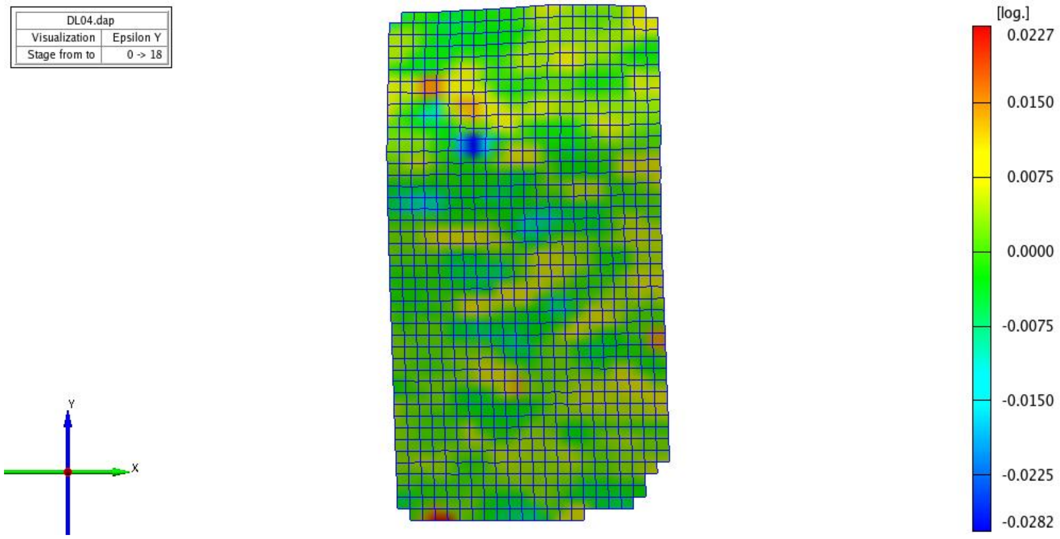

Figure 36. Double layer longitudinal strain (Time = 90 sec)

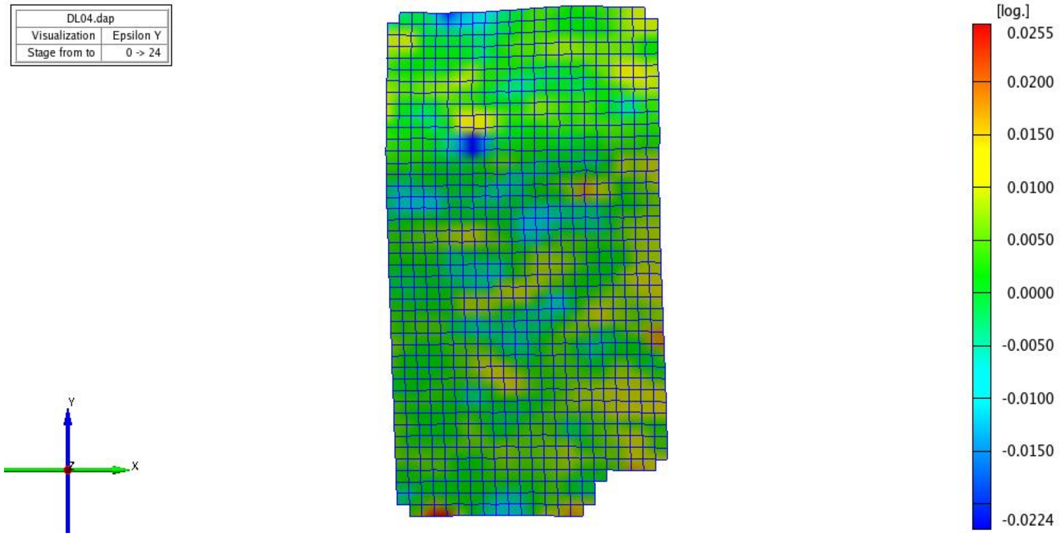

Figure 37. Double layer longitudinal strain (Time = 120 sec)

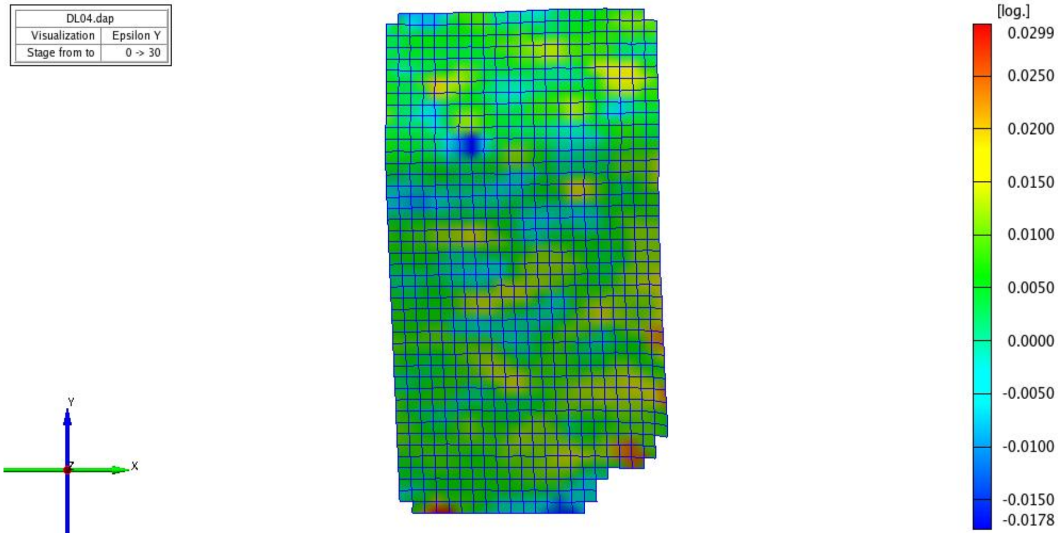

Figure 38. Double layer longitudinal strain (Time = 150 sec)

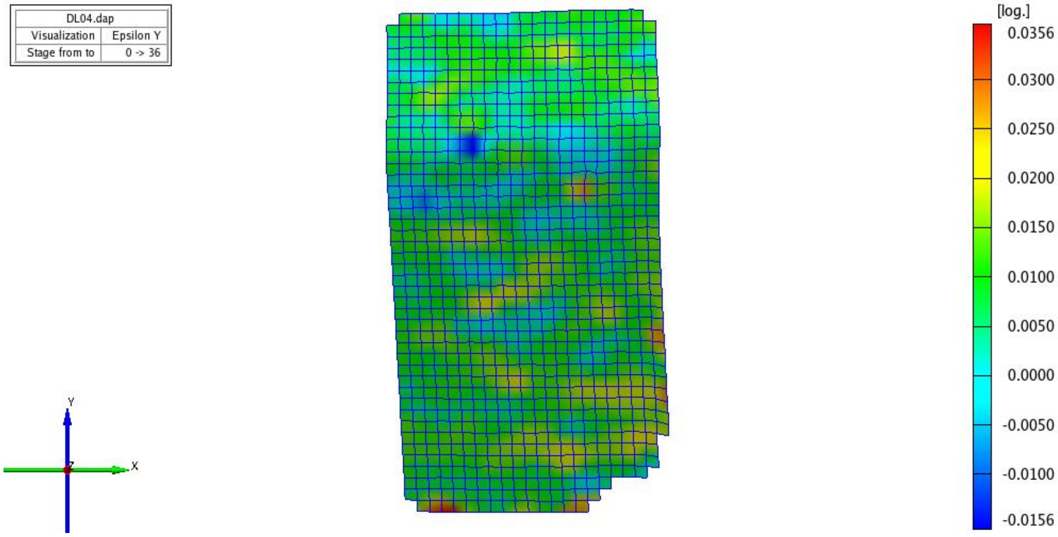

Figure 39. Double layer longitudinal strain (Time = 180 sec)

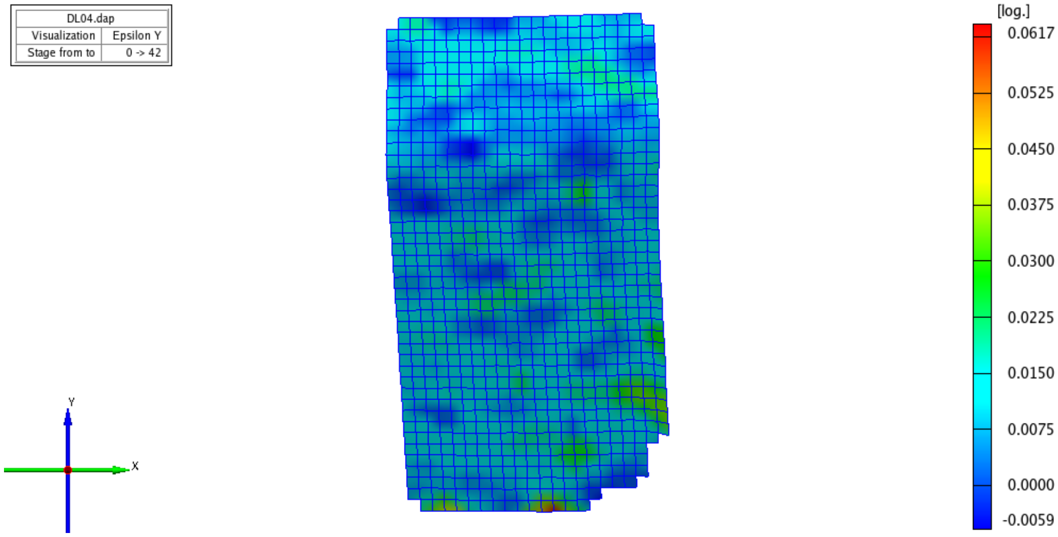

Figure 40. Double layer longitudinal strain (Time = 210 sec)

The average strain values in both the transverse and longitudinal directions were estimated in the ARAMIS software and are presented below in Table 15.

Table 15. Double layer specimen average strain values

Stage	Mean Transv. Strain	Mean Long Strain
0	0.000	0.000
6	0.000	0.000
12	-0.001	0.001
18	-0.002	0.001
24	-0.004	0.003
30	-0.009	0.006
36	-0.017	0.009
42	-0.022	0.011

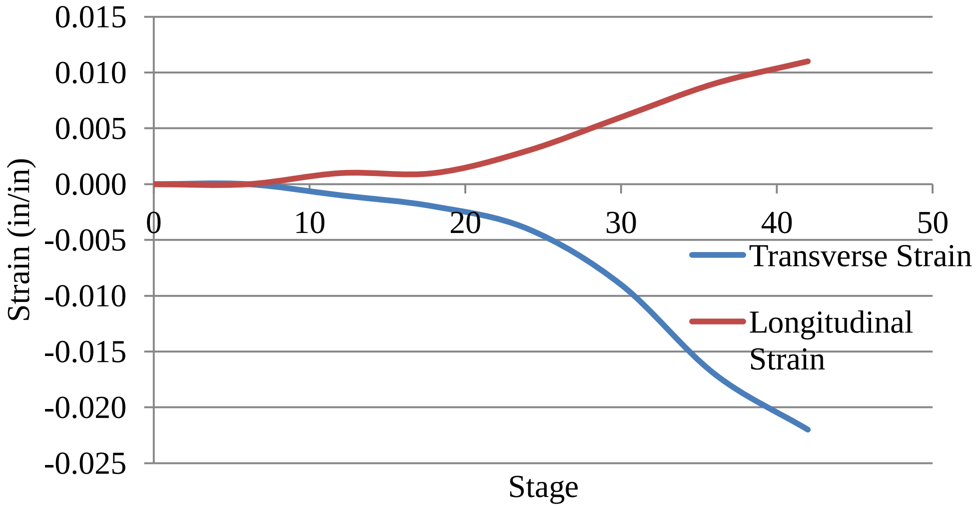

Figure 41. Double layer specimen: strain vs. stage

Table 16. Double layer specimen mean strain values

Stage	Mean Transv. Strain	Mean Long Strain
0	0.000	0.000
6	0.000	0.000
12	-0.001	0.001
18	-0.002	0.001
24	-0.004	0.003
30	-0.009	0.006
36	-0.017	0.009
42	-0.022	0.011

The variation of the longitudinal and transverse strains with respect to stage (time) is shown below in Figures 42 and 43.

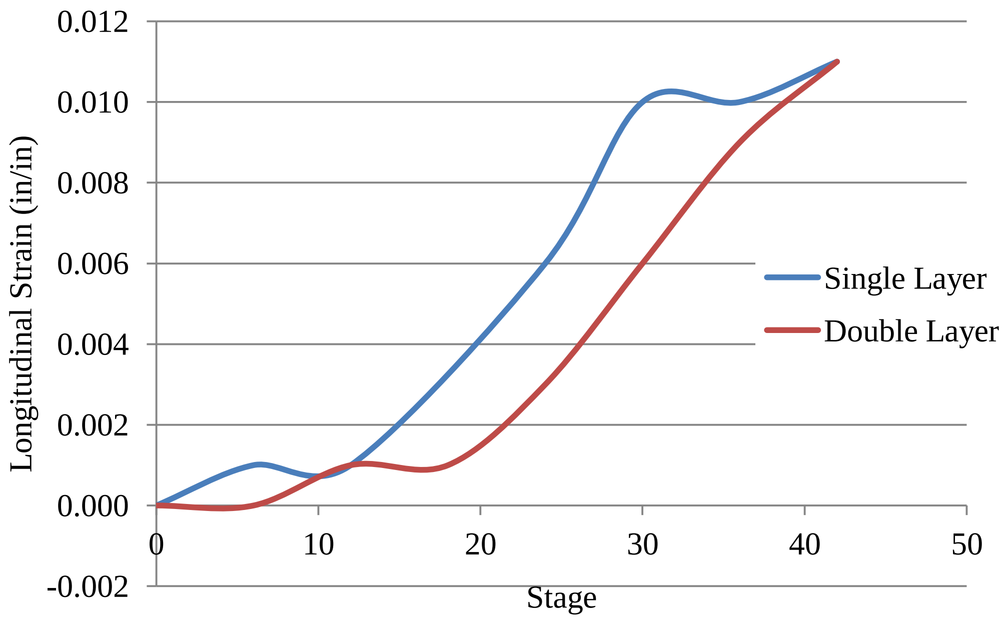

Figure 42. Longitudinal strain vs. Stage

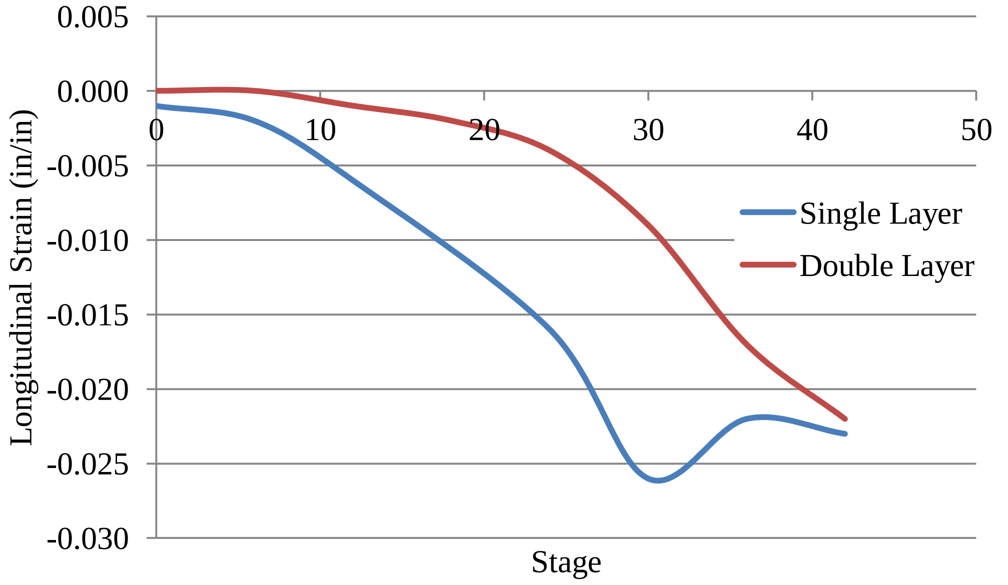

Figure 43. Transverse strain vs. Stage

Strain variations between the single layer and double layer specimen were observed from the ARAMIS results. These differences are most likely due to the longer length of fabric present in the double layer specimen. For the double layer specimen, more stroke is required to overcome the initial crimp region and begin to deform the fabric.

It should be noted that the magnitudes of the measured transverse strains reported are much larger than the corresponding longitudinal strain at the same stage. This phenomenon is observed in the both the single layer and double layer specimen. A second look at the experimental procedure and subsequent data analysis are warranted.

4 ASU UMAT AND FE MODELING DETAILS

4.1 ASU UMAT Version 1.3 Overview

A constitutive material model for dry woven fabrics has been in development at ASU. This model, UMAT48, based mainly on data obtained through experimental testing, is intended for use in the finite element code LS-DYNA. This explicit finite element software package allows for the implementation of a user-defined material model, typically as a FORTRAN subroutine, in the event that a suitable material model is not readily available in the code standard library. UMAT48 utilizes a multi-linear approach to approximate the pre and post-peak stress/strain response of dry woven fabric materials under load. The routine also incorporates a strain-based failure mechanism as well as strain rate dependence as observed in experimentation. The model material is considered orthotropic, with failure in the transverse and longitudinal directions considered separately. The current working version of the material model is 1.3. A brief history of the development of the material model is presented here.

4.1.1 Material Model Evolution

The first version (V1.0) of the material model captured the response of the fabric in the uncrimping, linear elastic loading and linear unloading regions. Failure in the warp and fill directions were coupled (failure in one direction deleted the failed element). All fabric configurations were modeled using one layer of shell elements (SL). The thickness of the fabric shell elements was determined by multiplying the number of layers by the measured fabric thickness (0.011”). For example, the shell elements representing an eight layer fabric scheme would be assigned a thickness of 8 x 0.011” = 0.088”. The simulations were implemented in LS-DYNA Version 970 (Stahlecker, 2007).

V1.1 of the model considered element failure in the warp and fill directions separately. For this version, multiple fabric layer models (ML) were considered as well as SL models. Multiple fabric layers were represented with concentric rows of shell elements. Quality assurance (QA) checks were implemented in order to track the quality of the simulations. All V1.1 models were run with LS-DYNA Version 971 (Bansal, 2007) .

V1.2 incorporated changes to the contact formulations between the fabric layers. Changes were also made to the shear formulation in the model. Both ML and SL models were considered using this version of the material model. All V1.2 models were run using LS-DYNA Version 971.7600 (Zhu, 2009).

The current version of the material model, V1.3, has provided additional functionality to previous versions including the determination of the Cowper-

Symonds parameters for strain-rate dependence, refining the element erosion criteria and determining the optimal value for global damping (Vaidya, 2011).

4.1.2 Stress Strain Response

The stress-strain response modeled in UMAT48 is a piecewise linear function that captures the major characteristic regions observed during tensile testing of Kevlar® fabric. Figure 44 below provides an illustration of these regions.

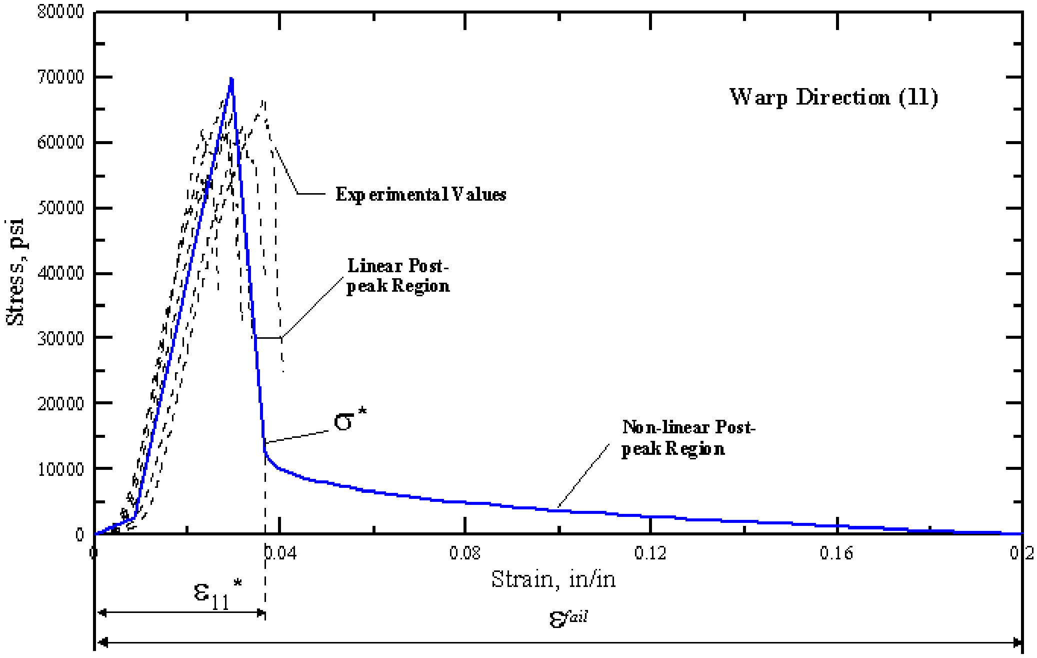

Figure 44. Warp direction stress strain response of Kevlar® 49 fabric (Stahlecker, 2007)

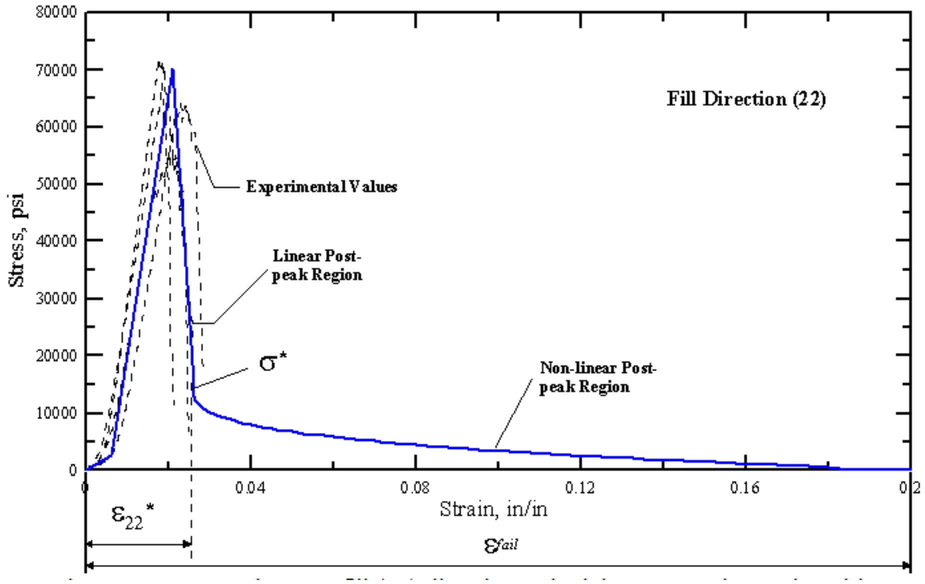

Figure 45. Fill direction stress strain response of Kevlar® 49 fabric (Stahlecker, 2007)

The initial region of low slope is referred to as the uncrimping region and is characterized by the straightening (or uncrimping) of the fabric yarns. The modulus of the fabric in this region is estimated as a fractional value of the equivalent stiffness of the fabric during loading. These fractional values, Excrfac and Eycrfac, were determined to be 0.06 and 0.2 respectively. The fabric weave geometry shifts under tensile load to a position at which point the longitudinal yarns begin taking substantial load. This second region is referred to as the region of linear loading. Although the transition between the uncrimping region and the linear loading region is in actuality non-linear, it is modeled as an abrupt change for ease of implementation. The stiffness of this region is calculated as an equivalent stiffness based on the model geometry. The actual stiffness of the Kevlar® fabric under tensile load must be adjusted due to geometrical differences between the true fabric and the shell elements in the model. Equation 2 below illustrates the scaling that is necessary to account for these differences. The calculation is based on the assumption that the linear stiffness of the simulation elements is equal to the linear stiffness of the actual fabric.

$$E_{FE}A_{FE} = E_{Exp}A_{Exp} \tag{3}$$

The area of one inch of Kevlar® fabric was determined based on measured data and material properties, while the area of one inch of modeled shell elements was determined based on the element thickness. The resulting stiffness of the finite element model material during linear loading was established as

$$E_{FE} = 0.2815E_{Exp} \tag{4}$$

From experimentation the elastic modulus of Kevlar® fabric was determined to be 16.625 Msi, therefore the elastic modulus of the finite element model material in both the warp and fill directions (Ex, Ey) was set at 4.68 Msi. The linear loading region continues to a peak stress value at which point the fabric begins to unload. This region is relatively linear and is modeled as such. The strain at peak stress for the warp and fill directions, emaxx and emaxy, is determined through experimentation to be 0.0223 and 0.0201, respectively. After the material has reached its peak stress, it begins to unload with elastic moduli Exsoftfac and Eysoftfac equal to -2.2 Msi and -5.6 Msi respectively to a post peak stress value of 0.01 Msi (this value is consistent for both the warp and fill directions). The stress in the non-linear post-peak region was calculated by Equations 5 and 6 for the fabric in the warp and fill direction, respectively.

$$\sigma_{11} = \sigma^{*}\left(1 - \left(\frac{\varepsilon_{11} - \varepsilon_{11}^{*}}{\varepsilon_{fail} - \varepsilon_{11}^{*}}\right)^{dfac}\right) \tag{5}$$

$$\sigma_{22} = \sigma^{*}\left(1 - \left(\frac{\varepsilon_{22} - \varepsilon_{22}^{*}}{\varepsilon_{fail} - \varepsilon_{22}^{*}}\right)^{dfac}\right) \tag{6}$$

σ^{*} and ε^{*} are the stress and strain at the onset of the post-peak non-linear region, ε_{fail} is the failure strain in each direction and dfac is the slope of the response curve in the post-peak non-linear region.

4.1.3 Unloading/Reloading/Compression

Due to the violent nature of ballistic testing, the test specimen may experience patterns of unloading and reloading and may even experience compressive forces. Experimental testing was performed to characterize the response of the fabric under cyclic loading. The results from the experimental testing are provided below in Figure 46.

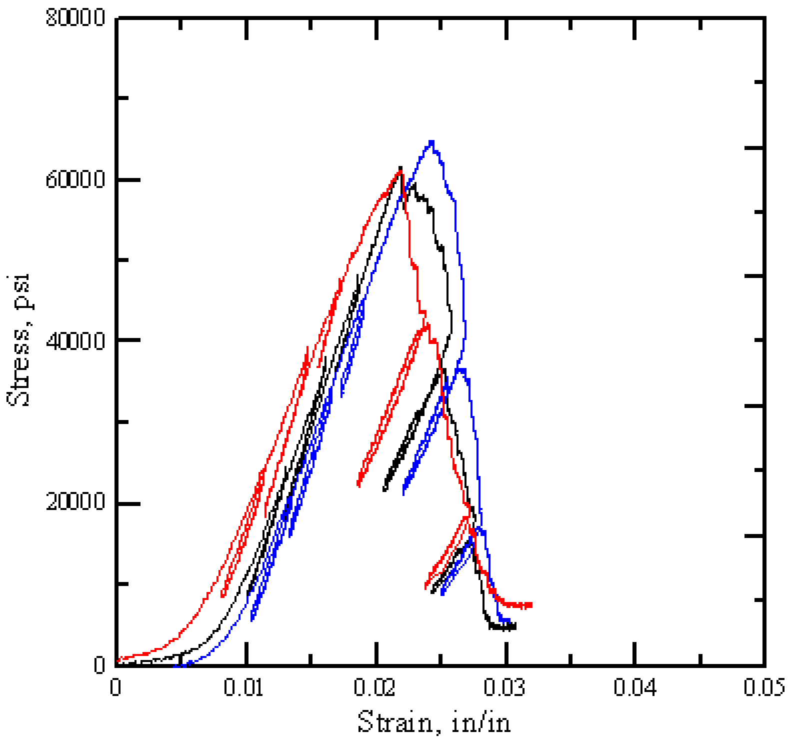

Figure 46. Kevlar® 49 Cyclic Stress Strain Response (Stahlecker, 2007)

To account for any unload/reload cycles in the numerical simulations, the subroutine checks for reversals in stress rate. An unloading rate of Eunlfac=1.5Msi is applied in the instance of cyclic loading. Kevlar® fabric has negligible resistance to compressive stress. However, to avoid numerical instabilities, a very small compressive modulus (Ecompfacp = 0.005 Msi) was implemented in the subroutine to account for any cases when the fabric may experience net compressive stresses.

4.1.4 Strain Rate Dependence

Various studies have been performed on the effect of strain rate on the stress strain response of Kevlar® 49 fabric. Wang and Xia (Experimental and theoretical study on the strain rate and temperature dependence of mechanical behaviour of Kevlar fibre, 1999) performed high strain rate testing of Kevlar® 49 yarn. At strain rates of 1350 /s, they observed an increase in the stiffness as well as the strain at peak stress and the net peak stress value when compared to slower strain rate testing. Results from these tests are provided below in Figure 47.

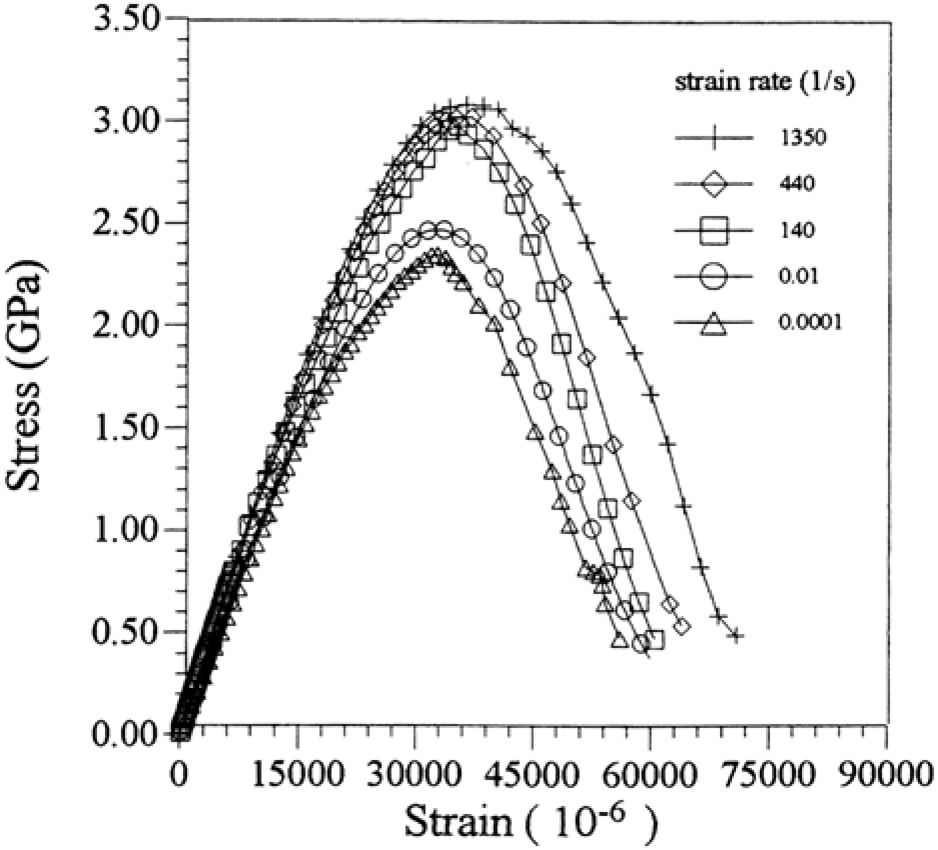

Figure 47. Stress strain response of Kevlar® 49 under high strain rate tensile loading (Wang and Xia, 1999)

(Zhu, Mobasher and Rajan 2011) observed similar results during high strain rate testing of Kevlar® 49 fabric. At strain rates of 170 /s, increases in the stiffness, strain and peak stress and peak stress were observed. Results from these tests are provided below in Figure 48.

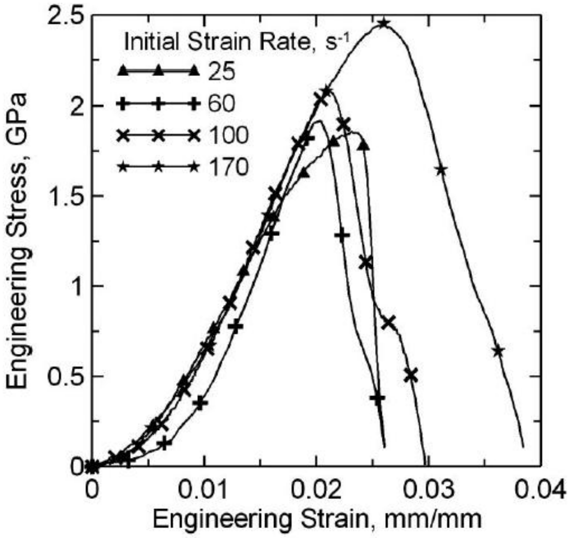

Figure 48. Stress strain response of Kevlar® 49 fabric under high strain rate tensile load (Zhu, Mobasher and Rajan, 2011)

To effectively capture these effects in the numerical simulation, the Cowper-Symonds model (Cowper, et al., 1957) was implemented. The general form of the model is shown below in (7).

$$\sigma^{\max\,(adj)} = \sigma^{\max}\left(1+\frac{\dot{\varepsilon}}{C}\right)^{\frac{1}{P}} \tag{7}$$

The Cowper Symonds model accounts for the increase in peak stress with an increase in applied strain rate. In the UMAT48, the peak stress was assumed to be a function of the Cowper Symonds model. Subsequently, expressions for the adjusted elastic modulus as a function of strain rate were developed and are included here as Equations 8 and 9.

$$E_{11}^{adj} = E_{11}\left(1+\frac{\dot{\varepsilon_{11}}}{C_E}\right)^{\frac{1}{P_E}} \tag{8}$$

$$E_{22}^{adj} = E_{22}\left(1+\frac{\dot{\varepsilon_{22}}}{C_E}\right)^{\frac{1}{P_E}} \tag{9}$$

In the equations above, E_{11}^{adj} and E_{22}^{adj} represent the adjusted elastic moduli in the warp and fill directions, respectively. $\dot{\varepsilon}_{11}$ and $\dot{\varepsilon}_{22}$ are the element strain rates in the warp and fill directions. C_E and P_E are constants that describe the relationship between the peak stress and the strain rate. These constants have been determined through curve fitting routines to be $C_E = 0.005$ and $P_E = 40.0$. Figure 49 illustrates the effect of strain rate on the response of the model fabric.

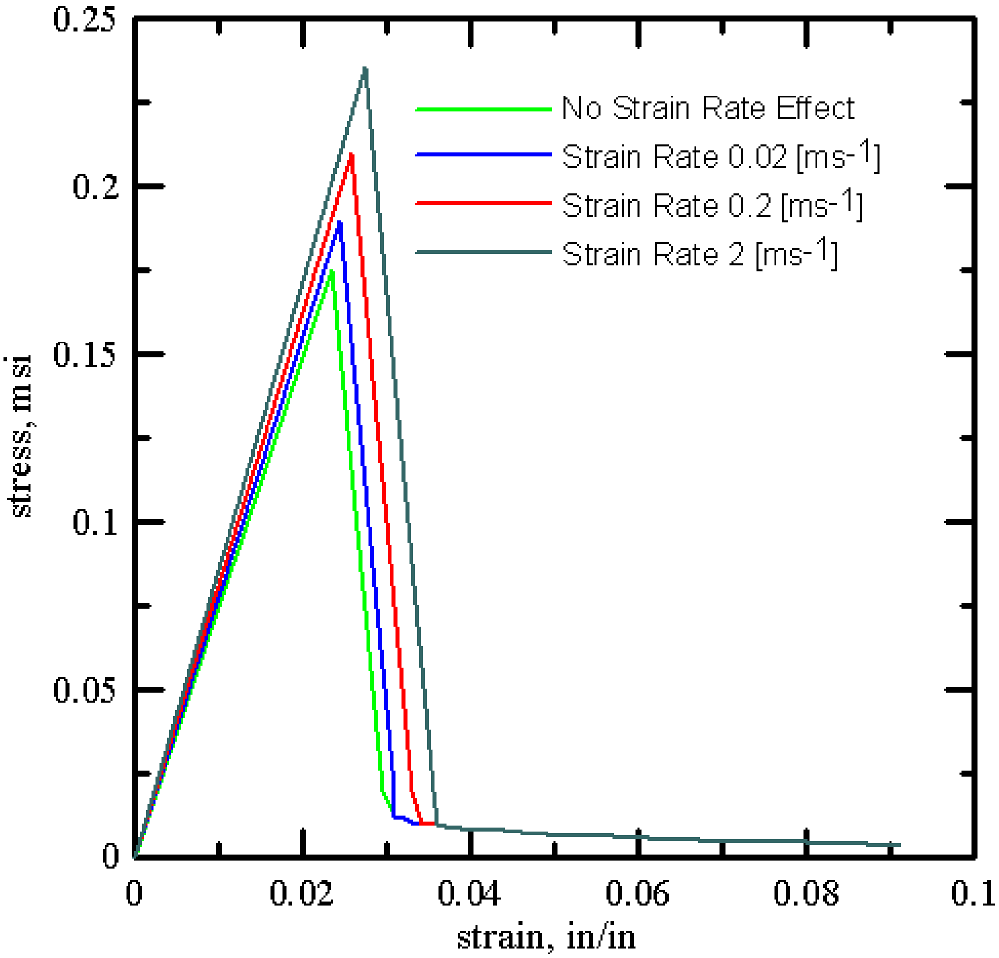

Figure 49. Effect of strain rate on the stress strain response of Kevlar® 49 fabric using the Cowper Symonds model (Bansal, 2007)

4.1.5 Damage and Failure

The UMAT48 considers damage in each orthogonal direction separately. That is, for an element to fail completely it must fail in both the warp and fill directions. The failure criteria defined in the model is strain based. Once an element reaches a specified failure strain (0.1) in both the warp and fill directions the element is deleted from the model. Similarly if the strain in either the warp or fill direction reaches a value of 0.35, the element is removed from the model.

4.1.6 Model Parameters

Parameters used in Version 1.3 of the UMAT48 are provided below in Table 17.

Table 17. UMAT48 parameter values (Vaidya, 2011)

No	Material Constant	Notation	v.1.0	v.1.1	v.1.2	v.1.3
1	Warp Stiffness in Elastic Region (psi 10^6)	Ex	3.2	3.2	3.2	4.68
2	Fill Stiffness in Elastic Region (psi 10^6)	Ey	4.5	4.5	4.5	4.68
3	Warp Direction Crimp Stiffness Factor	Excrfac	0.1	0.1	0.1	0.06
4	Fill Direction Crimp Stiffness Factor	Eycrfac	N/A	N/A	N/A	0.2
5	Warp Direction Post-peak Linear Region Stiffness Factor	Exsoftfac	-2.5	-2.5	-2.5	-2.2
6	Fill Direction Post-peak Linear Region Stiffness Factor	Eysoftfac	N/A	N/A	N/A	-5.6
7	Unloading/Reloading Stiffness Factor	Eunlfac	1.5	1.5	1.5	1.5
8	Compressive Stiffness Factor	Ecompfac	0.005	0.005	0.005	0.005
9	Shear Stiffness (G_{23}) (psi 10^6)	Gyz	0.05	0.05	0.05	0.05
10	Shear Stiffness (G_{23})	Gzx	0.05	0.05	0.05	0.05

	(psi 10^6)					
11	Shear Stiffness Linear Region 1 (G_{12}) (psi 10^6)	Gxy1	0.001	0.001	0.001	0.0006
12	Shear Stiffness Linear Region 2 (G_{12}) (psi 10^6)	Gxy2	0.008	0.008	0.008	0.006
13	Shear Stiffness Linear Region 3 (G_{12}) (psi 10^6)	Gxy3	0.04	0.04	0.04	0.05
14	Shear Stiffness Linear Region 4 (G_{12}) (psi 10^6)	Gxy4	0.3	0.3	0.3	N/A
15	Shear Strain 1 (rad)	gammaxy1	0.35	0.35	0.35	0.25
16	Shear Strain 2 (rad)	gammaxy2	0.5	0.5	0.5	0.35
17	Shear Strain 3 (rad)	gammaxy3	0.57	0.57	0.57	N/A
18	Warp Direction Crimp Strain (in/in)	ecrpx	0.0085	0.0085	0.0085	0.0065
19	Fill Direction Crimp Strain (in/in)	ecrpy	0.006	0.006	0.006	0.0025
20	Warp Direction Strain at Peak Stress (in/in)	emaxx	0.0295	0.0295	0.0295	0.0223
21	Fill Direction Strain at Peak Stress (in/in)	emaxy	0.021	0.021	0.021	0.0201
22	Stress at Post-peak Non-linearity (psi 10^6)	sigpost	0.015	0.005	0.01	0.01
23	Warp Direction Failure Strain (in/in)	efailx	0.2	0.1	0.16	0.2
24	Fill Direction Failure Strain (in/in)	efaily	0.2	0.1	0.16	0.2
25	Cowper-Symonds Factor for Stiffness (ms^{-1})	C(E)	0.005	0.005	0.005	0.005
26	Cowper-Symonds Factor for Stiffness (ms^{-1})	P(E)	40	40	40	40
27	Cowper-Symonds Factor for Strain (ms^{-1})	C(e)	0.005	0.005	0.005	0.005
28	Cowper-Symonds Factor for Strain (ms^{-1})	P(e)	40	40	40	40
29	Post-peak Non-linear Region Factor	dfac	0.3	0.35	0.3	0.3
30	Failure strain of element	fail_e	N/A	0.35	0.35	0.35

4.2 Finite Element Model Details

4.2.1 Model Overview

Figures 50 and 51 illustrate the components included in the finite element simulations of the NASA GRC ballistic testing.

Figure 50. FE model of ring and Kevlar® fabric

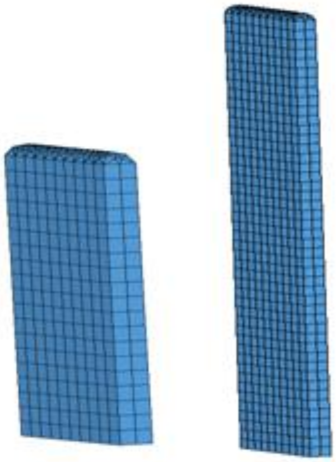

Figure 51. FE model of old (L) and new (R) projectiles

The orientation of the ring is shown in Figure 52 below. The global X axis is aligned with the projectile path of motion. The ring is therefore oriented at a 15 degree down angle to the global X axis.

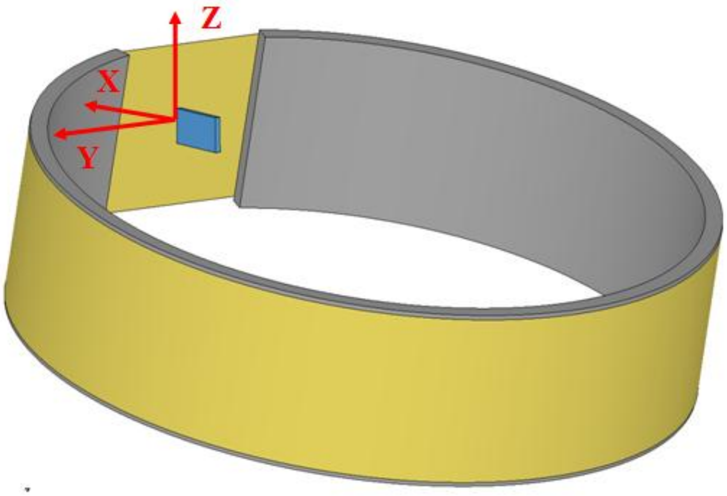

Figure 52. Global FE coordinate system

The projectile orientation and degrees of freedom are illustrated below in Figure 53.

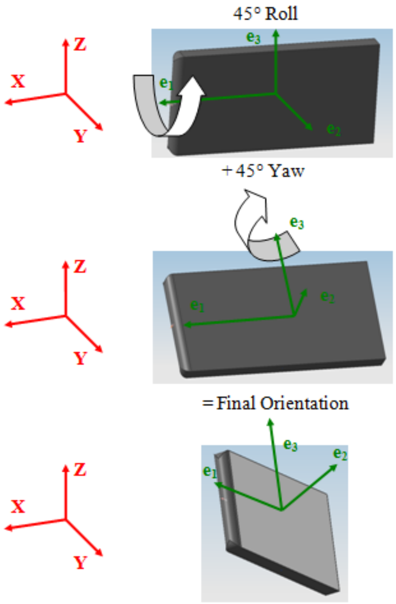

Figure 53. Projectile Orientation Illustration (Stahlecker, 2007)

4.2.2 Elements

Four-noded linear Belytschko-Tsay shell elements were specified for the Kevlar® fabric. Shell elements were modeled at 0.25” x 0.25” square with a thickness of 0.044”. This thickness is based on the effective thickness of Kevlar® 49 fabric of 0.011” and represents the thickness of 4 individual layers of fabric. The modeling of multiple layers of fabric in one layer of FE shell elements allows for a lower computational cost without sacrificing accuracy. This modeling methodology allows for the determination of partial damage through the containment structure thickness as well as allows for the modeling of the interaction between fabric layers.

Eight-noded linear hexahedral constant stress solid brick elements were used to model the ring body. An element size of 0.25” was specified during meshing, which is fine enough to accurately capture any stresses that may be experienced by these parts yet coarse enough to limit the computational cost (Vaidya, 2011). The projectiles were meshed using a combination of linear brick elements for the projectile bodies and linear tetrahedral elements for the projectile tips. Mesh sizes of 0.1” for the tip and 0.15” for the body were specified for the new projectile while mesh sizes of 0.15 for the tip and 0.2 for the body were specified for the old projectile. Tetrahedral elements were utilized to mesh the projectile tips due to their good conformance to the true geometry at this end of the body.

4.2.3 Materials

The UMAT48 was implemented as the model material for the fabric shell elements. The ring and projectiles were modeled using the elasto-plastic material model *MAT_JOHNSON_COOK.

4.2.4 Boundary Conditions

Finite element models associated with Phases I, II and III of the FAA project were previously developed under the assumption that, due to the short time frame of the testing and the mass of the steel test ring, the effects of the boundary conditions imposed during experimental ballistic testing on the numerical results to be negligible. An example of an FE model neglecting these boundary support conditions is shown below in Figure 54. All elements associated with this model are free to translate/rotate globally in space under the influence of the steel projectile.

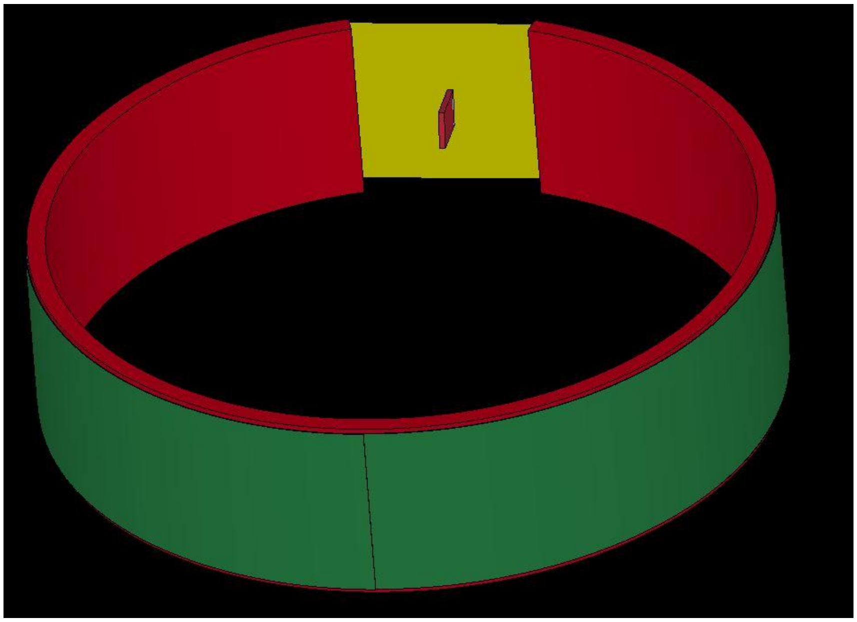

Figure 54. Unrestrained, Unbraced Finite Element Model

The support conditions present during NASA GRC ballistic testing are shown here in Figure 55. The effect that the imposition of these boundary conditions would have on the finite element model results was unknown. The goal of this study was to ascertain the scope and nature of the impacts that the inclusion of the experimental boundary conditions has on the results of the numerical simulations.

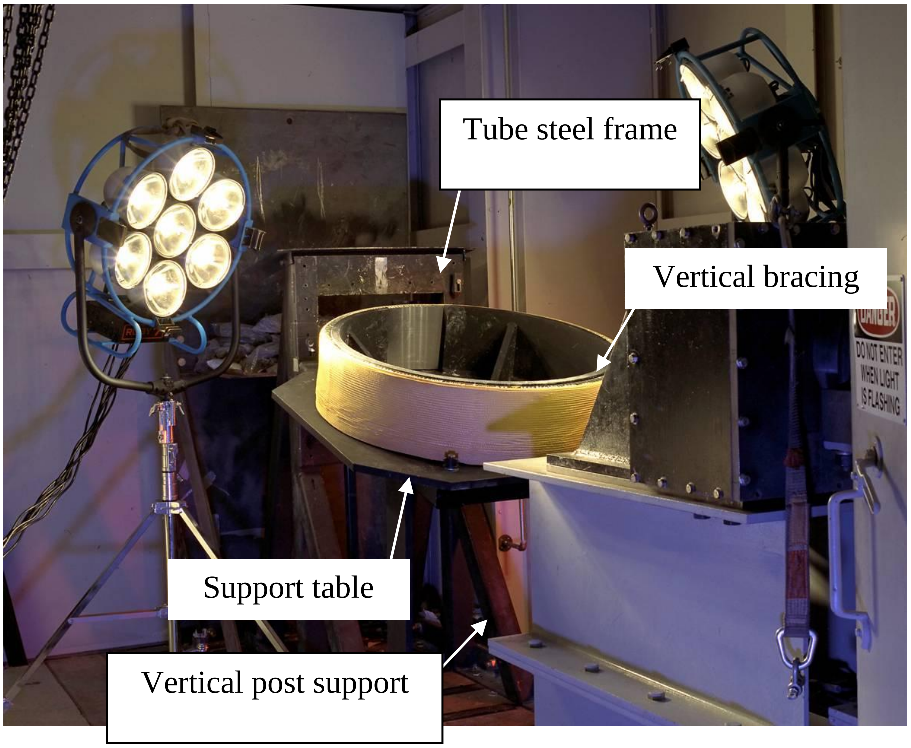

Figure 55. Experimental test setup: support apparatus configuration

4.2.4.1 Experimental Boundary Conditions

The support structure utilized during experimental ballistic testing is shown above in Figure 55. The steel test ring was welded to a 1” thick x 47.5” square steel base plate. Two (2) 1” x 8.5” x 8.5” steel braces, located at 45° either side of the centerline of the ring opening, were welded to both the ring and to the steel base plate as shown in the figure above, providing lateral support to the walls of the ring. A schematic diagram of the ring/bracing system is shown below in Figure 56.

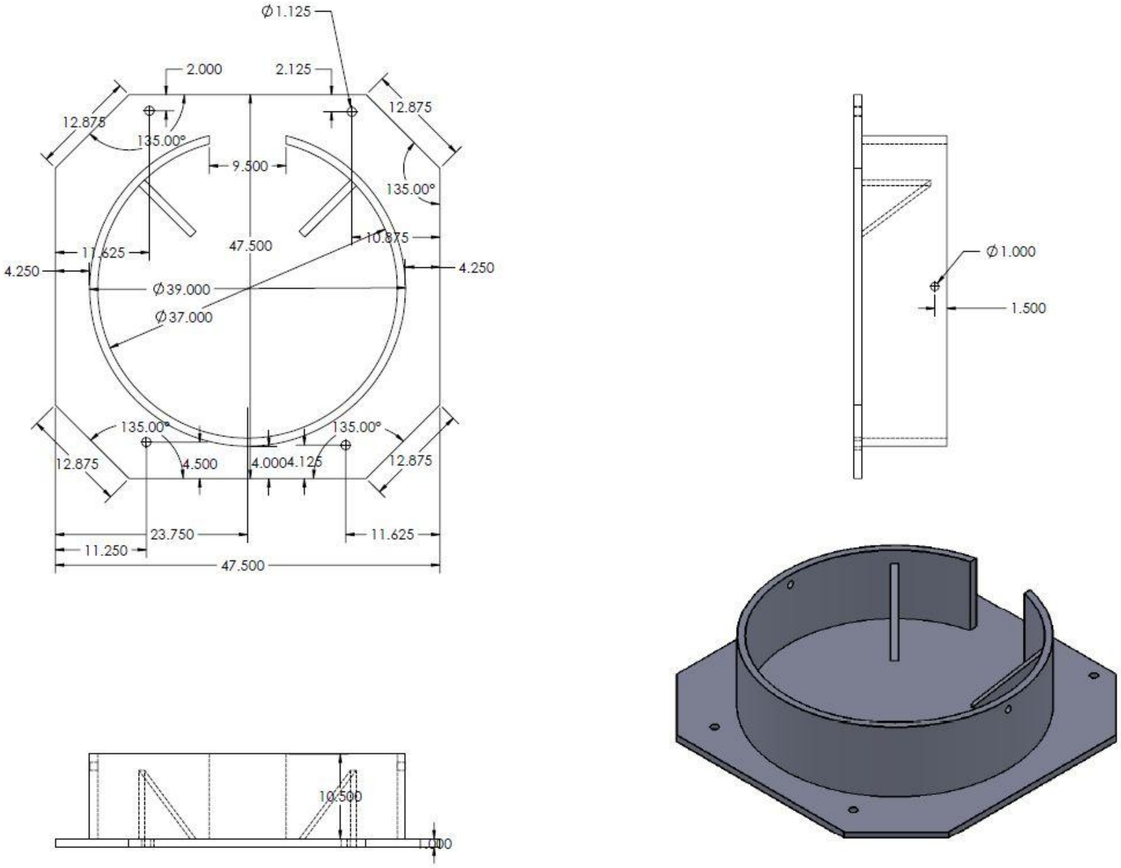

Figure 56. Schematic diagram of braced ring apparatus

This ring/brace/base plate structure was supported against lateral translation by the braced tube steel frame shown, the tube steel measuring 4” x 4” x 3/8”. Vertical support of the ring platform was provided by the steel post shown. This support structure was in turn bolted to a 12” thick steel plate embedded in concrete.

4.2.4.2 Modeling of Boundary Conditions

Finite element simulations of the experimental testing were prepared using LS-DYNA finite element code, Version R4.2.1, double precision. All simulations were performed on a Windows 7 64 Bit operating system.

The lateral support provided by the tube steel frame was approximated as being perfectly rigid. Although some vibrations and/or translations may be present during testing, these were not accounted for during testing and the effects of these are assumed to be negligible for this analysis due to the robustness of the ring support structure. To model the effect of the support structure, all six (6) degrees-of-freedom associated with all nodes located along the bottom-most surface of the ring were constrained with respect to the global coordinate system. The 1” x 8.5” x 8.5” steel braces present during testing were added to the finite element models to simulate the lateral stiffness provided to the ring during experimentation. To simulate the weld affixing the braces to the steel base plate, the nodes along the bottom-most surface of the braces were also fixed for translation, similar to the ring nodes. An example of a restrained, braced FE model is provided below in Figure 57. Note that the translational restraints imposed on the ring nodes cannot be seen in the figure although they are present in the model.

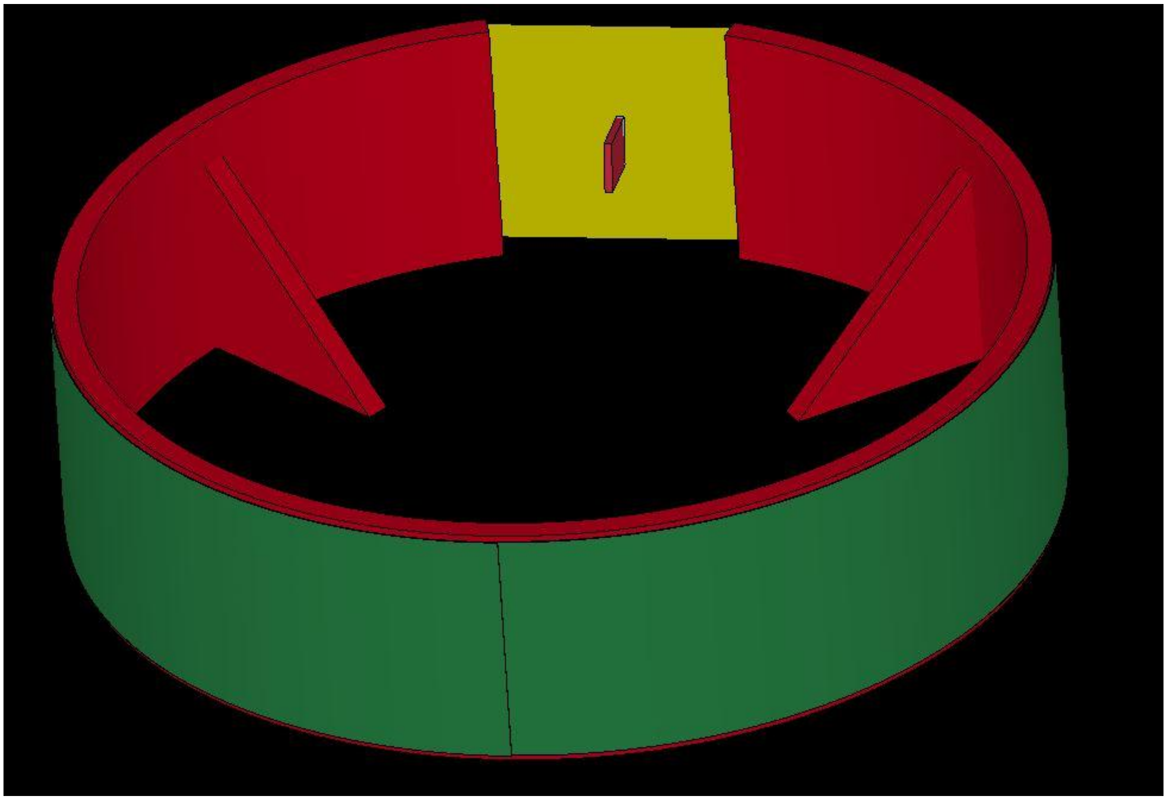

Figure 57. Restrained, Braced Finite Element Model

To study the effects that each individual boundary condition has on the results of the numerical simulations, each support was added separately and analyzed. A list of the model suites prepared in association with this study is provided below in Table 18.

Table 18. List of Model Suites: Boundary Condition Study

Model Suite Name	Description
Fixed_JCRing_SMS_Braced	Fixed base with vertical braces: SMS
Fixed_JCRing_SMS_Unbraced	Fixed base no vertical braces: SMS
Free_JCRing_SMS_Braced	Free base with vertical braces: SMS
Free_JCRing_SMS_Unbraced	Free base no vertical braces: SMS
Fixed_JCRing_SMS_Braced	Fixed base with vertical braces: CMS
Fixed_JCRing_SMS_Unbraced	Fixed base no vertical braces: CMS
Free_JCRing_SMS_Braced	Free base with vertical braces: CMS
Free_JCRing_SMS_Unbraced	Free base no vertical braces: CMS

After the model suites listed above were analyzed, a comparative study was prepared to determine the effect of each individual boundary condition on the FE model results. A list of the comparisons performed is included below in Table 19.

Table 19. List of Model Suite Comparisons

	Comparison Descriptions
1	Fixed models vs. Free models (Braced)
2	Fixed models vs. Free models (Unbraced)
3	Braced models vs. Unbraced models (Fixed)
4	Braced models vs. Unbraced models (Free)

The comparisons listed above were performed for both the CMS (concentric modeling scheme) and SMS (spiral modeling scheme) fabric configurations. These fabric configurations are explained in greater detail below.

4.2.5 Fabric Wrapping Scheme

Previous versions of finite element simulations of the NASA ballistic testing considered the fabric layers to be concentric. This concentric modeling scheme (CMS) provided reasonable results (Rajan, et al. 2004). Recent studies have been performed (Vaida 2011) to determine the benefit of modeling the fabric wrapping as a spiral modeling scheme (SMS) as the fabric is configured during experimental testing. Figure 58 shows the configuration of the SMS at the region of overlap at the backside of the steel ring.

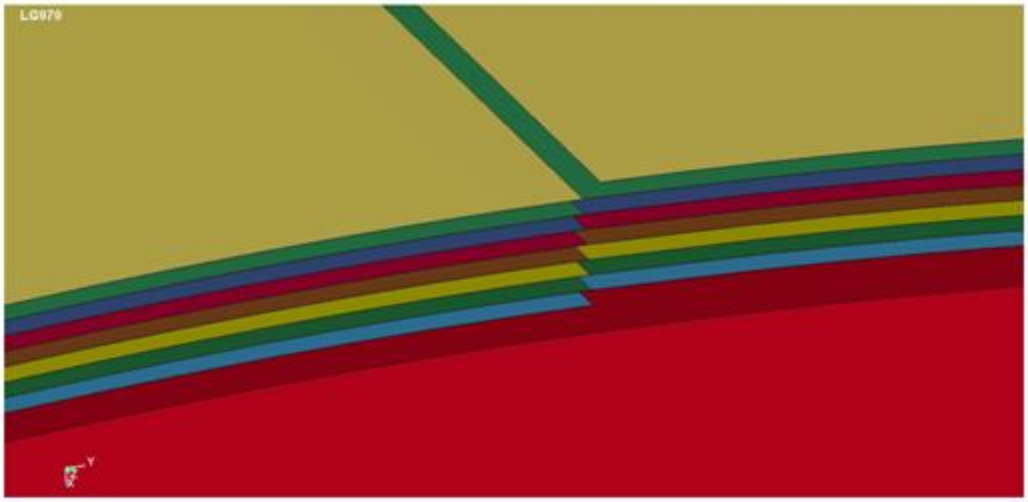

Figure 58. Fabric configuration at region of overlap: Spiral Modeling Scheme

A contact definition was provided to simulate the adhesion of the leading edge of the fabric to the ring and the trailing edge of the fabric to the fabric wrap. Additional damping was defined to remove resultant stress waves that appeared after modifying the wrapping configuration. The results from the wrapping configuration study showed that the SMS fabric configuration provided acceptable results when compared to the experimental testing (Vaida, 2011).

4.2.6 Keyword Description

A brief description of the keywords utilized in the FAA model suite is provided below. An example set of keyword cards with values is included with this report in APPENDIX B.

*CONTACT_AUTOMATIC_SURFACE_TO_SURFACE was used to define the interaction between the fabric layers, between the ring and the fabric and between the projectile and the fabric. The previously determined (Rajan, et al., 2009) static and dynamic coefficients of friction of 0.1 (steel to Kevlar®) and

0.2 (Kevlar® to Kevlar®) are defined as well as the viscous damping coefficients (Vaidya, 2011). The damping coefficients (VDC) values of 10 and 20 percent are specified for steel to fabric and fabric to fabric contact, respectively. In the *CONTROL_TIMESTEP card the initial timestep is given to LS-DYNA to calculate. A scale factor for the computed timestep of 0.75 is specified for all models. The LS-DYNA manual recommends a default value of 0.9 unless modeling high explosive loading, in which case the recommended value is 0.67. 0.75 is an appropriate value to represent a higher velocity type load. This requires that the timestep used in the solution is ¾ of the timestep calculated by LS-DYNA, allowing for a more stable solution. The termination time for each model is specified based on the duration of the test in *CONTROL_TERMINATION. The typical value for the termination time is set at 0.75 ms. The *CONTROL_SHELL keyword establishes criteria regarding the shell elements in the model. The warpage angle (limit deformation angle at which point a warning is issued to the user) is set to 20 degrees. The default shell theory is set to Belytschko Tsay formulation. Also, second order objective stress updates and invariant node numbering is turned on as recommended by LSTC for high velocity type loading.

5 OVERVIEW OF MAT234: MAT_VISCOELASTIC_LOOSE_FABRIC

5.1 Objective

At the onset of this project, the numerical simulation of dry woven fabrics for use in structural ballistic applications was fairly young. Since then, some work has been done by others, concurrently with this project, to develop reliable models for these materials. The material model MAT 234: *MAT_VISCOELASTIC_LOOSE_FABRIC, developed by Ivelin Ivanov and Ala Tabiei (Ivanov, et al., 2004), considers a micromechanical approach to model the response of dry woven fabrics in the non-linear finite element software LS-DYNA. As part of the validation process for UMAT48, it was desired to study the mechanics of MAT 234 and compare the results obtained from finite element models utilizing MAT 234 with the results when utilizing UMAT48. The parameter values necessary to model Kevlar® 49 fabric with the MAT 234 material model were calculated from the keyword description for MAT234 (see APPENDIX C)(LS-DYNA, 2007). MAT234 was then implemented in the FE simulations of NASA ballistic testing and the results were compared against the same FE models run with the ASU UMAT V1.3.

5.2 Overview of Material Model

5.2.1 Material Model Mechanics

MAT 234 utilizes a micromechanical approach to model behaviors that are specific to dry woven fabrics including the initial straightening/uncrimping of the fabric yarns under tensile load as well as the trellising and interlock of the yarns under shear deformation of the fabric. The model is based on a representative volume cell (RVC) as shown below in Figure 59.

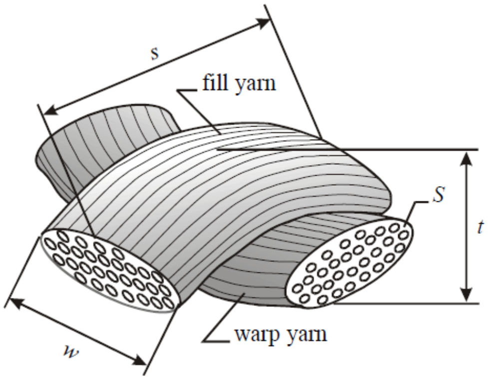

Figure 59. MAT 234 Representative Volume Cell

As shown in the figure above, the RVC is based on the deformed geometry of the fabric, namely an undulated fill yarn crossed over an undulated warp yarn. This geometry is modeled as shown below in Figure 60 as linear viscoelastic elements connected by pin joint connections to rigid link elements. This configuration allows for the straightening of the linear elements when subjected to tensile forces as well as the trellising and interlocking of the fiber elements when subjected to shear forces/deformation.

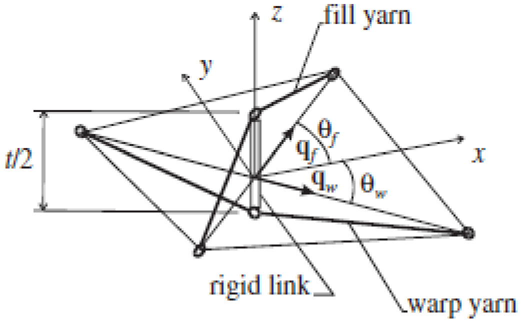

Figure 60. Mechanistic Representative Volume Cell Model

A schematic depicting the shear deformation and interlock mechanism of the fabric material is provided in Figure 61.

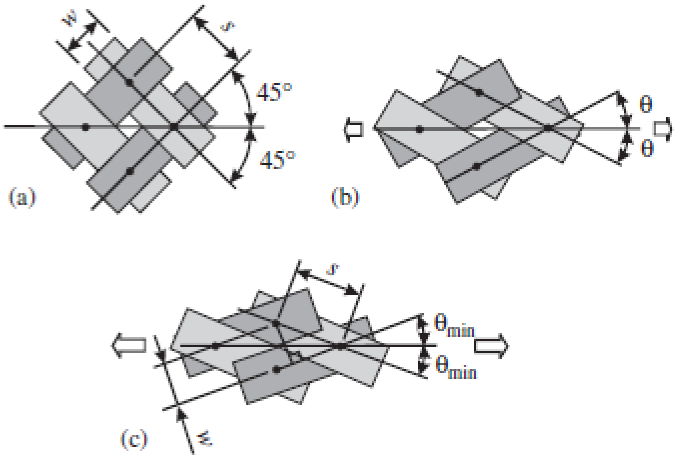

Figure 61. Trellising Mechanism of Fabrics: (a) Undeformed State (b) Slightly Deformed Fabric and (c) Fabric Deformed to Interlock

These mechanisms are specific to woven fabrics and are have a significant impact on the response characteristics of these materials.

5.2.2 Viscoelastic Material Model

Polymeric materials at room temperature exhibit viscoelastic behavior including creep and stress relaxation. Due to the short time duration of ballistic loading, the long-term effects of viscoelasticity are assumed to have no significant effect and therefore are not considered. To capture the instantaneous viscoelastic response of the fabric material, MAT 234 implements a three (3) element phenomenological material model consisting of a modified Maxwell element (single spring element, Element ‘a’) and a Kelvin-Voight Element (spring and dashpot elements in parallel, Element ‘b’). A schematic of this viscoelastic model is provided below in Figure 62.

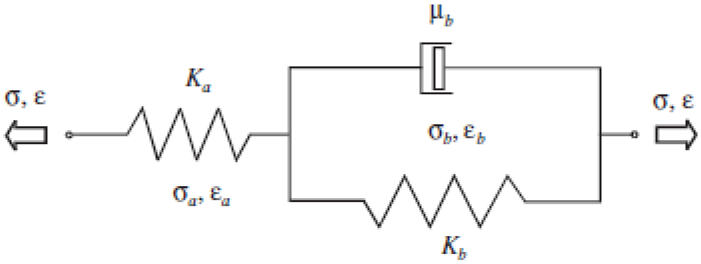

Figure 62. MAT 234 (3) Element Viscoelasticity Model

Based on the response characteristics of these elements, the phenomenological model attempts to capture both the instantaneous response and the delayed response of the material under tensile loading. Using the equilibrium of the model, the governing differential equation can be derived and is included here as shown below.

$$(K_a + K_b)\sigma + \mu_b\dot{\sigma} = K_a K_b \varepsilon + \mu_b K_a \dot{\varepsilon} \tag{10}$$

where K_a is the Hookian spring coefficient (EKA), μ_b is the viscosity coefficient (VMB). Using this governing equation, the response curves in the elastic loading region for MAT 234 evaluated over a range of strain rates can be generated and compared against the curves generated by the user-defined material model. By utilizing this curve fitting methodology, it was possible to determine the most appropriate values for the parameters Ka and μ_b in order to most closely match the response curves from the ASU UMAT. A detailed description of the material cared parameters is available in LS-DYNA (LS-DYNA, 2007).

5.2.3 Preliminary Parameter Values

The parameter values implemented with MAT 234 for Kevlar® 49 yarn are provided below in Table 20 with the standard base units used in this project

Table 20. MAT234 Parameter Values for Kevlar® 49 fabric

Description	Variable	Value
Mass Density (lb-s^2/in^4)	RO	13.46E-5
Young's Modulus (Longitudinal, Msi)	E1	8.397
Young's Modulus (Transverse, Msi)	E2	1
Longitudinal Shear Modulus (Msi)	G12	2.38
Ultimate Strain at Failure	EU	0.042
Yarn Locking Angle (Degrees)	THL	17
Initial Braid Angle (Degrees)	THI	45
Transition Angle to Locking (Degrees)	TA	3
Yarn Width (in)	W	0.049
Span Between the Yarns (in)	s	0.058824
Real Yarn Thickness (in)	T	0.011
Effective Yarn Thickness (in)	H	6.10e-3
Yarn Cross Sectional Area (in^2)	S	1.70E-4
Elastic Constant of Element 'a' (Msi)	EKA	11.75
Ultimate Strain of Element 'a'	EUA	0.0216
Damping Coefficient of Element 'b' (Msi)	VMB	3.25e-3
Coefficient of Friction Between the Fibers	C	0.2
Transverse Shear Modulus (Msi)	G23	2.38
Elastic Constant of Element 'b' (Msi)	EKB	29.43
AOPT V1	V1	-0.2588
AOPT V2	V2	0.0
AOPT V3	V3	0.9659

The values above were determined via experimental testing, calculated based on the fabric geometry and estimated using curve fitting procedures and simple regression techniques. Details of the calculations used to compute these values are provided here.

5.2.3.1 Mass Density, RO

The mass density specified by DuPont for Kevlar® 49 is 1.44 g/cm^3. The unit conversion to the base units is shown below.

$$1.44\frac{g}{cm^3}\left(\frac{1kg}{1000g}\right)\left(\frac{2.20463lbm}{1kg}\right)\left(\frac{1lbf-s^2}{32.2lbm-ft}\right)\left(\frac{1ft}{12in}\right)\left(\frac{2.54cm}{1in}\right)^3=13.464E-5\frac{lbf-s^2}{in} \qquad (11)$$

5.2.3.2 Longitudinal Young's Modulus, E1

Young's Modulus in the longitudinal direction is specified at 8.397 Msi. This value was determined experimentally by performing static tension testing on woven fabric yarn with a gage length of 8". The stress strain response of Kevlar® yarn samples is provided below.

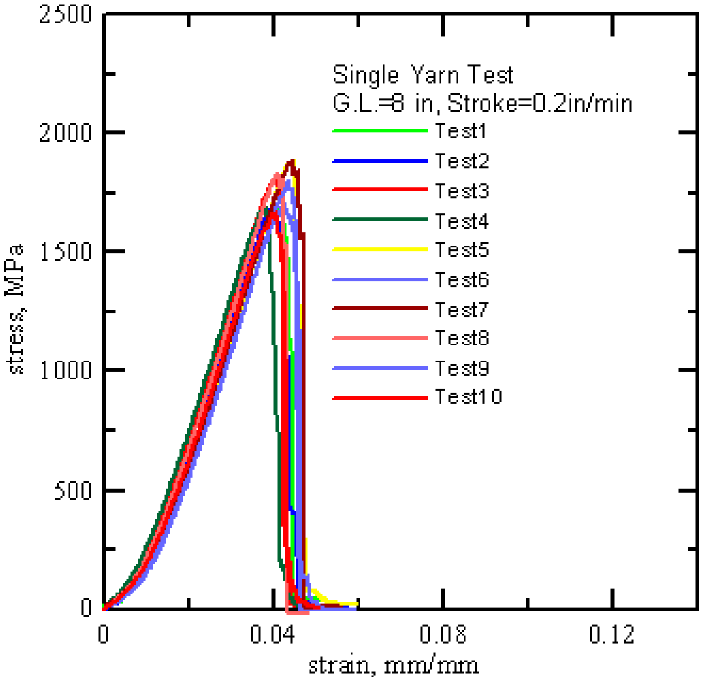

Figure 63. Stress Strain Response of Kevlar® Yarn: Gage Length = 8"

Experimental values for the modulus of Kevlar® yarn vary widely with strain rate and gage length. Based on static tension testing of Kevlar® 49 yarn performed at

ASU the modulus ranged from approximately 3 Msi (gage length L=2”) to approximately 11 Msi (gage length L=17”). Results from the 8” gage length specimen were selected as they reduced the effects of the length on the stiffness of the sample present in the short gage length samples and mitigated the effects of any non-uniform tension due to misalignment of the sample on the test apparatus characteristic of longer gage length samples.

5.2.3.3 Transverse Direction Modulus, E2

It was not possible to experimentally find the value of E_2 for a Kevlar®49 fabric yarn. It is known that the modulus in the transverse direction is relatively much smaller than in the longitudinal direction. Hence a value of 1 Msi was assumed and the value is approximately 11% of E_1..

5.2.3.4 Longitudinal Shear Modulus, G12

The longitudinal Shear Modulus, G12 for the yarn is specified at 2.38 Msi. This value was determined experimentally by measuring the torsional response of a mass suspended from a known length of Kevlar® yarn (Determination of Shear Modulus of Single Fibers, 1999). The torsional response of the yarn allows for the evaluation of the shear constants in the longitudinal direction of the fiber.

5.2.3.5 Ultimate Strain at Failure, EU

The ultimate strain at failure for a Kevlar® 49 yarn is specified as 0.042. This value was determined experimentally by ASU (Zhu, 2009) and represents the strain at peak stress for a single yarn specimen removed from woven fabric for a gage length of 8” as shown above in Figure 63.

5.2.3.6 Yarn Locking Angle, THL

The yarn locking angle represents the point in the shear deformation of the fabric at which yarn interlock begins. The angle is determined by the width, w of the fabric yarns (0.04895 in) and the yarn span, s (0.058824 in). The minimum braid angle, $\theta_{\min}$, as shown in Figure 61, is calculated by Equation 12.

$$\sin(2\theta_{\min}) = \frac{w}{s} \tag{12}$$

The yarn locking angle is the difference between the initial braid angle (45°) and $\theta_{\min.}$

$$THL = 45 - \theta_{min} \tag{13}$$

The representative geometry of the fabric at interlock is shown above in Figure 61. For the geometry specified for this problem, the yarn locking angle is specified at 17°. The calculation of this value is shown below.

$$\begin{aligned} &w = 0.049in \\ &s = 0.058824 \\ &\theta_{\min} = \left[\sin^{-1}\left(\frac{0.049}{0.058824}\right)\right] / 2 = 28.20° \\ &THL = 45 - 28.20 = 16.8°(say17°) \end{aligned}$$

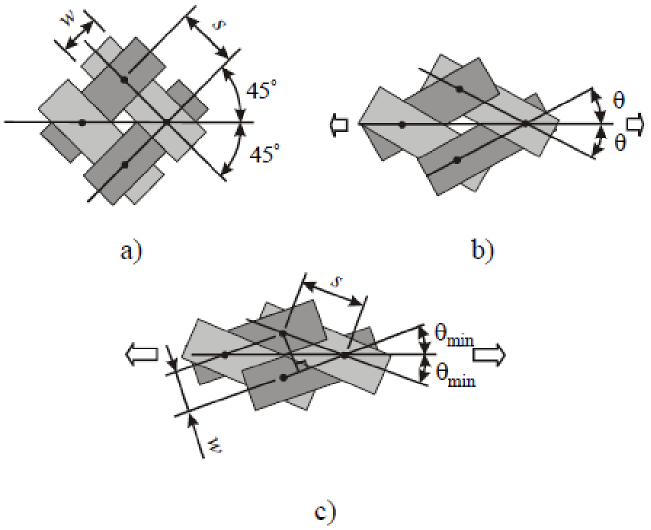

Figure 64. (a) Initial undeformed geometry of fabric; (b) General deformed geometry of fabric; (c) Geometry of fabric at onset of interlock phenomenon

5.2.3.7 Initial Braid Angle

The initial braid angle of the material is ½ of the total angle between Warp and Fill direction yarns in the undeformed state. Because the fill and warp yarns are initially orthogonal, the value for THI is set at 45°.

5.2.3.8 Transition Angle to Locking, TA

The transition angle to locking (Δθ in Figure 65 below).provides a small angle during which the locking mechanism between the yarns can take effect. The value of TA is set to 3 degrees.

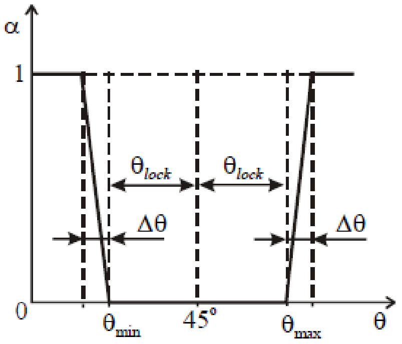

Figure 65. Lateral Contact Factor, α vs average braid angle, θ

5.2.3.9 Yarn Width, W

The yarn width, W is specified at a value of 0.049 in. This value was determined experimentally by impregnating a sample of Kevlar® fabric with epoxy in a stress free, undeformed state, then preparing a cross section of the sample and measuring the geometry of the undeformed yarns with a microscope (Bansal, 2007). This value represents the average width of the warp and fill yarns. Results from the yarn geometry analysis can be found in an earlier report.(Rajan, et al., 2007).

5.2.3.10 Span Between the Yarns, s

The distance between yarns, s, is specified as 0.058824 in. This distance is calculated by considering the geometry of the undeformed fabric. Kevlar® 49 fabric consists of 17 yarns per inch (1/17 = 0.058824”).

5.2.3.11 Real Yarn Thickness, T

The actual thickness of the Kevlar® fabric was measured at 0.011 inches (Simmons, et al., 2004).

5.2.3.12 Effective Yarn Thickness, H

The effective yarn thickness of the material is specified at a value of 6.10E-3 inches. This value is defined in the material card description document as the quotient of the areal density (measured experimentally at 0.144 g/in^2) and the mass density (1.44 g/cm^3(23.5974 g/in^3)).

5.2.3.13 Yarn Cross Sectional Area, S

The cross sectional area of Kevlar® yarn was found to be 1.70E-4 in^2. This value was determined experimentally by measuring the mass of samples of Kevlar® yarn and dividing the mass of the yarn, P, by the product of the mass density (1.44 g/cm^3) multiplied by the length of the specimen, L (see Equation 14, below).

$$S = P/(\rho) \tag{14}$$

$$\begin{aligned} &m_{ave} = 0.03825g \\ &\rho L_{ave} = 34.584g/cm^2 \\ &S = \frac{0.03825}{(34.584)} = 0.00110cm^2 \\ &0.00110cm^2\left(\frac{1in}{2.54cm}\right)^2 = 1.70E-4in^2 \end{aligned}$$

5.2.3.14 Elastic Constant of Element 'a' (linear spring k), EKA

The value specified for the linear spring elastic constant K_1 of the phenomenological material model is 11.75 Msi. An analysis was performed to fit the response curve generated by the M234 governing equations evaluated at a typical strain rate experienced by model elements located near the point of impact of the projectile. The UMAT V1.3 utilized a Cowper-Symonds (CS) model to develop the elastic loading region of the stress-strain response curve. The CS model equation is provided below.

$$E_{adj} = E_{11}\left(1+\frac{\dot{\varepsilon}}{C_E}\right)^{\frac{1}{P_E}} \tag{15}$$

where E_{adj} is the adjusted Young's Modulus for the current time step, E_{11} is the unadjusted Young's Modulus of the material (8.397 Msi), $\dot{\varepsilon}$ is the strain rate of the element at the current time step, C_E is an adjustment factor (set at 0.005), and P_E is an adjustment factor (set at 40).

Utilizing Equation (20), the resulting moduli, E_{adj}, can be determined for a range of strain rate values (see Table 21).

Table 21. Adjusted Modulus of Elasticity by Strain Rate (Cowper Symonds Model, ASU)

Strain Rate (1/ms)	Eadj (Msi)
0.0001	5.0501
0.001	5.3435
1	6.3500
2	6.4610
10	6.7262
20	6.8438

A routine was developed to generate xy data pairs corresponding to the response dictated by the governing equations for M234. These equations are based on a three (3) element phenomenological material model consisting of a modified Maxwell element (without the dashpot) in series with a Kelvin-Voight element. The 3 element model is shown below in Figure 66 and the corresponding governing equation is provided as Equation (16).

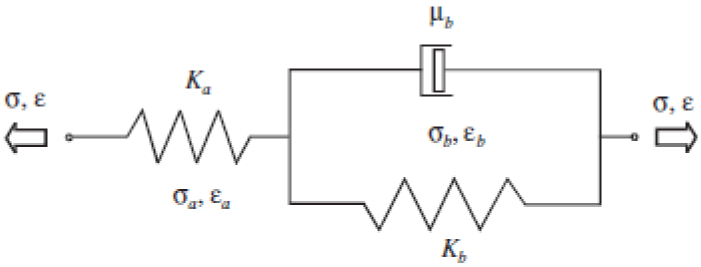

Figure 66. 3-Element Phenomenological Model MAT234

$$\Delta\sigma^{(n)} = \frac{2[K_a K_b \varepsilon^{(n)} - (K_a + K_b)\sigma^{(n)}] + K_a(K_b + 2(\mu_b/\Delta t^{(n)}))\Delta\varepsilon^{(n)}}{(K_a + K_b) + 2(\mu_b/\Delta t^{(n)})} \qquad (16)$$

Figure 67. Phenomenological Material Model with Governing Equation

By selecting a strain increment (0.001) and strain rate (varies), the values for Ka and Mub were selected such that the resulting curve closely resembles the curve generated from the Cowper Symonds model implemented in the UMAT48. The resulting values shown below in Table 22 are the most optimal values for Ka and Mub at each respective value for strain rate.

Table 22. Optimal Values for Ka and Mub for Various Strain Rates

Strain Rate (/s)	Ka (psi)	Mub (opt)
0.1	1.00E+07	1250
1	1.08E+07	1500
1000	11.75E+06	3000
2000	11.75E+06	3250
10000	11.75E+06	3250
20000	12.00E+06	3250

Four models from the FAA NASA ballistic tests were analyzed to determine an appropriate value for the representative strain rate in the impact area of the projectile for modeling purposes. Two (2) high projectile velocity models (LG404 and LG427) were selected with varying number of fabric layers. Similarly two (2) low projectile velocity models (LG966 and LG967) with varying number of fabric layers were selected. For each model, the strain rates of elements located at the approximate point of impact of the projectile were plotted vs. time and analyzed to determine an appropriate value for the strain rate in both the x and y directions. Plots showing the element strain rates with respect to time are provided below in Figures 68 thru 71.

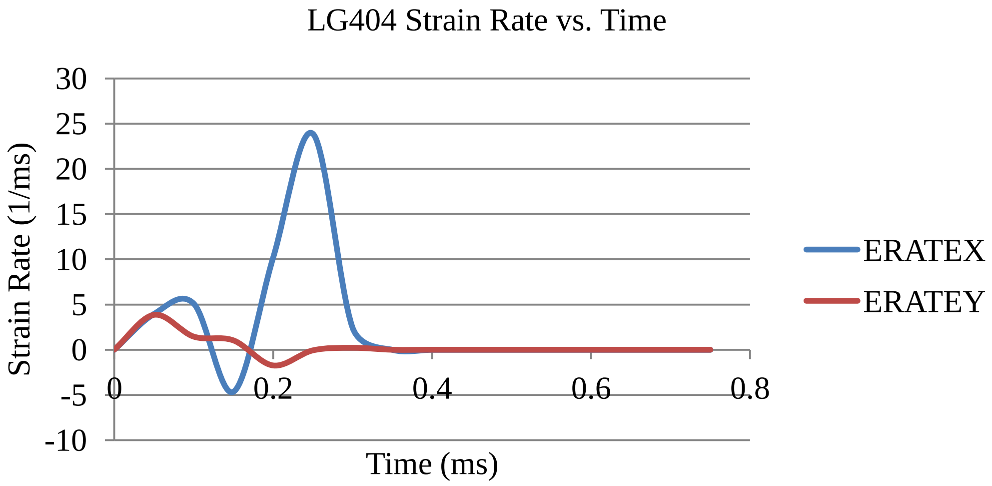

Figure 68. LG404 X and Y Strain Rates vs. Time Near Point of Projectile Impact

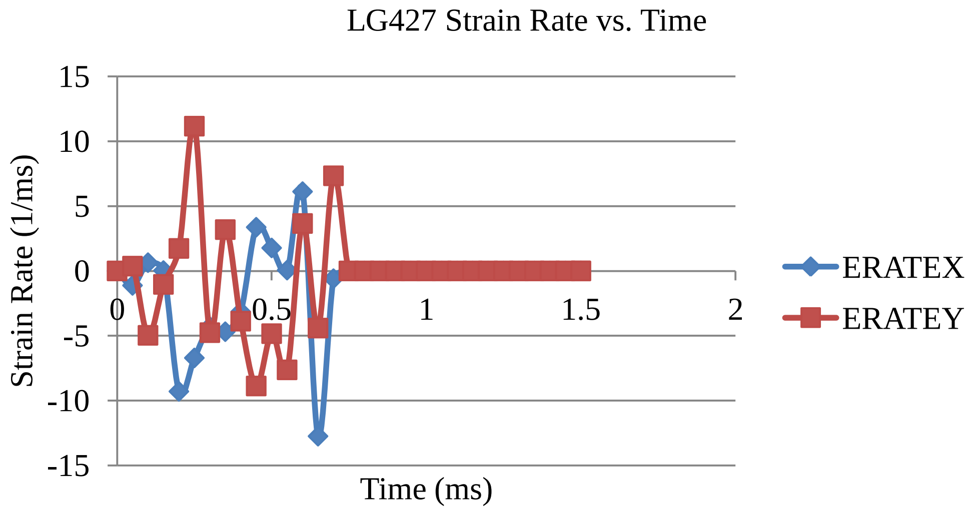

Figure 69. LG427 X and Y Strain Rates vs. Time Near Point of Projectile Impact

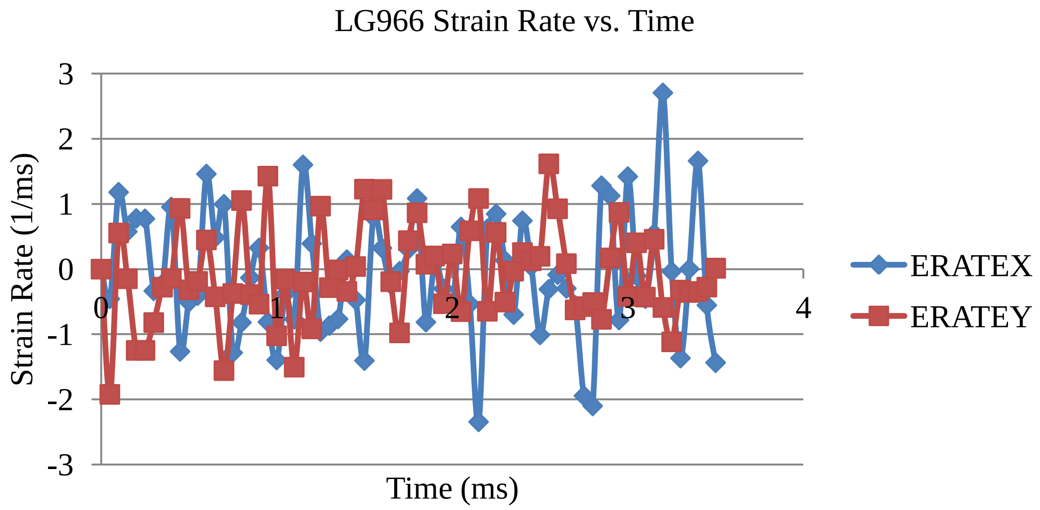

Figure 70. LG966 X and Y Strain Rates vs. Time Near Point of Projectile Impact

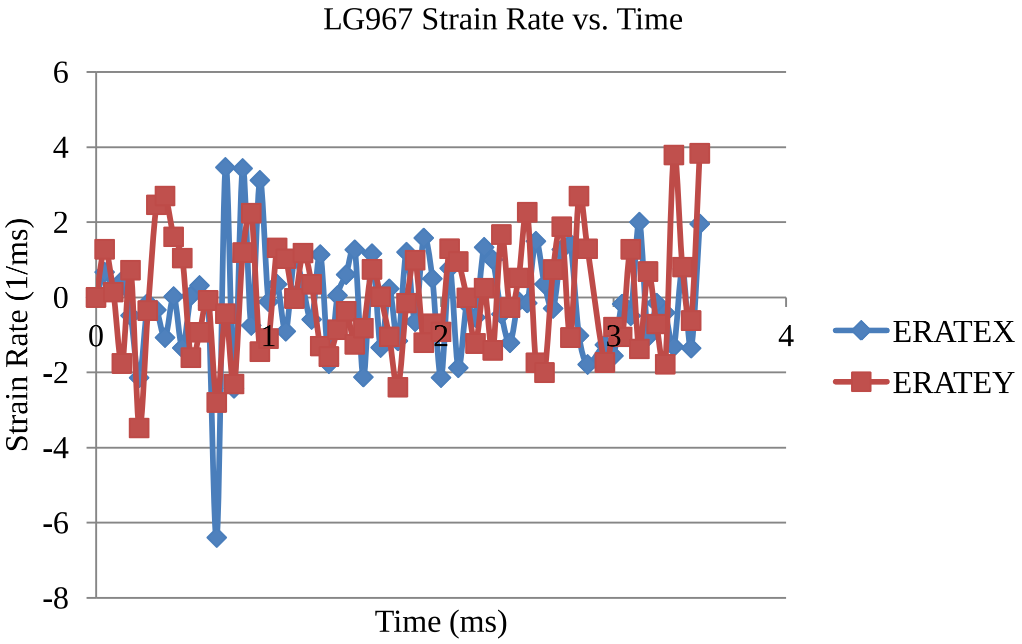

Figure 71. LG967 X and Y Strain Rates vs. Time Near Point of Projectile Impact

Due to the nature of the response curves in the linear elastic loading regions and the variation of strain rate experienced in the FE models, the values for Ka and Mub that most appropriately fit the ASU response curves are Ka=11.75E6 psi and Mub=3250 psi. Figure 72 below presents plot comparisons between the Cowper-Symonds model utilized by ASU UMAT and the response curves generated by the MAT 234 governing equations utilizing these optimized values for Ka and Mub.

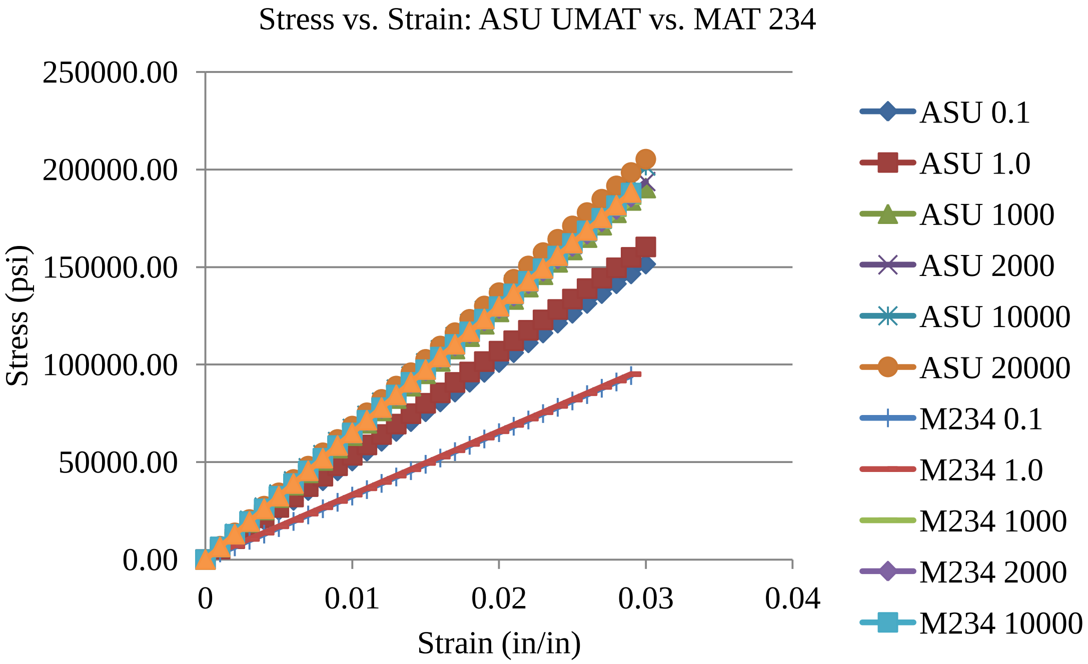

Figure 72. MAT 234 Response Curves with Optimized Parameters vs. ASU

5.2.3.15 Ultimate Strain of Element 'a', EUA

The ultimate strain of Element 'a' (spring element) of the phenomenological material model is specified at 0.0216 (2.16%). This value was determined by considering the maximum stress in a single yarn of Kevlar® under static tensile loading (as determined by experimental testing at ASU, (Rajan, et al., 2007)), found to be 0.254 Msi for a gauge length of 8". Using this value along with the stiffness value of 11.75 Msi for the Maxwell spring element the value for max strain of the Maxwell spring element was determined as the max stress divided by Ka.

$$\sigma_{\max} = 0.254 Msi$$
$$Ka = 11.75 Msi$$
$$EUA = 0.254 / 11.75 = 0.0216$$

5.2.3.16 Damping Coefficient of Element ‘b’, VMB

The value specified for VMB is 3.25 E-3 Msi. This value was determined via a curve fitting procedure and provides the best fit response curve when compared against the same curve generated by the ASU UMAT V1.3 (elastic loading section only).

5.2.3.17 Coefficient of Friction Between Fibers, C

The coefficient of friction between the fabric yarns is specified at 0.2. This corresponds to the values measured during fabric to fabric friction testing performed at ASU (Rajan, et al. 2009).

5.2.3.18 Transverse Shear Modulus, G23

Experimental data for the transverse shear modulus of individual Kevlar®49 yarns are not available. Hence, as a reasonable approximation, the transverse shear modulus is taken as 2.38 Msi, equal to the longitudinal shear modulus.

5.2.3.19 Elastic Constant of Element ‘b’, EKB

The elastic constant of Element ‘b’ of the phenomenological is calculated via Equation 17 below:

$$K_b = \frac{K_a E_1}{K_a - E_1} \tag{17}$$

where K_a = Elastic constant of Element ‘a’, EKA and E_1 is the longitudinal shear modulus, E1. Utilizing the corresponding values for EKA and E1, EKB is found to be 29.43 Msi.

$$EKA = 8.397 Msi$$
$$Ka = 11.75 Msi$$
$$K_b = \left(\frac{11.75 * 8.397}{11.75 - 8.397} \right) = 29.43 Msi$$

5.2.4 Parameter Value Study

To verify that the preliminary values determined in Section 5.2.3 were appropriate for Kevlar® 49 fabric, the material definition was implemented in finite element simulations of quasi-static tension testing that had previously been performed at ASU. The stress strain response of the numerical simulation was compared against the actual response of the fabric during testing. Based on the results from this comparison, some preliminary parameter values were adjusted to fit the MAT234 stress-strain response curves to the experimental test results. The representative response curve from the mechanical tension testing is presented below in Figure 73.

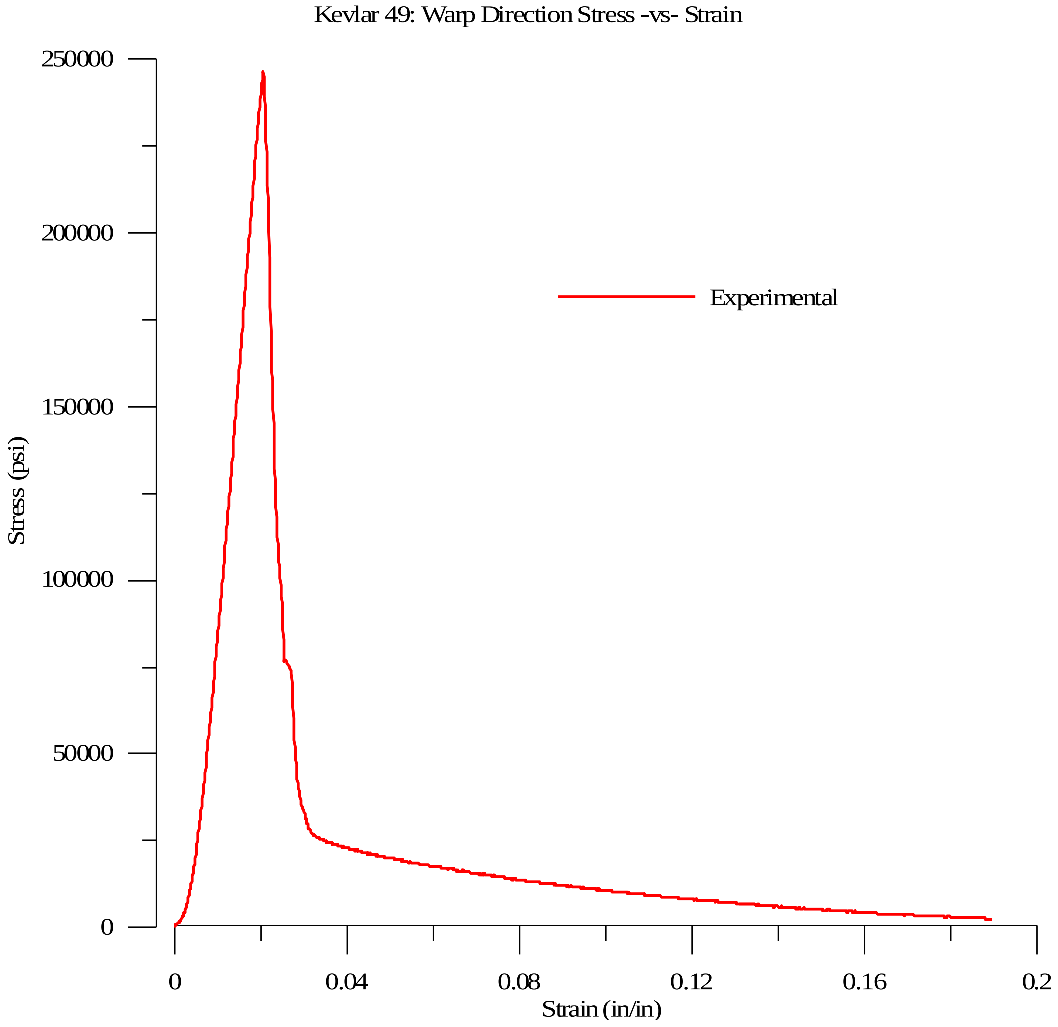

Figure 73. Experimental Response Curve: Kevlar® 49

A numerical simulation of the static tension test utilizing MAT234 was performed and the resulting stress strain plot from an element located in the center of the model fabric was compared against the experimental response curve. The comparison of the response curves is shown below in Figure 74.

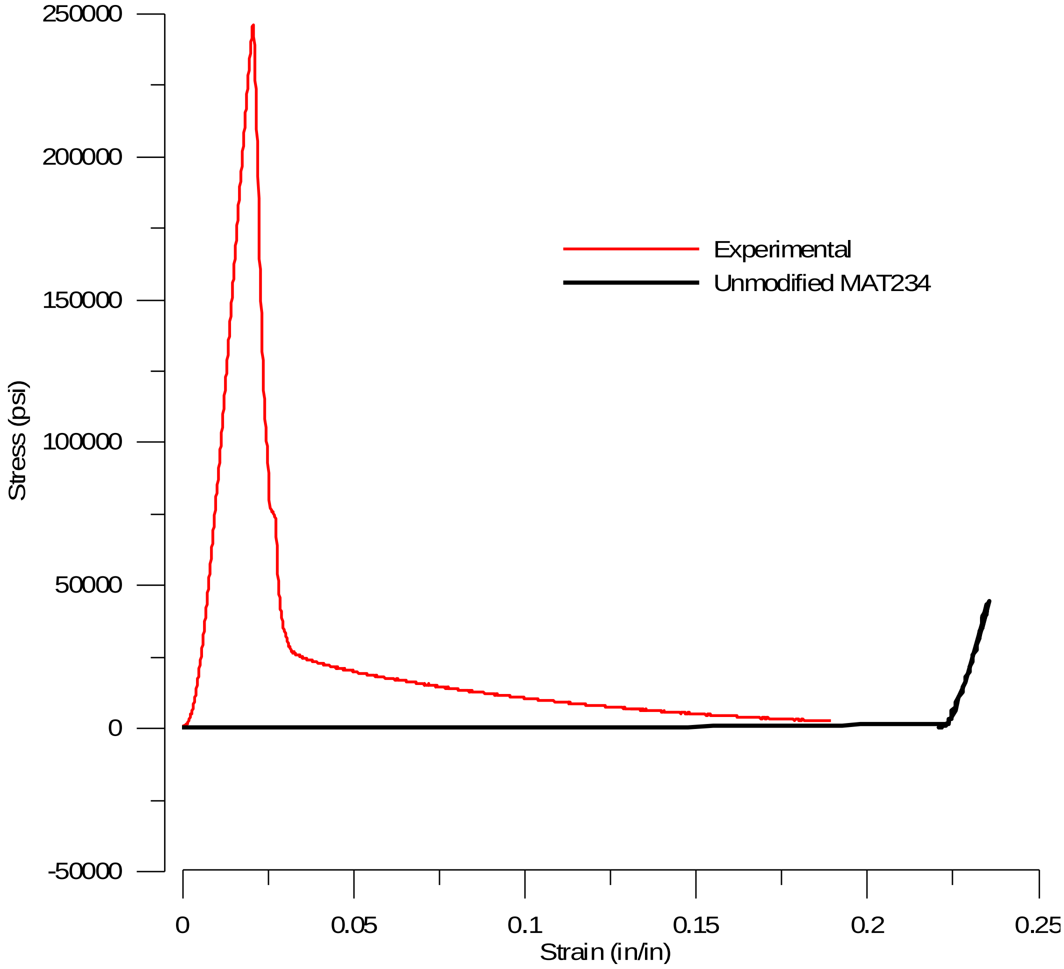

Figure 74. Stress Strain response comparison: Unmod MAT234 vs. Experimental

Some interesting behaviors were observed when utilizing the parameter values indicated above in the MAT234 material model for the tension test model. The response of the Kevlar® fabric was extremely elastic, with the elements undergoing large amounts of shear deformation before beginning to take any load. This delayed response created an overly long uncrimping region, with the strain at which point the fabric begins to load located at approximately 22%. The peak stress attained at this element was far less than the peak stress realized during mechanical testing. Also, the response of the MAT234 model indicated the lack of a distinct post-peak region. To better approximate the behavior of Kevlar® 49 fabric as observed during mechanical testing, the modeling parameters were analyzed to determine their effect on the preliminary deformation of the model fabric. It was estimated that the geometric parameters would play a larger role in the trellising behavior, so these values were the main point of focus. Results showed that the initial region of high deformation and low stress was dictated by the definition of the locking angle (THL) and the transition angle (TA) of the Kevlar® fabric. These values were adjusted until the resulting plot more closely aligned with the response curve from the UMAT48. The resulting values for these parameters were found to be THL = 0.1 and TA = 0.1. The resulting plot from the tension test model utilizing the modified locking angle parameters is provided below in Figure 75.

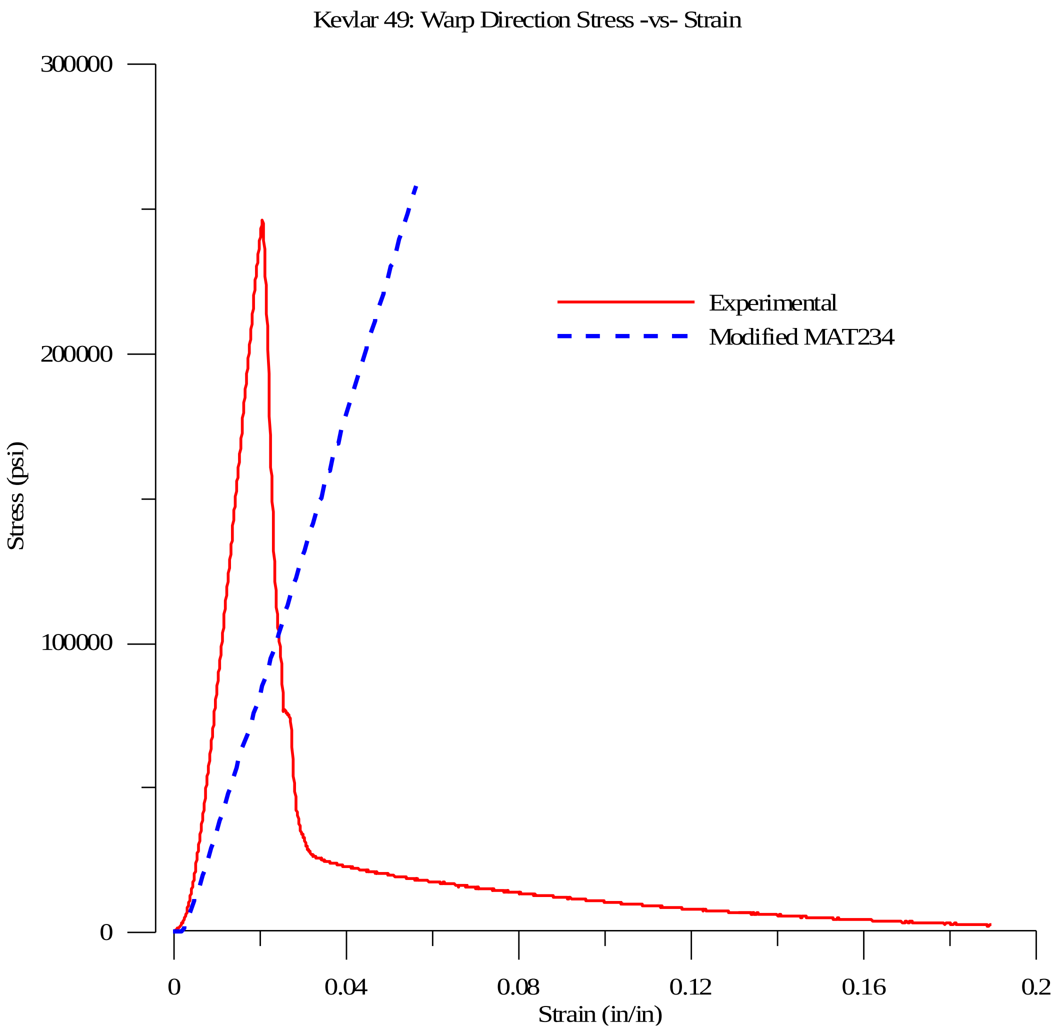

Figure 75. Stress Strain Response: Modified MAT234 vs. Experimental

By adjusting the yarn locking properties, the strain at which the fabric specimen began to take load was shifted to more accurately reflect the experimental results. The stiffness of the model fabric is slightly softer than the experimental modulus, however the difference in the strain rates between the ballistic tests and the static tension tests could account for this discrepancy. The peak stress obtained by the FE model (258,000 psi) was only slightly higher than the experimentally obtained value of 250,000 psi.

6 NUMERICAL RESULTS

6.1 Boundary Condition Study

6.1.1 Quality of FE Simulations: Energy Balance Check

It is necessary to determine the quality of the numerical solutions in order to estimate the accuracy of the finite element simulations. To effectively characterize the possible sources of errors inherent in the FE models associated with this boundary condition study, multiple quantities associated with the overall energy balance of the models were analyzed. These include the hourglass energy ratio (HGR), sliding energy ratio (SER), kinetic energy ratio (KER) and the internal energy ratio (ER) of the simulation. These values are calculated using Equations (18) through (21) below.

$$HGR = \frac{E_{HOURGLASS}}{E_{TOTAL}} \tag{18}$$

$$SER = \frac{E_{SLIDING}}{E_{TOTAL}} \tag{19}$$

$$KER = \frac{E_{KINETIC}}{E_{TOTAL}} \tag{20}$$

$$ER = \frac{E_{INTERNAL}}{E_{TOTAL}} \tag{21}$$

where $E_{HOURGLASS}$ is the hourglass energy at a particular time step, $E_{SLIDING}$ is the sliding interaction energy of the model at a particular time step, $E_{KINETIC}$ is the system kinetic energy at each time step, $E_{INTERNAL}$ is the internal energy of the system at each time step and E_{TOTAL} is the sum of the internal and kinetic energies at each time step.

The threshold values for each of these quantities are presented in Table 23.

Results from QA/QC checks for all eight (8) model suites are presented here in Tables 24 thru 31.

Table 23: Energy Balance Component Threshold Values

	Threshold Value Range
Hourglass Energy Ratio (HG)	HG < 0.1
Sliding Energy Ratio (SE)	SE < 0.1
Kinetic Energy Ratio (KE)	KE < 1.0
Internal Energy Ratio (IE)	IE < 1.0

Table 24. QA/QC Results: CMS Fixed Braced Models

Test Case	Sliding Energy Ratio	Kinetic Energy Ratio	Internal Energy Ratio	Hourglass Energy Ratio
LG963	0.10	1.00	0.65	0.09
LG404	0.00	1.00	0.02	0.00
LG409	0.01	1.00	0.03	0.01
LG424	0.01	1.00	0.04	0.01
LG594	0.22	1.00	0.38	0.01
LG609	0.00	1.00	0.03	0.00
LG610	0.01	1.00	0.05	0.00
LG611	0.01	1.00	0.05	0.00
LG612	0.01	1.00	0.04	0.02
LG618	0.17	1.00	0.30	0.05
LG620	0.12	1.00	0.21	0.02
LG689	0.05	1.00	0.13	0.00
LG692	0.10	1.00	0.24	0.04
LG966	0.29	1.00	0.57	0.00
LG429	0.00	1.00	0.07	0.00
LG432	0.00	1.00	0.09	0.00
LG965	0.40	1.00	0.46	0.03
LG964	0.26	1.00	0.51	0.09
LG411	0.16	1.00	0.26	0.03
LG427	0.04	1.00	0.15	0.01
LG967	0.40	1.00	0.45	0.09
LG971	0.43	1.00	0.44	0.10
LG656	0.27	1.00	0.35	0.02
LG657	0.46	1.00	0.48	0.02
LG969	0.35	1.00	0.45	0.01
LG970	0.40	1.00	0.32	0.11

Table 25. QA/QC Results: CMS Fixed Unbraced Models

Test Case	Sliding Energy Ratio	Kinetic Energy Ratio	Internal Energy Ratio	Hourglass Energy Ratio
LG963	0.10	1.00	0.65	0.17
LG404	0.01	1.00	0.04	0.00
LG409	0.01	1.00	0.03	0.00
LG424	0.01	1.00	0.04	0.00
LG594	0.24	1.00	0.44	0.04
LG609	0.00	1.00	0.03	0.00
LG610	0.01	1.00	0.04	0.00
LG611	0.01	1.00	0.05	0.00
LG612	0.01	1.00	0.05	0.20
LG618	0.12	1.00	0.26	0.04
LG620	0.14	1.00	0.29	0.02
LG689	0.05	1.00	0.13	0.01
LG692	0.14	1.00	0.31	0.05
LG966	0.19	1.00	0.60	0.01
LG429	0.00	1.00	0.07	0.00
LG432	0.00	1.00	0.10	0.00
LG965	0.40	1.00	0.45	0.07
LG964	0.25	1.00	0.50	0.06
LG411	0.20	1.00	0.26	0.02
LG427	0.04	1.00	0.15	0.03
LG967	0.41	1.00	0.50	0.06
LG971	0.42	1.00	0.44	0.07
LG656	0.22	1.00	0.24	0.01
LG657	0.40	1.00	0.39	0.03
LG969	0.33	1.00	0.33	0.11
LG970	0.51	1.00	0.40	0.14

Table 26. QA/QC Results: CMS Free Braced Models

Test Case	Sliding Energy Ratio	Kinetic Energy Ratio	Internal Energy Ratio	Hourglass Energy Ratio
LG963	0.10	1.00	0.64	0.09
LG404	0.00	1.00	0.03	0.00
LG409	0.01	1.00	0.03	0.00
LG424	0.01	1.00	0.04	0.01
LG594	0.17	1.00	0.37	0.04
LG609	0.00	1.00	0.03	0.01
LG610	0.01	1.00	0.05	0.00
LG611	0.02	1.00	0.07	0.00
LG612	0.01	1.00	0.05	0.02
LG618	0.19	1.00	0.34	0.04
LG620	0.17	1.00	0.36	0.02
LG689	0.06	1.00	0.14	0.01
LG692	0.13	1.00	0.30	0.03
LG966	0.29	1.00	0.55	0.00
LG429	0.00	1.00	0.07	0.00
LG432	0.00	1.00	0.09	0.00
LG965	0.40	1.00	0.44	0.05
LG964	0.25	1.00	0.50	0.05
LG411	0.14	1.00	0.23	0.02
LG427	0.04	1.00	0.15	0.02
LG967	0.42	1.00	0.47	0.05
LG971	0.44	1.00	0.43	0.07
LG656	0.21	1.00	0.24	0.01
LG657	0.43	1.00	0.38	0.03
LG969	0.34	1.00	0.33	0.11
LG970	0.50	1.00	0.38	0.11

Table 27. QA/QC Results: CMS Free Unbraced Models

Test Case	Sliding Energy Ratio	Kinetic Energy Ratio	Internal Energy Ratio	Hourglass Energy Ratio
LG963	0.10	1.00	0.64	0.13
LG404	0.01	1.00	0.04	0.00
LG409	0.01	1.00	0.03	0.00
LG424	0.01	1.00	0.05	0.01
LG594	0.24	1.00	0.44	0.04
LG609	0.00	1.00	0.03	0.00
LG610	0.01	1.00	0.04	0.00
LG611	0.01	1.00	0.06	0.00
LG612	0.01	1.00	0.05	0.01
LG618	0.11	1.00	0.23	0.03
LG620	0.16	1.00	0.32	0.02
LG689	0.05	1.00	0.13	0.00
LG692	0.08	1.00	0.21	0.03
LG966	0.26	1.00	0.59	0.01
LG429	0.00	1.00	0.07	0.00
LG432	0.00	1.00	0.09	0.00
LG965	0.40	1.00	0.44	0.05
LG964	0.25	1.00	0.50	0.06
LG411	0.15	1.00	0.26	0.02
LG427	0.03	1.00	0.15	0.02
LG967	0.40	1.00	0.44	0.06
LG971	0.42	1.00	0.42	0.07
LG656	0.20	1.00	0.21	0.01
LG657	0.43	1.00	0.37	0.03
LG969	0.33	1.00	0.34	0.10
LG970	0.50	1.00	0.39	0.10

QA/QC Results: SMS Fixed Braced Models

Table 28. QA/QC Results: SMS Fixed Braced Models

Test Case	Sliding Energy Ratio	Kinetic Energy Ratio	Internal Energy Ratio	Hourglass Energy Ratio
LG963	0.12	1.00	0.50	0.11
LG404	0.01	1.00	0.04	0.00
LG409	0.01	1.00	0.05	0.00
LG424	0.01	1.00	0.07	0.00
LG594	0.17	1.00	0.38	0.04
LG609	0.01	1.00	0.04	0.00
LG610	0.01	1.00	0.04	0.01
LG611	0.00	1.00	0.89	0.00
LG612	0.00	1.00	0.02	0.01
LG618	0.06	1.00	0.25	0.05
LG620	0.06	1.00	0.18	0.02
LG689	0.05	1.00	0.11	0.01
LG692	0.02	1.00	0.10	0.04
LG966	0.01	1.00	0.73	0.00
LG429	0.03	1.00	0.09	0.00
LG432	0.02	1.00	0.08	0.00
LG965	0.10	1.00	0.60	0.02
LG964	0.14	1.00	0.56	0.04
LG411	0.07	1.00	0.15	0.03
LG427	0.05	1.00	0.13	0.03
LG967	0.13	1.00	0.59	0.03
LG971	0.07	1.00	0.62	0.01
LG656	0.13	1.00	0.18	0.01
LG657	0.26	1.00	0.35	0.01
LG969	0.27	1.00	0.42	0.11
LG970	0.20	1.00	0.52	0.06

Table 29. QA/QC Results: SMS Fixed Unbraced Models

Test Case	Sliding Energy Ratio	Kinetic Energy Ratio	Internal Energy Ratio	Hourglass Energy Ratio
LG963	0.14	1.00	0.57	0.10
LG404	0.01	1.00	0.04	0.00
LG409	0.01	1.00	0.05	0.01
LG424	0.01	1.00	0.05	0.00
LG594	0.19	1.00	0.40	0.03
LG609	0.00	1.00	0.03	0.00
LG610	0.01	1.00	0.03	0.00
LG611	0.00	1.00	0.89	0.00
LG612	0.00	1.00	0.02	0.02
LG618	0.03	1.00	0.19	0.04
LG620	0.05	1.00	0.19	0.02
LG689	0.02	1.00	0.07	0.02
LG692	0.03	1.00	0.13	0.03
LG966	0.01	1.00	0.72	0.00
LG429	0.02	1.00	0.09	0.00
LG432	0.02	1.00	0.10	0.00
LG965	0.12	1.00	0.59	0.05
LG964	0.14	1.00	0.55	0.04
LG411	0.21	1.00	0.45	0.01
LG427	0.06	1.00	0.15	0.03
LG967	0.12	1.00	0.58	0.04
LG971	0.05	1.00	0.61	0.04
LG656	0.17	1.00	0.22	0.01
LG657	0.27	1.00	0.34	0.01
LG969	0.29	1.00	0.44	0.09
LG970	0.20	1.00	0.53	0.07

Table 30. QA/QC Results: SMS Free Braced Models

Test Case	Sliding Energy Ratio	Kinetic Energy Ratio	Internal Energy Ratio	Hourglass Energy Ratio
LG963	0.11	1.00	0.48	0.10
LG404	0.01	1.00	0.06	0.00
LG409	0.01	1.00	0.05	0.00
LG424	0.01	1.00	0.07	0.00
LG594	0.09	1.00	0.35	0.03
LG609	0.01	1.00	0.04	0.00
LG610	0.01	1.00	0.03	0.01
LG611	0.00	1.00	0.89	0.00
LG612	0.00	1.00	0.03	0.01
LG618	0.09	1.00	0.31	0.04
LG620	0.06	1.00	0.23	0.02
LG689	0.04	1.00	0.09	0.01
LG692	0.02	1.00	0.11	0.03
LG966	0.01	1.00	0.73	0.00
LG429	0.03	1.00	0.08	0.00
LG432	0.03	1.00	0.08	0.00
LG965	0.11	1.00	0.61	0.05
LG964	0.14	1.00	0.56	0.03
LG411	0.05	1.00	0.13	0.03
LG427	0.05	1.00	0.13	0.02
LG967	0.14	1.00	0.57	0.03
LG971	0.08	1.00	0.60	0.03
LG656	0.13	1.00	0.17	0.01
LG657	0.26	1.00	0.34	0.01
LG969	0.27	1.00	0.41	0.11
LG970	0.20	1.00	0.50	0.07

Table 31. QA/QC Results: SMS Free Unbraced Models

Test Case	Sliding Energy Ratio	Kinetic Energy Ratio	Internal Energy Ratio	Hourglass Energy Ratio
LG963	0.14	1.00	0.55	0.11
LG404	0.01	1.00	0.06	0.00
LG409	0.01	1.00	0.05	0.00
LG424	0.02	1.00	0.08	0.00
LG594	0.06	1.00	0.32	0.04
LG609	0.01	1.00	0.04	0.00
LG610	0.01	1.00	0.03	0.01
LG611	0.00	1.00	0.89	0.00
LG612	0.00	1.00	0.03	0.01
LG618	0.05	1.00	0.21	0.05
LG620	0.05	1.00	0.17	0.02
LG689	0.03	1.00	0.09	0.01
LG692	0.02	1.00	0.10	0.04
LG966	0.02	1.00	0.73	0.00
LG429	0.03	1.00	0.08	0.00
LG432	0.03	1.00	0.09	0.00
LG965	0.10	1.00	0.59	0.02
LG964	0.14	1.00	0.54	0.04
LG411	0.06	1.00	0.14	0.03
LG427	0.05	1.00	0.12	0.03
LG967	0.13	1.00	0.57	0.03
LG971	0.07	1.00	0.61	0.01
LG656	0.14	1.00	0.17	0.01
LG657	0.26	1.00	0.34	0.01
LG969	0.28	1.00	0.44	0.11
LG970	0.19	1.00	0.50	0.06

6.1.1.1 Hourglass Energy Ratio

A summary of the models experiencing hourglass energy ratios higher than the threshold limit of 0.1 is provided here in Table 32.

Table 32. Hourglass Energy Ratio Results Summary

CMS	Models
Fixed Braced	LG970
Fixed Unbraced	LG963, LG612, LG969, LG970
Free Braced	LG969, LG970
Free Unbraced	LG963, LG612
SMS	Models
Fixed Braced	LG963, LG969
Fixed Unbraced	--
Free Braced	LG969
Free Unbraced	LG963, LG969

CMS configured models were observed to have more out of range hourglass energy ratios than SMS configured models, with the SMS Fixed Unbraced modeling scheme providing the best results for hourglassing with all models meeting the HGR acceptance criteria. It is worthy to note that of all models exhibiting out of spec HGR values, only one (1) model, LG612, was associated with the ballistic testing from Phase I or Phase II. All other models were associated with the Phase III ballistic testing (LG9XX). Phase III ballistic testing was performed with reduced initial projectile velocities, with nearly all tests resulting in full projectile containment.

The hourglass energy ratios for the “flat” layers of fabric (layers 15 thru 22 located at the ring opening) of the CMS fixed unbraced model LG970 are shown below. The hourglass energy ratio associated with the inner most layer of fabric (layer 15) is was observed to be consistently higher than that of the other layers. The hourglass energy ratio for the fabric layers consistently increase as the projectile velocity decreases.

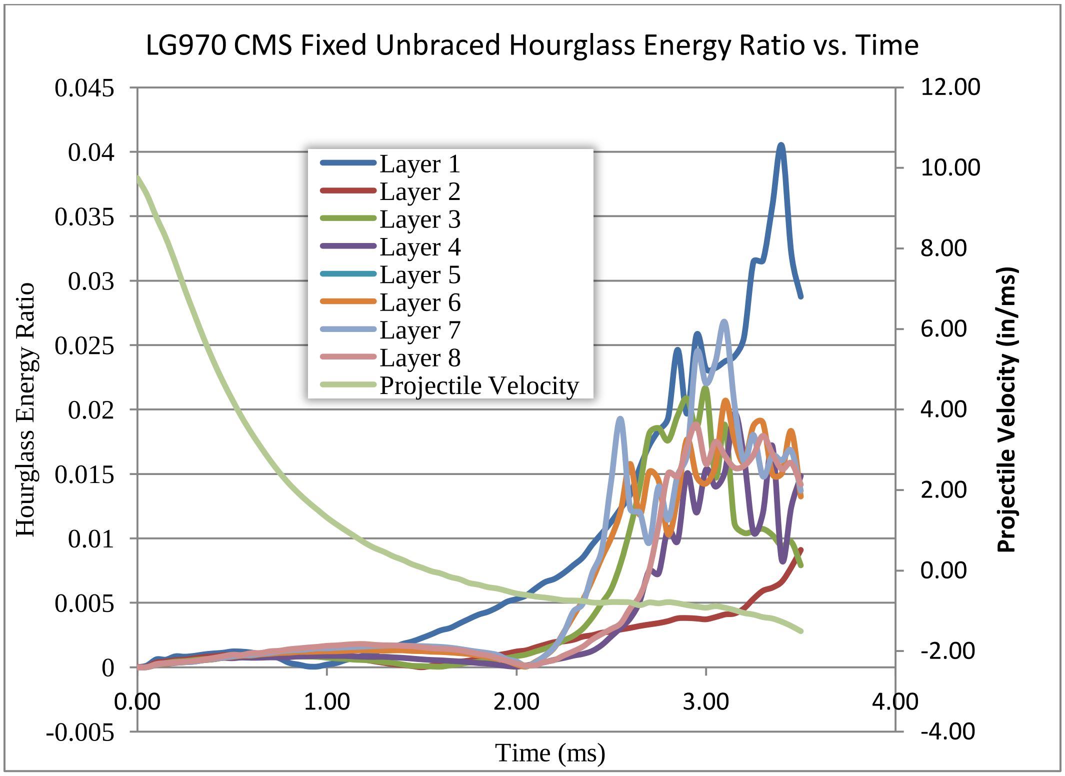

Figure 76. LG967 Hourglass Energy Ratio (Flat Fabric Layers)

The hourglass energy ratio for the test case LG970 (CMS) for all fixity conditions is provided below in Figure 77. The plots represent the hourglass energy ratio associated with the innermost layer of fabric at the opening of the ring (flat portion).

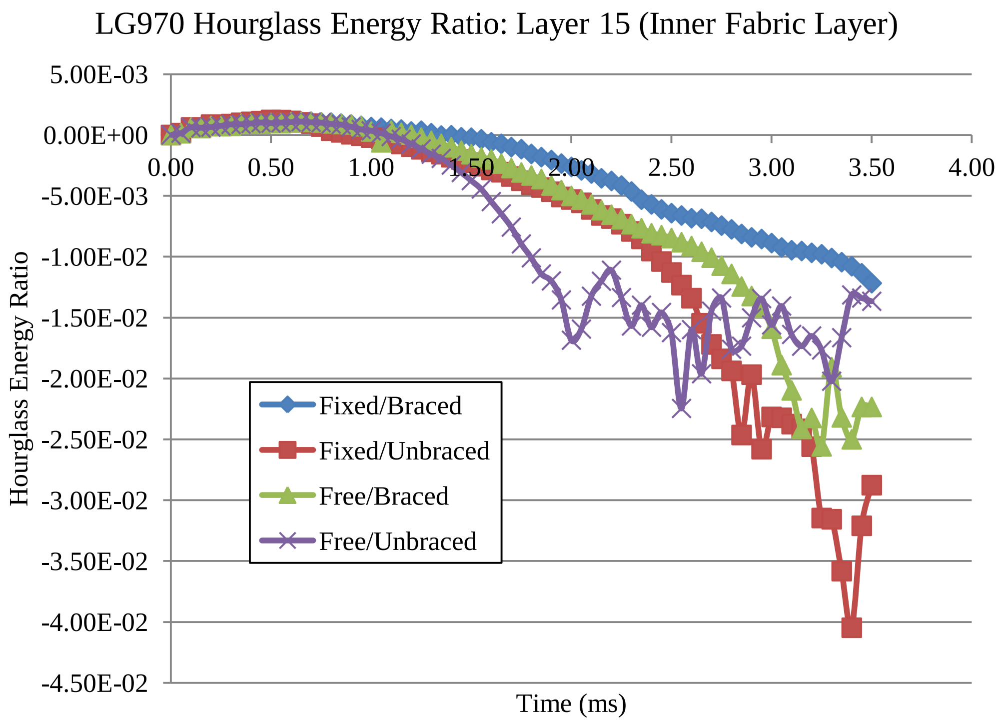

Figure 77. LG70 CMS Hourglass Energy Ratio vs. Time

The hourglass energy ratio remains fairly consistent between the four (4) model configurations until approximately 1.0 ms into the analysis. This initial loading region is characterized by elevated projectile velocities and high initial strain rates.

For comparison, the hourglass energy ratio for the inner-most layer of a high velocity, full penetration model (LG404) is provided below in Figure 78. The projectile velocity (895.7 fps) is much greater than the ballistic limit of the test configuration (8 layers BL = 630 fps) (Vaidya, 2010).

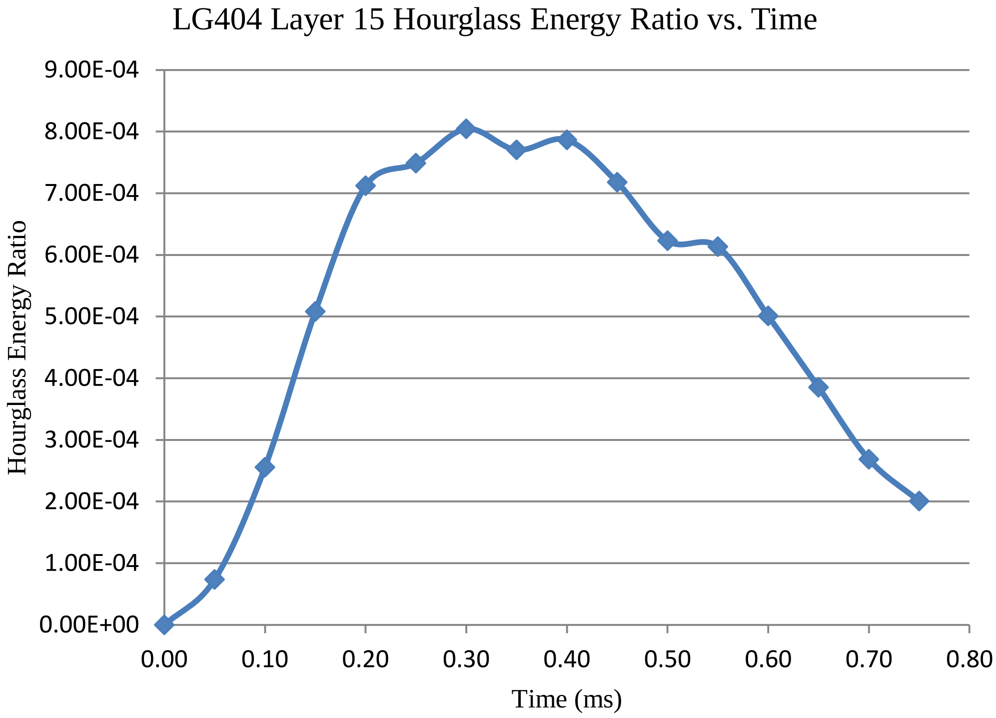

Figure 78. LG404 CMS Fixed Braced Hourglass Energy Ratio vs. Time

The model exhibits minimal hourglassing as the projectile quickly penetrates the fabric layers.

6.1.1.2 Sliding Energy Ratio

Many models were observed to exceed the Sliding Energy Ratio threshold limit of 0.1 (10%) as shown below in Table 33.

Table 33. Models Experiencing SER Exceedance

CMS	Models
Fixed Braced	LG594,LG618,LG620,LG966,LG965,LG964,LG411,LG967,LG971, LG656, LG657,LG969,LG970
Fixed Unbraced	LG594,LG618,LG620,LG692,LG966,LG965,LG964,LG411,LG967, LG971, LG656,LG657,LG969,LG970
Free Braced	LG594,LG618,LG620,LG692,LG966,LG965,LG964,LG411,LG967, LG971, LG656,LG657,LG969,LG970
Free Unbraced	LG594,LG618,LG620,LG966,LG965,LG964,LG411,LG967,LG971, LG656, LG657,LG969,LG970

SMS	Models
Fixed Braced	LG963,LG594,LG964,LG967,LG656,LG657,LG969,LG970
Fixed Unbraced	LG963,LG594,LG965,LG964,LG411,LG967,LG656,LG657,LG969, LG970
Free Braced	LG963,LG965,LG964,LG967,LG656,LG657,LG969,LG970
Free Unbraced	LG963,LG964,LG967,LG656,LG657,LG969,LG970

Table 34. SER Model Details

File Run	Penetrator		Fabric Layers	Actual Configuration			Before Impact
	Type	Mass		Roll	Pitch	Yaw	Velocity
LG963	Old	323.5	4	7.5	5.5	-0.7	308.3
LG594	New	306.8	8	27.0	6.6	47.8	843.9
LG618	New	312.3	8	-47.1	6.3	51.6	866.4
LG692	Old	324.1	8	38.2	2.3	41.5	885.3
LG620	New	316.2	8	-37.8	0.2	55.1	893.8
LG966	Old	323.1	8	7.6	-4.3	5.4	355.0
LG965	Old	323.0	16	6.6	-37.7	-0.9	555.5
LG964	Old	322.5	17	-4.6	19.9	5.9	601.0
LG411	Old	314.8	24	0.0	0.0	0.0	885.8
LG967	Old	323.5	24	55.7	-4.5	-54.5	575.0
LG971	Old	322.9	24	-4.2	6.3	-7.2	564.0
LG656	Old	324.1	32	9.0	-2.3	-10.1	967.3
LG657	Old	324.1	32	-22.2	9.7	1.4	829.7
LG969	Old	323.1	32	2.6	5.4	-0.5	771.0
LG970	Old	322.1	32	2.0	-3.6	-5.0	812.0
		(g)		(deg)	(deg)	(deg)	(ft/sec)

Details about these models are provided in Table 34. Models from all Phases of testing (I, II and III) were observed to violate the SER threshold value. Phase I and Phase II tests (LG4XX, LG5XX and LG6XX) models exhibiting increased levels of sliding interface energy were observed to be characterized by more extreme initial projectile yaw orientations, with the exceptions of LG411, LG656 and LG657. These more highly oriented projectiles increased the amount of fabric to projectile interaction and fabric to fabric interaction as some of the "cutting" penetration associated with a non-oriented impact was minimized. However, Phase III ballistic testing (LG9XX models) was run with lower initial projectile velocities than tests performed in conjunction with Phases I and II. It can be noted from Figures 79 and 80 that as the X direction velocity of the projectile decreases, the sliding interface energy ratio increases. This behavior can be attributed to the increased interaction between the fabric layers as the fabric attempts to contain the projectile. The lower initial projectile velocities of the Phase III ballistic tests results in increased sliding energy ratios observed in the numerical simulations.

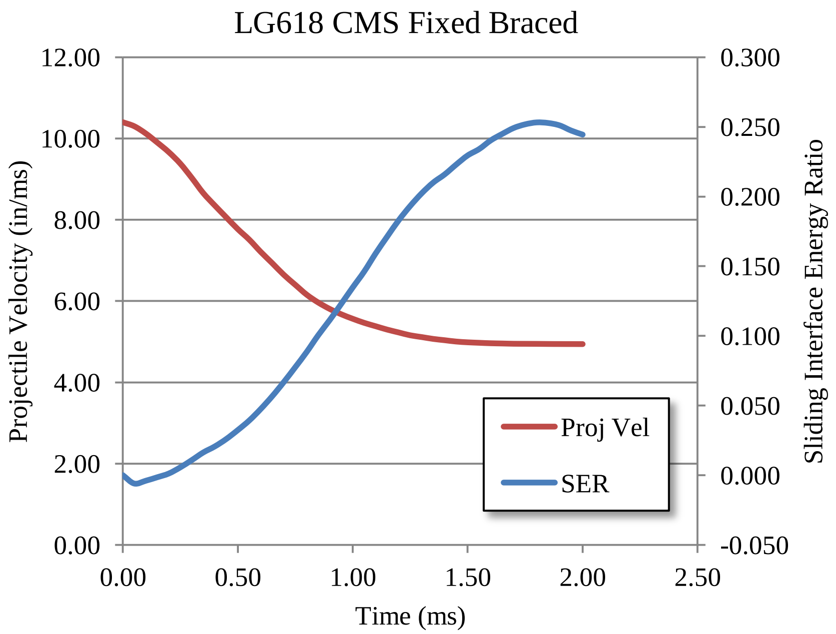

Figure 79. LG618 CMS Fixed Braced Sliding Energy Ratio/Projectile Velocity

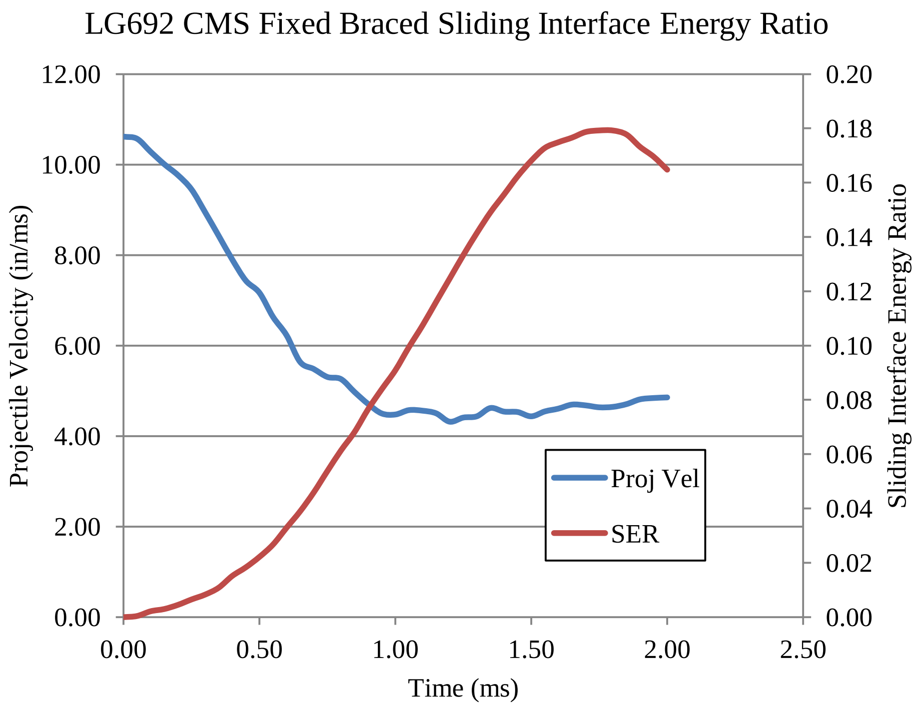

Figure 80. LG692 CMS Fixed Braced Sliding Energy Ratio/Projectile Velocity

The sliding energy ratios with respect to time for model LG970 (all boundary condition configurations) are shown below in Figure 81. The plots show a consistent increase in the sliding energy ratio with respect to time. This general trend was observed to be consistent for all model configurations. The model energy plots violate the threshold value for sliding energy ratio (0.10) at approximately 0.65 ms.

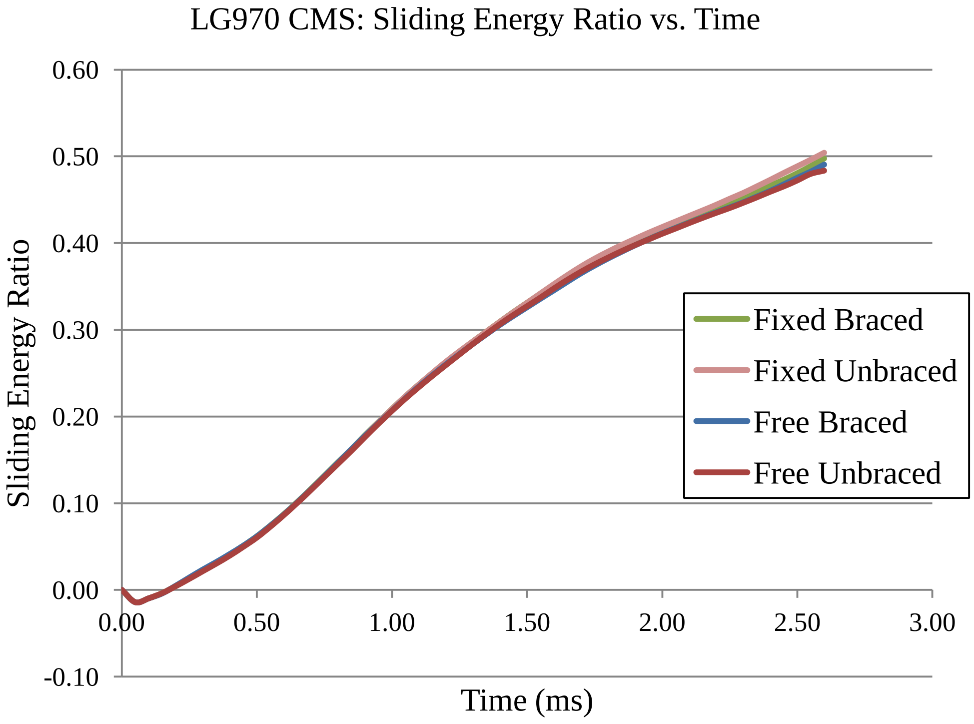

Figure 81. LG970 Sliding Energy Ratio vs. Time

In comparison, the sliding energy ratio trace for a high velocity, low orientation projectile model (LG404) is presented below in Figure 82. The maximum sliding energy ratio for LG404 (0.00) is much lower than that of LG970 (0.40), which is consistent with the sliding energy results from all other model configurations. Simulations of tests with high projectile velocities were generally not observed to experience issues with elevated sliding energy levels. Test models with projectile velocities near or below the ballistic limit of the test configuration were observed to experience elevated sliding energy ratios. This is due to the reduced “cutting action” of the projectile and the increased fabric layer interactions when the projectile is nearly contained or fully contained within the fabric.

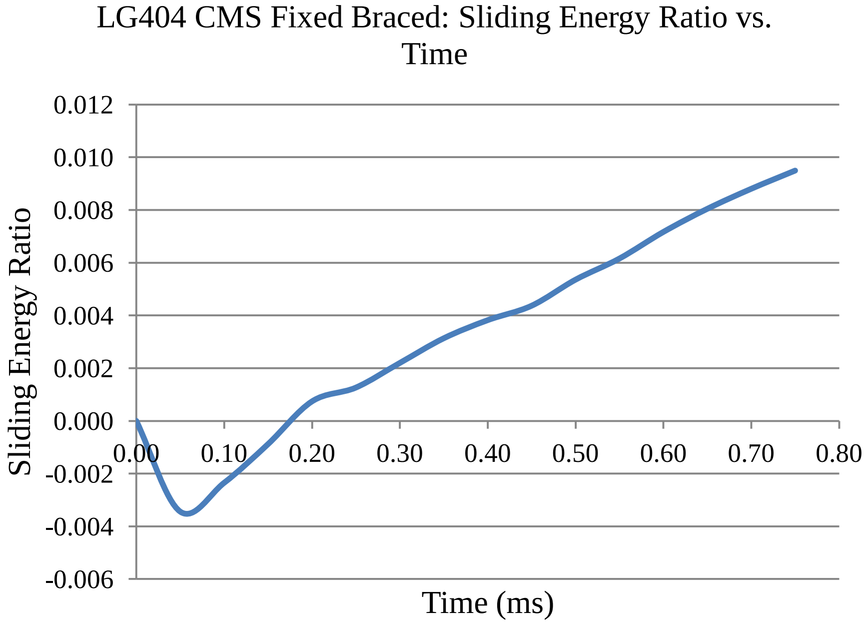

Figure 82. LG404 CMS Fixed Braced Sliding Energy Ratio vs. Time

6.1.1.3 Kinetic Energy Ratio (KER)

No models were observed to experience issues with the Kinetic Energy Ratio.

6.1.1.4 Internal Energy Ratio (IER)

No models were observed to experience issues with the Internal Energy Ratio.

6.1.2 Effect of Bracing

6.1.2.1 CMS/Fixed Models

6.1.2.1.1 Energy Absorption

A comparison of the percent energy absorbed by the fixed CMS models both with and without bracing is provided below in Table 35

Table 35. Fixed CMS Model Energy Results

	% Energy Absorbed			Difference		
Test No.	NASA	Fixed Braced	Fixed Unbraced	NASA-Braced	NASA-Unbraced	Braced-Unbraced
LG963	67.4%	97.2%	99.2%	29.8%	31.8%	-2.0%
LG404	16.1%	11.3%	16.4%	-4.9%	0.3%	-5.2%
LG409	17.6%	14.9%	15.0%	-2.7%	-2.6%	0.0%
LG424	20.1%	17.0%	17.5%	-3.2%	-2.6%	-0.5%
LG594	67.0%	90.3%	94.0%	23.3%	27.0%	-3.7%
LG609	18.4%	14.9%	15.0%	-3.5%	-3.4%	0.0%
LG610	16.9%	21.5%	21.9%	4.6%	5.0%	-0.5%
LG611	22.4%	24.0%	23.4%	1.6%	1.0%	0.6%
LG612	16.1%	20.8%	20.5%	4.7%	4.4%	0.3%
LG618	58.4%	77.4%	72.8%	19.0%	14.4%	4.6%
LG620	57.8%	69.2%	77.2%	11.4%	19.4%	-8.0%
LG689	46.6%	45.2%	48.3%	-1.4%	1.7%	-3.1%
LG692	53.7%	75.6%	76.8%	21.9%	23.2%	-1.2%
LG966	93.4%	99.6%	98.9%	6.1%	5.5%	0.7%
LG429	38.4%	23.4%	23.7%	-15.0%	-14.6%	-0.4%
LG432	47.4%	26.7%	30.5%	-20.7%	-16.9%	-3.7%
LG965	100.0%	93.5%	92.5%	-6.5%	-7.5%	1.0%
LG964	98.1%	90.5%	92.9%	-7.6%	-5.2%	-2.4%
LG411	78.2%	86.0%	88.7%	7.8%	10.5%	-2.6%
LG427	56.0%	51.8%	51.5%	-4.2%	-4.5%	0.3%
LG967	100.0%	95.9%	95.6%	-4.1%	-4.4%	0.4%
LG971	100.0%	97.9%	97.9%	-2.1%	-2.1%	0.1%
LG656	76.5%	95.7%	81.3%	19.2%	4.8%	14.4%
LG657	100.0%	100.0%	99.9%	0.0%	-0.1%	0.1%
LG969	100.0%	99.1%	98.2%	-0.9%	-1.8%	0.9%
LG970	95.9%	98.3%	97.2%	2.4%	1.3%	1.1%
			Mean	2.9%	3.2%	-0.3%
			Median	-0.5%	0.6%	0.0%
			Max Abs	29.8%	31.8%	14.4%
			Min Abs	0.0%	0.1%	0.0%
			Std. Dev.	11.9%	11.8%	3.9%

It is evident from the results presented above that the inclusion of the vertical steel wall braces in the fixed/CMS finite element models had a negligible impact on the numerical results. There was minimal change in both the mean (0.3%) and standard deviation (3.9%) between the two solutions while only two (2) models experienced a change in energy absorption greater than 5%; LG620 and LG656. The projectile orientation and velocity information is presented below in Table 36Table 36.

Table 36. Projectile Orientation and Velocity Information

Model	Roll (deg)	Pitch (deg)	Yaw (deg)	Init. Proj. Vel. (fps)	Ballistic Limit (fps)
LG620	-47.1	6.3	51.6	866	620-640
LG656	9.0	-2.3	-10.1	967	925-950

The extreme yaw angle of the projectile at impact during the test LG620 may have contributed to the deviation of the absorbed energy. Upon inspection, four of the 7 models experiencing the highest differences in the amount of absorbed energy are characterized by projectiles that impact the fabric at extreme yaw angles. This variability makes sense, as at these increased angles more energy can be absorbed via other modes, such as deformation of the projectile or additional contact between the projectile and the fabric layers rather than direct deformation of the fabric. For test LG656, the projectile velocity was near enough to the ballistic limit of the test setup to cause the increased variance in the energy absorption between the braced and unbraced models.

6.1.2.1.2 Displacement

Results from the point of impact displacement analysis for fixed CMS models both with and without bracing are presented below in Table 37.

Table 37. Point of Impact Displacement Values: Fixed CMS Models

	Displacement (in)			
Test No.	NASA	Fixed	Fixed	% Diff:
LG963	2.6	7.1	7.0	2.0%
LG964	3.0	5.4	4.9	10.4%
LG965	3.0	5.6	5.5	0.9%
LG967	2.7	4.1	4.1	0.0%
LG969	3.2	4.4	4.3	2.3%
LG970	3.6	4.6	4.6	-0.6%
LG971	2.5	4.1	4.1	-0.2%
			Mean	2.1%
			Max	10.4%
			Min	-0.6%
			Std Dev	3.8%

Differences between the point of impact displacements associated with the fixed braced CMS models vary only slightly (2.1% mean difference) from those associated with the fixed-unbraced-CMS models indicating a negligible effect on the results of the fixed numerical simulations. Results from both suites of models, however, vary greatly from the displacements measured during ballistic testing.

6.1.2.1.3 Damage

Results from the damage comparison analysis performed on fixed CMS models are provided below in Table 38.

Table 38. Damage Analysis Results: CMS Fixed Models

		NASA		Fixed-Braced		Fixed-Unbraced	
	No. Layers	Pen	Dam	Pen	Dam	Pen	Dam
LG404	8	8	0	8	0	8	0
LG965	16	16	0	0	0	0	0
LG967	24	0	10	0	4	0	0
LG969	32	3	8	0	4	0	4
LG971	24	0	13	0	0	0	0

Damage results for the model LG404 most accurately resembled the damage observed during ballistic testing as all eight (8) layers of fabric were penetrated for both the experimental case and the numerical simulation. The damage incurred by the 900 series (Phase III) models began to deviate from the damage observed during experimental testing. The LG965 model (16 fabric layers) ballistic test resulted in 16 penetrated layers experimentally. However, FE modeling of LG965 resulted in no layers neither damaged nor penetrated for both the braced and unbraced conditions. Similarly, the experimental results for LG967 (32 total fabric layers) included 10 damaged layers while the FE model resulted in zero damaged layers. The test LG969 (24 total layers) resulted in three (3) penetrated layers and eight (8) damaged layers during experimental testing. For all of the Phase III test cases considered above, the FE simulations underpredicted the damage to the Kevlar® fabric.

6.1.2.2 CMS/Free Models

6.1.2.2.1 Energy Absorption

A comparison of the energies absorbed by the free CMS models both with and without bracing is provided below in Table 39

Table 39. Energy Absorption Results: CMS/Free Braced vs. Unbraced Models

	% Energy Absorbed			Difference		
Test No.	NASA	Free Braced	Free Unbraced	NASA - Braced	NASA - Unbraced	Braced-Unbraced
LG963	67.4%	97.5%	98.5%	30.1%	31.1%	-1.0%
LG404	16.1%	12.1%	16.4%	-4.0%	0.2%	-4.3%
LG409	17.6%	14.7%	14.5%	-2.9%	-3.1%	0.2%
LG424	20.1%	18.6%	18.6%	-1.6%	-1.5%	-0.1%
LG594	67.0%	88.6%	97.1%	21.5%	30.0%	-8.5%

LG609	18.4%	14.8%	14.5%	-3.6%	-3.9%	0.3%
LG610	16.9%	22.7%	21.1%	5.8%	4.2%	1.6%
LG611	22.4%	27.4%	25.6%	5.0%	3.2%	1.8%
LG612	16.1%	20.7%	21.7%	4.6%	5.6%	-1.0%
LG618	58.4%	81.4%	71.9%	23.0%	13.5%	9.6%
LG620	57.8%	81.7%	77.2%	24.0%	19.4%	4.6%
LG689	46.6%	52.7%	49.2%	6.1%	2.6%	3.5%
LG692	53.7%	82.1%	70.4%	28.5%	16.7%	11.7%
LG966	93.4%	99.7%	99.1%	6.3%	5.7%	0.6%
LG429	38.4%	23.2%	21.9%	-15.2%	-16.5%	1.3%
LG432	47.4%	27.6%	27.0%	-19.8%	-20.4%	0.7%
LG965	100.0%	94.1%	94.4%	-5.9%	-5.6%	-0.3%
LG964	98.1%	91.7%	92.9%	-6.4%	-5.2%	-1.2%
LG411	78.2%	78.8%	86.4%	0.6%	8.1%	-7.6%
LG427	56.0%	48.9%	53.5%	-7.1%	-2.5%	-4.6%
LG967	100.0%	96.6%	96.7%	-3.4%	-3.3%	-0.1%
LG971	100.0%	98.1%	98.2%	-1.9%	-1.8%	-0.2%
LG656	76.5%	81.9%	69.3%	5.4%	-7.2%	12.6%
LG657	100.0%	100.0%	99.9%	0.0%	-0.1%	0.0%
LG969	100.0%	98.5%	98.7%	-1.5%	-1.3%	-0.2%
LG970	95.9%	98.0%	98.0%	2.1%	2.2%	-0.1%
			Mean	3.4%	2.7%	0.7%
			Median	0.3%	0.1%	0.0%
			Max Abs	30.1%	31.1%	12.6%
			Min Abs	0.0%	0.1%	0.0%
			Std. Dev.	12.6%	11.9%	4.8%

It is evident from these results that the inclusion of the vertical steel wall braces in the free CMS finite element models had a negligible impact on the energy absorption of the numerical results. There was minimal change in both the mean percent energy absorption (0.7%) and standard deviation (4.8%) between the two solutions. Five (5) models experienced changes in percent energy absorption greater than 5%; LG594, LG618, LG692, LG411 and LG656. The projectile orientation and velocity information for these tests is provided below in Table 40.

Table 40. Projectile Orientation and Velocity Information

Model	Roll (deg)	Pitch (deg)	Yaw (deg)	Init. Proj. Vel. (fps)	Ballistic Limit (fps)
LG594	27.0	6.6	47.8	844	620-640
LG618	-47.1	6.3	51.6	866	620-640
LG692	38.2	2.3	41.5	885	620-640
LG411	0.0	0.0	0.0	886	850-875
LG656	9.0	-2.3	-10.1	967	925-950

The extreme yaw angles of tests 594, 618 and 692 led to the variance observed in the percent energy absorbed between the braced and unbraced models. For models LG411 and LG656, the variation in the percent energy absorbed by the braced and unbraced models can mainly be attributed to the proximity of the initial projectile velocities to the ballistic limits of the fabric configurations.

6.1.2.2.2 Displacement

Results from the point of impact displacement analysis for free CMS models both with and without ring bracing are presented below in Table 41.

Table 41. Point of Impact Displacement Values: Free CMS Models

	Displacement (in)			
Test No.	NASA	Free	Free	% Diff:
LG963	2.6	7.0	7.0	0.0%
LG964	3.0	5.4	5.4	0.2%
LG965	3.0	5.5	5.6	-0.9%
LG967	2.7	4.0	4.0	0.5%
LG969	3.2	4.2	4.3	-1.6%
LG970	3.6	4.7	4.7	0.0%
LG971	2.5	4.0	4.1	-2.2%
			Mean	-0.6%
			Max	0.5%
			Min	-2.2%
			Std Dev	1.0%

Differences between the point of impact displacements associated with the free braced CMS models vary only slightly (-0.6% mean difference) from those associated with the free unbraced CMS models indicating a negligible effect on the results of the free numerical simulations. Results from both the braced and unbraced models, however, vary greatly from the displacements experienced during ballistic testing

6.1.2.2.3 Damage

Results from the damage comparison analysis performed on free CMS models are provided below in Table 42.

Table 42. Damage Analysis Results: Free CMS Models

		NASA		Free-Braced		Free-Unbraced	
	No. Layers	Pen	Dam	Pen	Dam	Pen	Dam
LG404	8	8	0	8	0	8	0
LG965	16	16	0	0	0	0	0
LG967	24	0	10	0	0	0	0
LG969	32	3	8	0	4	0	8
LG971	24	0	13	0	0	0	0

Damage results for model LG404 most accurately resembled the damage observed during ballistic testing as all eight (8) layers of fabric were penetrated for both the experimental case and the numerical simulation. The damage incurred by the 900 series (Phase III) models began to deviate from the damage observed during experimental testing. The LG965 model (16 fabric layers) ballistic test resulted in 16 penetrated layers experimentally. However, FE modeling of LG965 resulted in no layers neither damaged nor penetrated for both the braced and unbraced conditions. Similarly, the experimental results for LG967 (32 total fabric layers) included 10 damaged layers while the FE model resulted in zero damaged layers. The test LG969 (24 total layers) resulted in three (3) penetrated layers and eight (8) damaged layers during experimental testing. For all of the Phase III test cases considered above, the FE simulations underpredicted the damage to the Kevlar® fabric.

6.1.2.3 SMS/Fixed Models

6.1.2.3.1 Energy Absorption

A comparison of the energies absorbed by the fixed SMS models both with and without bracing is provided below in Table 43.

Table 43. Energy Absorption Results: SMS/Fixed Braced vs. Unbraced Models

	% Energy Absorbed			Difference		
Test No.	NASA	Fixed Braced	Fixed Unbraced	NASA-Braced	NASA-Unbraced	Braced-Unbraced
LG963	67.4%	97.9%	98.7%	30.5%	31.3%	-0.8%
LG404	16.1%	20.7%	20.6%	4.5%	4.5%	0.0%
LG409	17.6%	20.0%	24.2%	2.4%	6.6%	-4.2%
LG424	20.1%	28.2%	24.5%	8.0%	4.4%	3.6%
LG594	67.0%	92.5%	95.2%	25.5%	28.2%	-2.7%
LG609	18.4%	17.9%	15.0%	-0.5%	-3.4%	3.0%
LG610	16.9%	16.0%	17.1%	-0.9%	0.2%	-1.1%
LG611	22.4%	33.5%	28.1%	11.1%	5.8%	5.4%
LG612	16.1%	14.8%	10.9%	-1.3%	-5.2%	3.9%
LG618	58.4%	72.7%	60.3%	14.3%	1.9%	12.4%
LG620	57.8%	63.5%	60.5%	5.7%	2.7%	3.0%
LG689	46.6%	43.5%	26.6%	-3.0%	-19.9%	16.9%
LG692	53.7%	38.0%	45.6%	-15.7%	-8.1%	-7.6%
LG966	93.4%	100.0%	100.0%	6.6%	6.6%	0.0%
LG429	38.4%	34.6%	36.5%	-3.8%	-1.9%	-1.9%
LG432	47.4%	33.8%	41.9%	-13.6%	-5.5%	-8.1%
LG965	100.0%	96.1%	96.3%	-3.9%	-3.7%	-0.2%
LG964	98.1%	96.3%	96.9%	-1.8%	-1.2%	-0.6%
LG411	78.2%	56.4%	99.4%	-21.8%	21.1%	-43.0%
LG427	56.0%	48.8%	59.5%	-7.3%	3.5%	-10.8%
LG967	100.0%	96.6%	96.9%	-3.4%	-3.1%	-0.3%
LG971	100.0%	97.7%	98.2%	-2.3%	-1.8%	-0.5%
LG656	76.5%	56.7%	70.7%	-19.8%	-5.8%	-14.0%
LG657	100.0%	99.5%	99.6%	-0.5%	-0.4%	-0.1%
LG969	100.0%	97.1%	98.2%	-2.9%	-1.8%	-1.2%
LG970	95.9%	96.8%	96.5%	0.9%	0.7%	0.2%
			Mean	0.3%	2.1%	-1.9%
			Median	-1.1%	-0.1%	-0.4%
			Max Abs	30.5%	31.3%	43.0%
			Min Abs	0.5%	0.2%	0.0%
			Std. Dev.	11.8%	10.7%	10.5%

Overall the inclusion of the steel bracing had a negligible impact on the numerical results of the fixed SMS FE simulations. Seven (7) models experienced changes in the energy absorption greater than 5% while the mean percent difference in energy absorption between the braced and unbraced models was determined to be 1.9% with a standard deviation of 10.5%. The energy absorption of the test LG411 experienced a substantial change due to the addition of the braces. The projectile initial velocities and orientations for the seven (7) models are provided below in Table 44.

Table 44. Projectile Orientation and Initial Velocity Data

Model	Roll (deg)	Pitch (deg)	Yaw (deg)	Init. Proj. Vel. (fps)	Ballistic Limit (fps)
LG618	-47.1	6.3	51.6	866	620-640
LG689	-12.8	-1.3	49.7	896	620-640
LG692	38.2	2.3	41.5	885	620-640
LG432	0.0	0.0	0.0	896	750-800
LG411	0.0	0.0	0.0	886	850-875
LG427	0.0	0.0	0.0	915	850-875
LG656	9.0	-2.3	-10.1	967	925-950

Models LG618, LG689 and LG692 all contained projectiles with extreme orientation angles, leading to increased variability in the percent energy absorbed. Models LG411, LG427 and LG656 all contained projectiles whose initial velocities are near the ballistic limit for the test fabric configuration, leading to increased variability in the percent energy absorbed between the braced and unbraced models.

6.1.2.3.2 Displacement

Results from the point of impact displacement analysis for fixed SMS models both with and without ring bracing are presented below in Table 45.

Table 45. Point of Impact Displacement Values: SMS Fixed Models

	Displacement (in)			
Test No.	NASA	Fixed	Fixed	% Diff:
LG963	2.6	6.9	7.0	-1.1%
LG964	3.0	5.4	5.4	0.0%
LG965	3.0	5.9	5.9	0.0%
LG967	2.7	4.3	4.4	-1.1%
LG969	3.2	4.7	4.6	1.1%
LG970	3.6	4.8	4.7	2.1%
LG971	2.5	4.4	4.2	4.0%
			Mean	0.7%
			Max	4.0%
			Min	-1.1%
			Std Dev	1.9%

The results above show a negligible effect on the results numerical simulations for the fixed SMS models with the addition of the ring bracing. Minimal differences are found between the mean percent energy absorption and the standard deviation of the model suite.

6.1.2.3.3 Damage

Results from the damage comparison analysis performed on fixed SMS models are provided below in Table 46.

Table 46. Damage Analysis Results: Fixed SMS Models

		NASA		Fixed-Braced		Fixed-Unbraced	
	No. Layers	Pen	Dam	Pen	Dam	Pen	Dam
LG404	8	8	0	8	0	8	0
LG965	16	16	0	0	0	0	0
LG967	24	0	10	0	0	0	0
LG969	32	3	8	0	8	0	4
LG971	24	0	13	0	0	0	0

Damage results for the model LG404 most accurately resemble the damage observed during ballistic testing as all eight (8) layers of fabric were penetrated. The damage incurred by the 900 series (Phase III) models began to deviate from the damage observed during experimental testing. The LG965 model (16 fabric layers) ballistic test resulted in 16 penetrated layers. However, FE modeling of LG965 resulted in no layers neither damaged nor penetrated for both the braced and unbraced conditions. Similarly, the experimental results for LG967 (32 total fabric layers) included 10 damaged layers while the FE model resulted in zero damaged layers. The test LG969 (24 total layers) resulted in three (3) penetrated layers and eight (8) damaged layers during experimental testing. For all of the Phase III test cases considered above, the FE simulations underpredicted the damage to the Kevlar® fabric.

6.1.2.4 SMS/Free Models

6.1.2.4.1 Energy Absorption

A comparison of the energies absorbed by the free SMS models both with and without bracing is provided below in Table 47.

Table 47. Energy Absorption Results: SMS/Free Braced vs. Unbraced Models

	% Energy Absorbed			Difference		
Test No.	NASA	Free Braced	Free Unbraced	NASA - Braced	NASA - Unbraced	Braced-Unbraced
LG963	67.4%	97.9%	98.5%	30.5%	31.1%	-0.6%
LG404	16.1%	22.5%	22.7%	6.3%	6.5%	-0.2%
LG409	17.6%	18.8%	18.8%	1.2%	1.2%	0.0%
LG424	20.1%	28.2%	28.6%	8.0%	8.5%	-0.4%
LG594	67.0%	84.5%	81.2%	17.5%	14.1%	3.3%
LG609	18.4%	18.1%	17.5%	-0.3%	-0.9%	0.6%

LG610	16.9%	16.2%	16.2%	-0.7%	-0.6%	-0.1%
LG611	22.4%	33.6%	27.5%	11.3%	5.1%	6.2%
LG612	16.1%	14.4%	14.2%	-1.7%	-2.0%	0.2%
LG618	58.4%	77.2%	62.6%	18.8%	4.3%	14.6%
LG620	57.8%	66.6%	60.4%	8.8%	2.6%	6.1%
LG689	46.6%	35.4%	35.8%	-11.2%	-10.7%	-0.5%
LG692	53.7%	38.9%	39.4%	-14.8%	-14.3%	-0.6%
LG966	93.4%	100.0%	100.0%	6.6%	6.6%	0.0%
LG429	38.4%	35.1%	34.8%	-3.3%	-3.6%	0.3%
LG432	47.4%	33.6%	33.8%	-13.8%	-13.6%	-0.2%
LG965	100.0%	95.9%	96.6%	-4.1%	-3.4%	-0.7%
LG964	98.1%	97.1%	97.1%	-1.0%	-1.0%	0.0%
LG411	78.2%	52.3%	53.3%	-25.9%	-24.9%	-1.0%
LG427	56.0%	49.5%	48.6%	-6.5%	-7.4%	0.9%
LG967	100.0%	97.1%	97.1%	-2.9%	-2.9%	0.1%
LG971	100.0%	98.3%	98.3%	-1.7%	-1.7%	0.0%
LG656	76.5%	56.6%	58.6%	-19.9%	-17.9%	-2.0%
LG657	100.0%	99.6%	99.6%	-0.4%	-0.4%	0.0%
LG969	100.0%	97.8%	97.7%	-2.2%	-2.3%	0.1%
LG970	95.9%	97.5%	97.5%	1.6%	1.7%	0.0%
			Mean	0.0%	-1.0%	1.0%
			Median	-0.9%	-0.9%	0.0%
			Max Abs	30.5%	31.1%	14.6%
			Min Abs	0.3%	0.4%	0.0%
			Std. Dev.	12.1%	10.8%	3.4%

The results presented above indicate that the inclusion of the ring wall braces in the free SMS finite element models has a negligible impact on the numerical results. There was minimal change in both the mean (1.0%) and standard deviation (3.4%) between the braced and unbraced solutions while only three (3) models experienced changes in energy absorption greater than 5%; LG611, LG618 and LG620. The projectile orientations for these three tests is provided below in Table 48.

Table 48. Projectile Orientations at Time of Impact

Model	Roll (deg)	Pitch (deg)	Yaw (deg)
LG611	30.9	-1.7	-10.8
LG618	-47.1	6.3	51.6
LG620	-37.8	0.2	55.1

The extreme projectile orientation angles at the time of impact for the three tests increase the potential for variability in the values for percent energy absorbed.

6.1.2.4.2 Displacement

Results from the point of impact displacement analysis for free SMS models both with and without bracing are presented below in Table 49

Table 49. Point of Impact Displacement Values: SMS Free Models

	Displacement (in)			
Test No.	NASA ARAMIS	Free Braced	Free Unbraced	% Diff: Braced/Unbraced
LG963	2.6	6.9	7.0	-1.4%
LG964	3.0	5.4	5.4	0.4%
LG965	3.0	6.0	6.0	-0.2%
LG967	2.7	4.2	4.3	-1.4%
LG969	3.2	4.6	4.7	-0.9%
LG970	3.6	4.8	4.8	-0.2%
LG971	2.5	4.3	4.3	-0.7%
			Mean	-0.6%
			Max	0.4%
			Min	-1.4%
			Std Dev	0.7%

The inclusion of the ring braces is shown to have had little to no effect on the results of the numerical simulations for the free SMS models. The mean difference in the maximum point of impact displacement between the two model configurations changed only 0.6% with minimal change in the standard deviation.

6.1.2.4.3 Damage

Results from the damage comparison analysis performed on free SMS models are provided below in Table 50.

Table 50. Damage Analysis Results: Free SMS Models

		NASA		Free-Braced		Free-Unbraced	
	No. Layers	Pen	Dam	Pen	Dam	Pen	Dam
LG404	8	8	0	8	0	8	0
LG965	16	16	0	0	0	0	0
LG967	24	0	10	0	0	0	0
LG969	32	3	8	0	8	0	8
LG971	24	0	13	0	0	0	0

Again, the damage results for model LG404 most accurately resemble the damage observed during ballistic testing as all eight (8) layers of fabric were penetrated for both the ballistic test and the numerical simulation. The damages incurred by the 900 series (Phase III) models began to deviate from the damages observed during experimental testing. The LG965 model (16 fabric layers) ballistic test resulted in 16 penetrated layers. However, FE modeling of LG965 resulted in no layers neither damaged nor penetrated for both the braced and unbraced conditions. Similarly, the experimental results for LG967 (32 total fabric layers) included 10 damaged layers while the FE model resulted in zero damaged layers. The test LG969 (24 total layers) resulted in three (3) penetrated layers and eight (8) damaged layers during experimental testing. For all of the Phase III test cases considered above, the FE simulations underpredicted the damage to the Kevlar® fabric.

6.1.3 Effect of Translational Constraint

6.1.3.1 CMS/Braced Models

6.1.3.1.1 Energy Absorption

A comparison of the energies absorbed by the CMS-braced models both with and without translational constraints is provided below in

Table 51 51.

Table 51. Energy Absorption Results: CMS/Braced Fixed vs. Free Models

% Energy Absorbed				Difference		
Test No.	NASA	Braced Fixed	Braced Free	NASA - Fixed	NASA - Free	Fixed - Free
LG963	67.4%	97.2%	97.5%	29.8%	30.1%	-0.2%
LG404	16.1%	11.3%	12.1%	-4.9%	-4.0%	-0.9%
LG409	17.6%	14.9%	14.7%	-2.7%	-2.9%	0.2%
LG424	20.1%	17.0%	18.5%	-3.2%	-1.6%	-1.5%
LG594	67.0%	90.3%	88.6%	23.3%	21.5%	1.7%
LG609	18.4%	14.9%	14.7%	-3.5%	-3.7%	0.2%
LG610	16.9%	21.5%	22.6%	4.6%	5.8%	-1.2%
LG611	22.4%	24.0%	27.4%	1.6%	5.0%	-3.4%
LG612	16.1%	20.8%	20.6%	4.7%	4.5%	0.2%
LG618	58.4%	77.4%	81.4%	19.0%	23.0%	-4.0%
LG620	57.8%	69.2%	81.7%	11.4%	24.0%	-12.5%
LG689	46.6%	45.2%	52.7%	-1.4%	6.1%	-7.5%
LG692	53.7%	75.6%	82.1%	21.9%	28.5%	-6.5%
LG966	93.4%	99.6%	99.7%	6.1%	6.3%	-0.2%
LG429	38.4%	23.4%	23.2%	-15.0%	-15.2%	0.2%
LG432	47.4%	26.7%	27.7%	-20.7%	-19.7%	-1.0%
LG965	100.0%	93.5%	94.1%	-6.5%	-5.9%	-0.6%
LG964	98.1%	90.5%	91.7%	-7.6%	-6.4%	-1.2%
LG411	78.2%	86.0%	78.8%	7.8%	0.6%	7.2%
LG427	56.0%	51.8%	48.9%	-4.2%	-7.1%	2.9%
LG967	100.0%	95.9%	96.6%	-4.1%	-3.4%	-0.7%
LG971	100.0%	97.9%	98.1%	-2.1%	-1.9%	-0.2%
LG656	76.5%	95.7%	81.9%	19.2%	5.4%	13.8%

LG657	100.0%	100.0%	100.0%	0.0%	0.0%	0.0%
LG969	100.0%	99.1%	98.5%	-0.9%	-1.5%	0.6%
LG970	95.9%	98.3%	98.0%	2.4%	2.1%	0.3%
			Mean	2.9%	3.4%	-0.5%
			Median	-0.5%	0.3%	-0.2%
			Max Abs	29.8%	30.1%	13.8%
			Min Abs	0.0%	0.0%	0.0%
			Std. Dev.	11.9%	12.6%	4.6%

The results presented above indicate that the inclusion of the translational constraints in the braced CMS finite element models has a negligible impact on the numerical results. There was minimal change in both the mean (0.5%) and standard deviation (4.6%) between the fixed and free models while only two (2) models experienced changes in energy absorption greater than 10% (LG620 – 12.5% and LG656 – 13.8%).

Table 52. Projectile Orientation and Initial Velocity Information

Model	Roll (deg)	Pitch (deg)	Yaw (deg)	Init. Proj. Vel. (fps)	Ballistic Limit (fps)
LG620	-47.1	6.3	51.6	866	620-640
LG689	-12.8	-1.3	49.7	896	620-640
LG692	38.2	2.3	41.5	885	620-640
LG411	0.0	0.0	0.0	886	850-875
LG656	9.0	-2.3	-10.1	967	925-950

Tests LG620, LG689 and LG692 all contained projectiles whose initial velocities were well above the ballistic limits of the fabric configuration. However, the initial projectile orientation caused some variance between the fixed and the free finite element models.

6.1.3.1.2 Displacement

Results from the point of impact displacement analysis for braced CMS models both with and without translational constraints are presented below in Table 53.

Table 53. Point of Impact Displacement Values: Braced CMS Models

	Displacement (in)			
Test No.	NASA	Braced	Braced	% Diff:
LG963	2.6	7.1	7.0	1.6%
LG964	3.0	5.4	5.4	1.3%
LG965	3.0	5.6	5.5	1.6%
LG967	2.7	4.1	4.0	2.5%
LG969	3.2	4.4	4.2	4.0%
LG970	3.6	4.6	4.7	-1.1%
LG971	2.5	4.1	4.0	1.8%
			Mean	1.7%
			Max	4.0%
			Min	-1.1%
			Std Dev	1.5%

The inclusion of the translational constraints is shown to have had little to no effect on the results of the numerical simulations for the braced SMS models. The mean difference in the maximum point of impact displacement between the two model configurations changed only 1.7% with minimal change in the standard deviation (1.5%).

6.1.3.1.3 Damage

Results from the damage comparison analysis performed on braced CMS models are provided below in Table 54.

Table 54. Damage Analysis Results: Braced CMS Models

		NASA		Braced-Fixed		Braced-Free	
	No. Layers	Pen	Dam	Pen	Dam	Pen	Dam
LG404	8	8	0	8	0	8	0
LG965	16	16	0	0	0	0	0
LG967	24	0	10	0	4	0	0
LG969	32	3	8	0	4	0	4
LG971	24	0	13	0	0	0	0

The damage results for model LG404 most accurately resemble the damage observed during ballistic testing as all eight (8) layers of fabric were penetrated for both the ballistic test and the numerical simulation. This is due to the velocity of the projectile with respect to the ballistic limit of the fabric configuration. The damages incurred by the 900 series (Phase III) models began to deviate from the damages observed during experimental testing. The LG965 model (16 fabric layers) ballistic test resulted in 16 penetrated layers. However, FE modeling of LG965 resulted in no layers neither damaged nor penetrated for both the braced and unbraced conditions. Similarly, the experimental results for LG967 (32 total fabric layers) included 10 damaged layers while the FE model resulted in zero damaged layers. The test LG969 (24 total layers) resulted in three (3) penetrated layers and eight (8) damaged layers during experimental testing. For all of the Phase III test cases considered above, the FE simulations underpredicted the damage to the Kevlar® fabric.

6.1.3.2 CMS/Unbraced Models

6.1.3.2.1 Energy Absorption

A comparison of the energies absorbed by the CMS-unbraced models both with and without translational constraints is provided below in

Table 55 55.

Table 55. Energy Absorption Results: CMS/Unbraced Fixed vs. Free Models

	% Energy Absorbed			Difference		
Test No.	NASA	Unbraced Fixed	Unbraced Free	NASA - Fixed	NASA - Free	Fixed - Free
LG963	67.4%	99.2%	98.5%	31.8%	31.1%	0.7%
LG404	16.1%	16.4%	16.4%	0.3%	0.2%	0.1%
LG409	17.6%	15.0%	14.5%	-2.6%	-3.1%	0.4%
LG424	20.1%	17.5%	18.6%	-2.6%	-1.5%	-1.2%
LG594	67.0%	94.0%	97.1%	27.0%	30.0%	-3.1%
LG609	18.4%	15.0%	14.5%	-3.4%	-3.9%	0.5%
LG610	16.9%	21.9%	21.1%	5.0%	4.2%	0.8%
LG611	22.4%	23.4%	25.6%	1.0%	3.2%	-2.2%
LG612	16.1%	20.5%	21.7%	4.4%	5.6%	-1.2%
LG618	58.4%	72.8%	71.9%	14.4%	13.5%	0.9%
LG620	57.8%	77.2%	77.2%	19.4%	19.4%	0.0%
LG689	46.6%	48.3%	49.2%	1.7%	2.6%	-0.9%
LG692	53.7%	76.8%	70.4%	23.2%	16.7%	6.4%
LG966	93.4%	98.9%	99.1%	5.5%	5.7%	-0.2%
LG429	38.4%	23.7%	21.9%	-14.6%	-16.5%	1.8%
LG432	47.4%	30.5%	27.0%	-16.9%	-20.4%	3.5%
LG965	100.0%	92.5%	94.4%	-7.5%	-5.6%	-1.8%
LG964	98.1%	92.9%	92.9%	-5.2%	-5.2%	0.0%
LG411	78.2%	88.7%	86.4%	10.5%	8.1%	2.3%
LG427	56.0%	51.5%	53.5%	-4.5%	-2.5%	-2.0%
LG967	100.0%	95.6%	96.7%	-4.4%	-3.3%	-1.1%
LG971	100.0%	97.9%	98.2%	-2.1%	-1.8%	-0.4%
LG656	76.5%	81.3%	69.3%	4.8%	-7.2%	12.0%
LG657	100.0%	99.9%	99.9%	-0.1%	-0.1%	-0.1%

LG969	100.0%	98.2%	98.7%	-1.8%	-1.3%	-0.5%
LG970	95.9%	97.2%	98.0%	1.3%	2.2%	-0.8%
			Mean	3.2%	2.7%	0.5%
			Median	0.6%	0.1%	0.0%
			Max Abs	31.8%	31.1%	12.0%
			Min Abs	0.1%	0.1%	0.0%
			Std. Dev.	11.8%	11.9%	3.0%

The results presented above indicate that the inclusion of the translational constraints in the unbraced CMS finite element models has a negligible impact on the numerical results. There was minimal change in both the mean (0.5%) and standard deviation (3.0%) between the fixed and free solutions while only two (2) models experienced changes in energy absorption greater than 5%; LG692 and LG656. The projectile orientation and velocity information for these two tests are provided below in Table 56.

Table 56. Projectile Orientation and Velocity Information

Model	Roll (deg)	Pitch (deg)	Yaw (deg)	Init. Proj. Vel. (fps)	Ballistic Limit (fps)
LG692	38.2	2.3	41.5	885	620-640
LG656	9.0	-2.3	-10.1	967	925-950

The variance in the percent energy absorption for model LG692 can be attributed to the extreme projectile orientation at the time of impact with the fabric layers. The initial projectile velocity for model LG656 is near the ballistic limit for the fabric configuration, leading to increased variability in the energy absorption characteristics.

6.1.3.2.2 Displacement

Results from the point of impact displacement analysis for unbraced CMS models both with and without translational constraints are presented below in Table 57.

Table 57. Point of Impact Displacement Values: Unbraced CMS Models

	Displacement (in)			
Test No.	NASA ARAMIS	Unbraced Fixed	Unbraced Free	% Diff: Fixed/Free
LG963	2.6	7.0	7.0	-0.4%
LG964	3.0	4.9	5.4	-8.0%
LG965	3.0	5.5	5.6	-0.2%
LG967	2.7	4.1	4.0	3.0%
LG969	3.2	4.3	4.3	0.0%
LG970	3.6	4.6	4.7	-0.4%
LG971	2.5	4.1	4.1	-0.2%
			Mean	-0.9%
			Max	3.0%
			Min	-8.0%
			Std Dev	3.4%

The inclusion of the translational constraints is shown to have had little to no effect on the results of the numerical simulations for the unbraced CMS models. The mean difference in the maximum displacement of the point of impact between the two model configurations changed only 0.9% with negligible change in the standard deviation (3.4%).

6.1.3.2.3 Damage

Results from the damage comparison analysis performed on the unbraced CMS model suite is provided below in Table 58.

Table 58. Damage Analysis Results: Unbraced CMS Models

		NASA		Unbraced-		Unbraced-Free	
	No. Layers	Pen	Dam	Pen	Dam	Pen	Dam
LG404	8	8	0	8	0	8	0
LG965	16	16	0	0	0	0	0
LG967	24	0	10	0	0	0	0
LG969	32	3	8	0	4	0	8
LG971	24	0	13	0	0	0	0

Similarly to previous damage results, the Phase III (900 series) FE models underpredicted the damage to the fabric layers. Once again, the damage incurred by the model LG404, the only non-Phase III simulation, accurately matched the damage experienced by the experimental test specimen.

6.1.3.3 SMS/Braced Models

6.1.3.3.1 Energy Absorption

A comparison of the energies absorbed by the SMS-braced models both with and without translational constraints is provided below in Table 59.

Table 59. Energy Absorption Results: SMS/Braced Fixed vs. Free Models

	% Energy Absorbed			Difference		
Test No.	NASA	Braced Fixed	Braced Free	NASA - Fixed	NASA - Free	Fixed - Free
LG963	67.4%	97.9%	97.9%	30.5%	30.5%	0.0%
LG404	16.1%	20.7%	22.5%	4.5%	6.3%	-1.8%
LG409	17.6%	20.0%	18.8%	2.4%	1.2%	1.2%
LG424	20.1%	28.2%	28.2%	8.0%	8.0%	0.0%
LG594	67.0%	92.5%	84.5%	25.5%	17.5%	8.0%
LG609	18.4%	17.9%	18.1%	-0.5%	-0.3%	-0.2%
LG610	16.9%	16.0%	16.2%	-0.9%	-0.7%	-0.2%
LG611	22.4%	33.5%	33.6%	11.1%	11.3%	-0.2%
LG612	16.1%	14.8%	14.4%	-1.3%	-1.7%	0.4%
LG618	58.4%	72.7%	77.2%	14.3%	18.8%	-4.5%
LG620	57.8%	63.5%	66.6%	5.7%	8.8%	-3.0%
LG689	46.6%	43.5%	35.4%	-3.0%	-11.2%	8.1%

LG692	53.7%	38.0%	38.9%	-15.7%	-14.8%	-0.9%
LG966	93.4%	100.0%	100.0%	6.6%	6.6%	0.0%
LG429	38.4%	34.6%	35.1%	-3.8%	-3.3%	-0.5%
LG432	47.4%	33.8%	33.6%	-13.6%	-13.8%	0.2%
LG965	100.0%	96.1%	95.9%	-3.9%	-4.1%	0.2%
LG964	98.1%	96.3%	97.1%	-1.8%	-1.0%	-0.7%
LG411	78.2%	56.4%	52.3%	-21.8%	-25.9%	4.1%
LG427	56.0%	48.8%	49.5%	-7.3%	-6.5%	-0.8%
LG967	100.0%	96.6%	97.1%	-3.4%	-2.9%	-0.5%
LG971	100.0%	97.7%	98.3%	-2.3%	-1.7%	-0.5%
LG656	76.5%	56.7%	56.6%	-19.8%	-19.9%	0.1%
LG657	100.0%	99.5%	99.6%	-0.5%	-0.4%	-0.1%
LG969	100.0%	97.1%	97.8%	-2.9%	-2.2%	-0.8%
LG970	95.9%	96.8%	97.5%	0.9%	1.6%	-0.7%
			Mean	0.3%	0.0%	0.3%
			Median	-1.1%	-0.9%	-0.2%
			Max Abs	30.5%	30.5%	8.1%
			Min Abs	0.5%	0.3%	0.0%
			Std. Dev.	11.8%	12.1%	2.7%

The results presented above indicate that the inclusion of the translational constraints in the braced SMS finite element models has a negligible impact on the numerical results. There was minimal change in both the mean (0.3%) and standard deviation (2.7%) between the fixed and free solutions while only two (2) models experienced changes in energy absorption greater than 5%. The projectile orientation and velocity information for these two models is provided below in Table 60.

Table 60. Projectile Orientation and Velocity Information

Model	Roll (deg)	Pitch (deg)	Yaw (deg)	Init. Proj. Vel. (fps)	Ballistic Limit (fps)
LG594	27.0	6.6	47.8	844	620-640
LG689	-12.8	-1.3	49.7	896	620-640

It is observed that the initial projectile velocities for both tests are well above the ballistic limits for the fabric configurations, therefore, the variability observed in the percent energy absorption values between the fixed and free models can be attributed to the extreme projectile orientations at impact.

6.1.3.3.2 Displacement

Results from the point of impact displacement analysis for braced SMS models both with and without translational constraints are presented below in Table 61.

Table 61. Point of Impact Displacement Values: Braced SMS Models

	Displacement (in)			
Test No.	NASA ARAMIS	Braced Fixed	Braced Free	% Diff: Fixed/Free
LG963	2.6	6.9	6.9	0.3%
LG964	3.0	5.4	5.4	0.2%
LG965	3.0	5.9	6.0	-1.8%
LG967	2.7	4.3	4.2	1.4%
LG969	3.2	4.7	4.6	0.2%
LG970	3.6	4.8	4.8	0.8%
LG971	2.5	4.4	4.3	3.3%
			Mean	0.6%
			Max	3.3%
			Min	-1.8%
			Std Dev	1.5%

The inclusion of the translational constraints is shown to have had little to no effect on the results of the numerical simulations for the braced SMS models. The mean difference in the maximum displacement of the point of impact between the two model configurations changed only 0.6% with negligible change in the standard deviation (1.5%).

6.1.3.3.3 Damage

Results from the damage comparison analysis performed on braced SMS models are provided below in Table 62.

Table 62. Damage Analysis Results: Braced SMS Models

		NASA		Braced-Fixed		Braced-Free	
	No. Layers	Pen	Dam	Pen	Dam	Pen	Dam
LG404	8	8	0	8	0	8	0
LG965	16	16	0	0	0	0	0
LG967	24	0	10	0	0	0	0
LG969	32	3	8	0	8	0	8
LG971	24	0	13	0	0	0	0

Similarly to previous damage results, the Phase III (900 series) FE models underpredicted the damage to the fabric layers. Once again, the damage incurred by the model LG404, the only non-Phase III simulation, accurately matched the damage experienced by the experimental test specimen.

6.1.3.4 SMS/Unbraced Models

6.1.3.4.1 Energy Absorption

A comparison of the energies absorbed by the SMS-unbraced models both with and without translational constraints is provided below in Table 63.

Table 63. Energy Absorption Results: SMS/Unbraced Fixed vs. Free Models

	% Energy Absorbed			Difference		
Test No.	NASA	Unbraced Fixed	Unbraced Free	NASA - Fixed	NASA - Free	Fixed - Free
LG963	67.4%	98.7%	98.5%	31.3%	31.1%	0.2%
LG404	16.1%	20.6%	22.7%	4.5%	6.5%	-2.0%
LG409	17.6%	24.2%	18.8%	6.6%	1.2%	5.4%
LG424	20.1%	24.5%	28.6%	4.4%	8.5%	-4.1%
LG594	67.0%	95.2%	81.2%	28.2%	14.1%	14.0%

LG609	18.4%	15.0%	17.5%	-3.4%	-0.9%	-2.5%
LG610	16.9%	17.1%	16.2%	0.2%	-0.6%	0.8%
LG611	22.4%	28.1%	27.5%	5.8%	5.1%	0.6%
LG612	16.1%	10.9%	14.2%	-5.2%	-2.0%	-3.3%
LG618	58.4%	60.3%	62.6%	1.9%	4.3%	-2.3%
LG620	57.8%	60.5%	60.4%	2.7%	2.6%	0.1%
LG689	46.6%	26.6%	35.8%	-19.9%	-10.7%	-9.2%
LG692	53.7%	45.6%	39.4%	-8.1%	-14.3%	6.1%
LG966	93.4%	100.0%	100.0%	6.6%	6.6%	0.0%
LG429	38.4%	36.5%	34.8%	-1.9%	-3.6%	1.7%
LG432	47.4%	41.9%	33.8%	-5.5%	-13.6%	8.1%
LG965	100.0%	96.3%	96.6%	-3.7%	-3.4%	-0.3%
LG964	98.1%	96.9%	97.1%	-1.2%	-1.0%	-0.2%
LG411	78.2%	99.4%	53.3%	21.1%	-24.9%	46.1%
LG427	56.0%	59.5%	48.6%	3.5%	-7.4%	10.9%
LG967	100.0%	96.9%	97.1%	-3.1%	-2.9%	-0.1%
LG971	100.0%	98.2%	98.3%	-1.8%	-1.7%	-0.1%
LG656	76.5%	70.7%	58.6%	-5.8%	-17.9%	12.1%
LG657	100.0%	99.6%	99.6%	-0.4%	-0.4%	0.0%
LG969	100.0%	98.2%	97.7%	-1.8%	-2.3%	0.5%
LG970	95.9%	96.5%	97.5%	0.7%	1.7%	-1.0%
			Mean	2.1%	-1.0%	3.1%
			Median	-0.1%	-0.9%	0.0%
			Max Abs	31.3%	31.1%	46.1%
			Min Abs	0.2%	0.4%	0.0%
			Std. Dev.	10.7%	10.8%	10.2%

Overall the inclusion of the translational constraints had a negligible impact on the numerical results of the unbraced SMS FE simulations. Seven (7) models experienced changes in the energy absorption greater than 5% while the mean percent difference in energy absorption between the braced and unbraced models as 3.1% with a standard deviation of 10.2%. The projectile orientation and velocity information for these seven (7) models is provided below in Table 64.

Table 64. Projectile Orientation and Velocity Information

Model	Roll (deg)	Pitch (deg)	Yaw (deg)	Init. Proj. Vel. (fps)	Ballistic Limit (fps)
LG594	27.0	6.6	47.8	844	620-640
LG689	-12.8	-1.3	49.7	896	620-640
LG692	38.2	2.3	41.5	885	620-640
LG432	0.0	0.0	0.0	896	750-800
LG411	0.0	0.0	0.0	886	850-875
LG427	0.0	0.0	0.0	915	850-875
LG656	9.0	-2.3	-10.1	967	925-950

The variance observed in the energy absorption for models LG594, LG689 and LG692 can be attributed to the extreme projectile orientation at the time of impact. The other four models, LG432, LG411, LG427 and LG656 all contain projectiles whose velocities at impact are near the ballistic limit for the test fabric configuration, leading to increased variability in the energy absorption characteristics of the test setup.

6.1.3.4.2 Displacement

Results from the point of impact displacement analysis for unbraced SMS models both with and without translational constraints are presented below in Table 65.

Table 65. Point of Impact Displacement Values: Unbraced SMS Models

	Displacement (in)			
Test No.	NASA ARAMIS	Unbraced Fixed	Unbraced Free	% Diff: Fixed/Free
LG963	2.6	7.0	7.0	0.0%
LG964	3.0	5.4	5.4	0.6%
LG965	3.0	5.9	6.0	-2.0%
LG967	2.7	4.4	4.3	1.2%
LG969	3.2	4.6	4.7	-1.7%
LG970	3.6	4.7	4.8	-1.5%
LG971	2.5	4.2	4.3	-1.4%
			Mean	-0.7%
			Max	1.2%
			Min	-2.0%
			Std Dev	1.2%

The inclusion of the translational constraints is shown to have had little to no effect on the results of the numerical simulations for the unbraced SMS models. The mean difference in the maximum displacement of the point of impact between the two model configurations changed only -0.7% with negligible change in the standard deviation (1.2%).

6.1.3.4.3 Damage

Results from the damage comparison analysis performed on unbraced SMS models is provided below in Table 66.

Table 66. Damage Analysis Results: Unbraced SMS Models

		NASA		Unbraced-Fixed		Unbraced-Free	
	No. Layers	Pen	Dam	Pen	Dam	Pen	Dam
LG404	8	8	0	8	0	8	0
LG965	16	16	0	0	0	0	0
LG967	24	0	10	0	0	0	0
LG969	32	3	8	0	4	0	8
LG971	24	0	13	0	0	0	0

Similarly to previous damage results, the Phase III (900 series) FE models underpredicted the damage to the fabric layers. Once again, the damage incurred by the model LG404, the only non-Phase III simulation, accurately matched the damage experienced by the experimental test specimen.

6.1.4 Discussion of Results

Overall the imposition of experimental boundary conditions had negligible effects on the results of the finite element simulations. The average percent change in energy absorption for all cases was 0.36% while the average standard deviation for the comparisons was 4.2%. The results from both displacement and damage comparisons indicate a negligible effect on these quantities due to the inclusion of experimental boundary conditions.

A summary of the energy absorption results from the different modeling configurations is presented below in Table 67.

Table 67. % Absorbed Energy Comparison with NASA Ballistic Tests (ASU V1.3)

MODEL	Mean	Max	Min	Std. Dev
CMS Free Unbraced	2.7%	31.1%	10.0%	11.9%
CMS Free Braced	3.4%	30.1%	0.0%	12.6%
CMS Fixed Unbraced	3.2%	31.8%	0.1%	11.8%
CMS Fixed Braced	2.9%	29.8%	0.0%	11.9%
SMS Free Unbraced	-1.0%	31.1%	0.4%	10.8%
SMS Free Braced	0.0%	30.5%	0.3%	12.1%
SMS Fixed Unbraced	2.1%	31.3%	0.2%	10.7%
SMS Fixed Braced	0.3%	30.5%	0.5%	11.8%

7 MAT234 – UMAT48 COMPARISON RESULTS

Results from the numerical simulation of NASA GRC ballistic testing of Kevlar® 49 fabric implementing MAT234 are presented below. The energy absorbed by the model system, the damage sustained by the fabric layers and the QA/QC checks (internal energy ratio, kinetic energy ratio, hourglass energy ratio and sliding energy ratio) are analyzed and these results are compared against the same quantities when utilizing the ASU UMAT48 V1.3 user-defined material model.

7.1 Absorbed Energy

The energy absorbed by the MAT234 model systems is outlined in Table 68 below.

Table 68. FE model energy absorbed: MAT234

	% Energy Absorbed		% Difference
Test No.	NASA	MAT234	NASA/MAT234
LG963	67.40%	19.12%	-48.28%
LG404	16.10%	3.32%	-12.78%
LG409	17.60%	3.12%	-14.48%
LG424	20.10%	3.57%	-16.53%
LG594	67.00%	21.03%	-45.97%
LG609	18.40%	2.39%	-16.01%
LG610	16.90%	8.59%	-8.31%
LG611	22.40%	8.85%	-13.55%
LG612	16.10%	3.97%	-12.13%
LG618	58.40%	17.18%	-41.22%
LG620	57.80%	21.91%	-35.89%
LG689	46.60%	13.76%	-32.84%
LG692	53.70%	12.68%	-41.02%
LG966	93.40%	21.32%	-72.08%
LG429	38.40%	6.94%	-31.46%
LG432	47.40%	6.60%	-40.80%
LG965	100.00%	29.23%	-70.77%
LG964	98.10%	32.67%	-65.43%

LG411	78.20%	9.86%	-68.34%
LG427	56.00%	9.59%	-46.41%
LG967	100.00%	72.30%	-27.70%
LG971	100.00%	33.38%	-66.62%
LG656	76.50%	19.47%	-57.03%
LG657	100.00%	27.04%	-72.96%
LG969	100.00%	17.86%	-82.14%
LG970	95.90%	17.49%	-78.41%

Variability in the determination of the final projectile velocity realized during ballistic testing is estimated at approximately 10%, therefore any FE model that experiences a percent absorbed energy (read final projectile velocity) that varies from the NASA test results by more than 10% is considered out of specification. All but one of the FAA models (LG610) fell outside of this limit. FE models of the ballistic testing greatly underpredicted the amount of energy absorbed by the fabric, with an average difference of approximately 43% (standard deviation = 24%).

Table 69 presents a comparison between the amount of energy absorbed when implementing the UMAT48 and MAT234 material models.

Table 69. Comparison of absorbed energy: NASA/UMAT48/MAT234

	% Energy Absorbed			Difference		
Test No.	NASA	UMAT48	MAT234	NASA/ MAT234	NASA/ UMAT48	UMAT48/ MAT234
LG963	67.40%	97.90%	19.12%	-48.28%	30.50%	-48.28%
LG404	16.10%	20.70%	3.32%	-12.78%	4.60%	-17.38%
LG409	17.60%	20.00%	3.12%	-14.48%	2.40%	-16.88%
LG424	20.10%	28.20%	3.57%	-16.53%	8.10%	-24.63%
LG594	67.00%	92.50%	21.03%	-45.97%	25.50%	-71.47%
LG609	18.40%	17.90%	2.39%	-16.01%	-0.50%	-15.51%
LG610	16.90%	16.00%	8.59%	-8.31%	-0.90%	-7.41%
LG611	22.40%	33.50%	8.85%	-13.55%	11.10%	-24.65%
LG612	16.10%	14.80%	3.97%	-12.13%	-1.30%	-10.83%

LG618	58.40%	72.70%	17.18%	-41.22%	14.30%	-55.52%
LG620	57.80%	63.50%	21.91%	-35.89%	5.70%	-41.59%
LG689	46.60%	43.50%	13.76%	-32.84%	-3.10%	-29.74%
LG692	53.70%	38.00%	12.68%	-41.02%	-15.70%	-25.32%
LG966	93.40%	100.00%	21.32%	-72.08%	6.60%	-78.68%
LG429	38.40%	34.60%	6.94%	-31.46%	-3.80%	-27.66%
LG432	47.40%	33.80%	6.60%	-40.80%	-13.60%	-27.20%
LG965	100.00%	96.10%	29.23%	-70.77%	-3.90%	-66.87%
LG964	98.10%	96.30%	32.67%	-65.43%	-1.80%	-63.63%
LG411	78.20%	56.40%	9.86%	-68.34%	-21.80%	-46.54%
LG427	56.00%	48.80%	9.59%	-46.41%	-7.20%	-39.21%
LG967	100.00%	96.60%	72.30%	-27.70%	-3.40%	-24.30%
LG971	100.00%	97.70%	33.38%	-66.62%	-2.30%	-64.32%
LG656	76.50%	56.70%	19.47%	-57.03%	-19.80%	-37.23%
LG657	100.00%	99.50%	27.04%	-72.96%	-0.50%	-72.46%
LG969	100.00%	97.10%	17.86%	-82.14%	-2.90%	-79.24%
LG970	95.90%	96.80%	17.49%	-78.41%	0.90%	-79.31%
			Max	-8.31%	30.50%	-7.41%
			Min	-82.14%	-79.31%	-79.31%
			Mean	-43.04%	0.28%	-42.15%
			Std. Dev	23.63%	11.83%	23.37%

The energy absorbed by the models implementing the UMAT48 material model more consistently represented the experimental ballistic test results than results from the MAT234 implementation. The MAT234 models underpredict the total energy absorbed by approximately 44% (Std. Dev = 24%) while the UMAT48 models varied from the experimental data by an average of 0.3% (Std. Dev. = 12%). The standard deviation of the FE model results is very near the variation inherent in the experimental data. This gross under prediction can be explained by considering the lack of a post-peak region in the material model. Much of the benefit of woven fabric materials is their high energy absorption properties (see Figure 83).

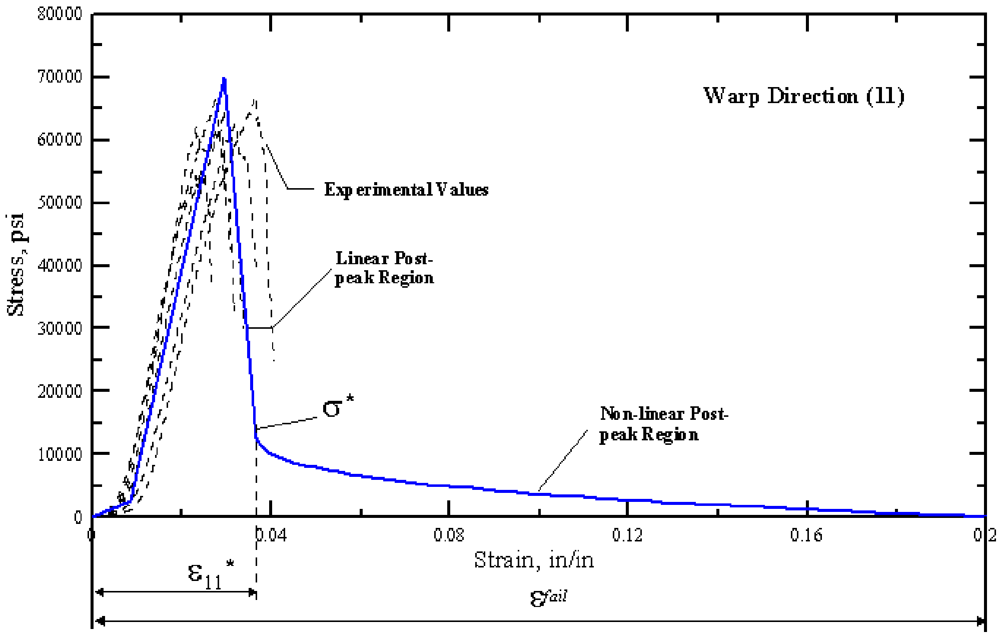

Figure 83. Stress strain response of Kevlar® 49 fabric: Warp Direction

Based on experimental testing of Kevlar® 49 fabric, it is evident that much of this energy is absorbed after the material has reached its peak stress. By only considering the stress strain response of the material up to the peak stress, the MAT234 material model neglects to account for much of the available energy absorption that could potentially be realized.

7.2 FE Model Damage

The resulting damage to the FE model fabric layers is presented below in Table 70.

Table 70. Damage comparison: NASA/UMAT48/MAT234

		NASA		UMAT48		M234	
	Total No. Layers	Pen.	Dam.	Pen.	Dam.	Pen.	Dam.
LG404	8	8	0	8	0	8	0
LG965	16	16	0	0	0	16	0
LG967	24	0	10	0	0	24	0
LG969	32	3	8	0	8	32	0
LG971	24	0	13	0	0	24	0

The damage realized by the MAT234 FE models above was consistent with the under-prediction of the absorbed energy described in Section 7.1. From the above results, it is clear that the MAT234 model over predicts in terms of failure of elements/damage of the fabric. In all of the runs, the projectile penetrates each fabric layer completely. Each model was characterized by the abrupt failure of the fabric elements in and around the area of impact of the projectile. All the models are uncontained and almost all the elements failed are located in the flat portion of the fabric, this is because of lack of propagation of stress waves beyond the flat portion of the fabric. Following are some important observations using MAT234 models.

1. From Figure 84 it is clear that the failure is in the flat portion and the failure is so sudden such that not much displacement of fabric is observed compared to the ASUumatv1.3-SMS model.

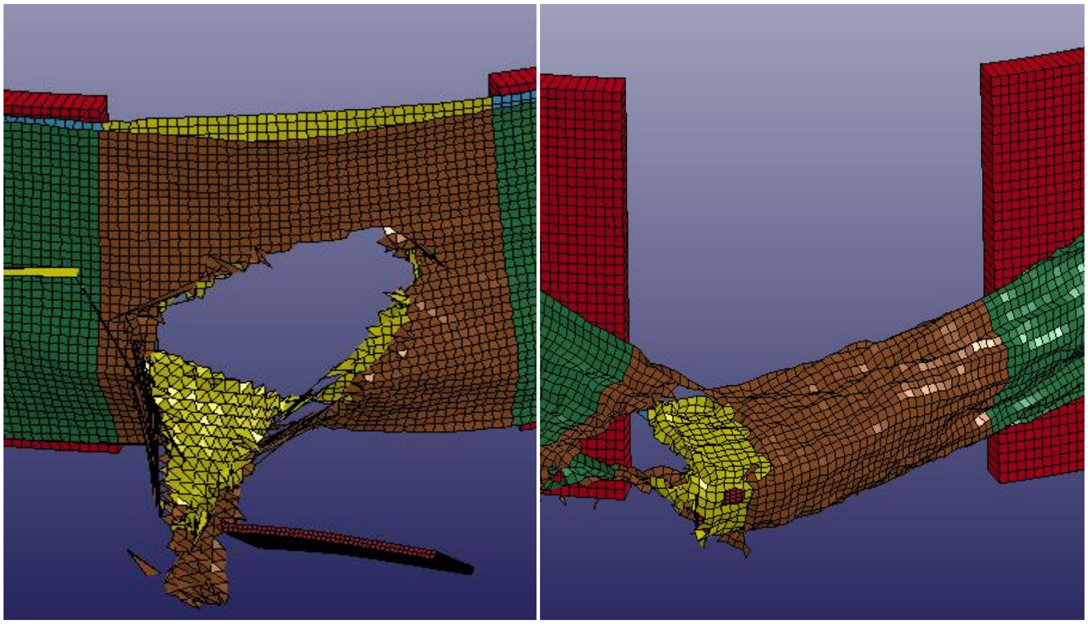

Figure 84. LG594 a) MAT234 b) UMAT48-SMS

2. In some of the models, heavy distortion of elements located near the impact region is observed. shows that for both the MAT234 and the ASUumatv1.3 versions of the LG620 model, the location of failed elements are same, but the displacement of fabric/element in the direction of projectile is not observed in MAT234. Heavy distortion of the fabric elements can also be seen and an important thing to note is that the propagation of stress wave due to impact is not at all observed in MAT234.
3. In Figure 85, good correlation is observed between the two models in terms of failed elements and damaged fabric portion, but the elements in MAT234 model are seen with high shear deformation and distortion.

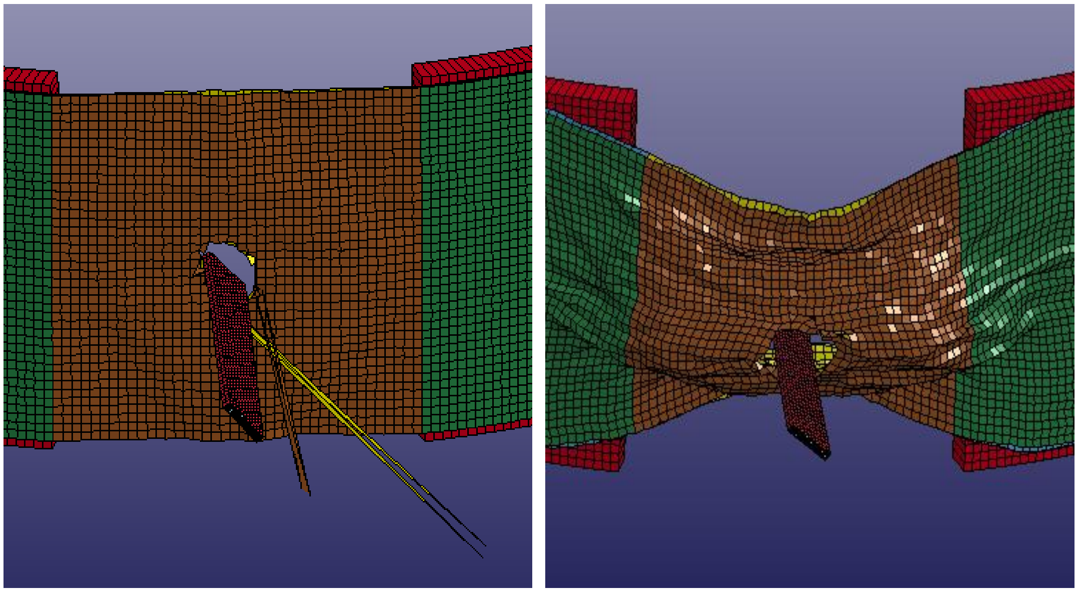

Figure 85. LG620 a) MAT234 b) UMAT48-SMS

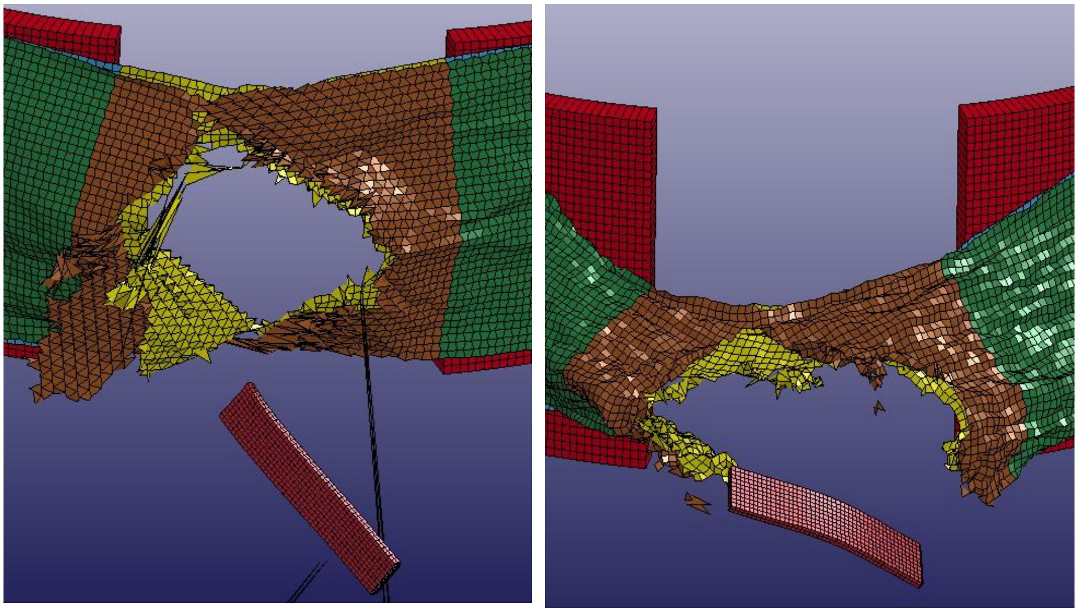

Figure 86. LG620 a) MAT234 b) ASUumatv1.3 (SMS)

7.3 QA/QC Checks

Results from the QA/QC check analysis are presented below in Table 71.

Table 71. QA/QC Checks: MAT234 FAA Model Suite

Test Case	Sliding Energy Ratio	Kinetic Energy Ratio	Internal Energy Ratio	Hourglass Energy Ratio
LG963	0.01	1.00	0.03	0.06
LG404	0.00	1.00	0.01	0.00
LG409	0.00	1.00	0.00	0.00
LG424	0.00	1.00	0.00	0.00
LG594	0.01	1.00	0.08	0.01
LG609	0.00	1.00	0.00	0.00
LG610	0.00	1.00	0.01	0.00
LG611	0.00	1.00	0.89	0.10
LG612	0.00	1.00	0.00	0.00
LG618	0.01	1.00	0.05	0.01
LG620	0.02	1.00	0.05	0.01
LG689	0.01	1.00	0.04	0.00
LG692	0.01	1.00	0.03	0.00
LG966	0.01	1.00	0.08	0.00
LG429	0.00	1.00	0.01	0.00
LG432	0.00	1.00	0.02	0.00
LG965	0.05	1.00	0.13	0.01
LG964	0.02	1.00	0.13	0.01
LG411	0.00	1.00	0.02	0.00
LG427	0.00	1.00	0.02	0.00
LG967	0.02	1.00	0.53	0.09
LG971	0.03	1.00	0.16	0.03
LG656	0.01	1.00	0.04	0.00
LG657	0.02	1.00	0.16	0.08
LG969	0.00	1.00	0.00	0.00
LG970	0.01	1.00	0.04	0.00

No models violated the threshold values for the QA/QC checks.

8 CONCLUSIONS AND DISCUSSION

8.1 Overview

In this research, improvements to the user defined material model UMAT48 for dry woven fabric were explored. The effects of implementing physical boundary conditions on the explicit LS-DYNA finite element simulations of NASA GRC ballistic testing of Kevlar® 49 fabric were determined. Static penetrator testing was performed on both single and double layer Kevlar® 49 fabric specimen and the resulting strains experienced by the fabric during testing were measured and compared against the corresponding strains from numerical simulations. The UMAT48 was compared against the material model MAT234 developed by Ivanov and Tabiei (Ivanov, et al., 2004).

8.2 Boundary Condition Study

The effect of implementing physical constraints on the numerical simulations of ballistic testing performed at NASA GRC was explored. Constraints placed on the FE models simulated the effects of triangular stiffeners applied to the wall of the steel ring and the fixity provided to the ring/fabric system by the support table apparatus. Both fabric modeling schemes (Concentric Modeling Scheme, or CMS and Spiral Modeling Scheme, or SMS) were considered. The inclusion of the simulated boundary conditions had a negligible effect on the energy absorption characteristics of the model systems, with an average percent change in energy absorption of 0.36% with an average standard deviation of 4.2%. The additional constraints also had negligible effects on the amount of damage to the model fabric.

8.3 Static Penetrator Testing

Static penetrator testing was performed in conjunction with this report. Both single and double layer specimens were tested and the resulting experimental strains were measured using the ARAMIS 3D optical strain measurement system. Results from the penetrator testing were inconclusive, therefore it is recommended that additional penetrator testing be performed and the use of the ARAMIS system for this measurement setup continue to be explored. It is recommended that a more thorough validation be performed prior to recording measurements to ensure accuracy utilizing this experimental setup. Additionally, future static penetrator testing should be performed until failure of the fabric to capture the load/displacement response of the fabric to this critical level. Allowing the fabric to fail provides another very important metric to validate the accuracy of the material model utilized.

8.4 MAT234 Comparison

Finite element simulations of ballistic testing of Kevlar® 49 fabric implementing the material model MAT234 (Ivanov & Tabiei, 2004) produced results that varied greatly from those obtained by implementing the UMAT48 material model. The amount of absorbed energy varied by an average of 44% with a standard deviation of 24%. The damage realized by the model fabric also varied between these two material models, with the MAT234 material resulting in complete penetration for almost all models, even those with projectile velocities well below the ballistic limit of the fabric. The QA/QC checks revealed few values falling outside of the allowable limits, indicating good quality modeling with limited energy distortion caused by hourglassing, sliding, etc. More research needs to be done to determine the appropriate settings for MAT234 to accurately reflect the behavior of Kevlar® 49 fabric. The values utilized in this report are based on the publicly available material model description and a published paper by the model developers. Further research should be performed to better match the response of MAT234 to that of Kevlar for ballistic applications.

REFERENCES

1. Bansal, Saurabh K. 2007. The Development of Micro-Mechanical Model of Kevlar Fabrics Used in Engine Containment System of Aircrafts. Arizona State University : M.S. Thesis, 2007.

2. Chawla, Krishnan Kumar. 2011. Composite Materials: Science and Engineering. s.l. : Springer, 2011.

3. Cowper, G.R. and Symonds, P S. 1957. Strain hardening and strain rate effect in the impact loading of cantilever beams. Providence, R.I. : Brown University, Department of Applied Mathematics, 1957.

4. Determination of Shear Modulus of Single Fibers. Tsai, C. L. and Daniel, I.M. 1999. Boston : Springer, 1999, Experimental Mechanics, V39, No. 4, pp. 284-286.

5. Dynamic Tensile Testing of Kevlar 49 Fabrics. Zhu, Deju, Mobasher, Barzin and Rajan, Subramaniam D. 2011. 2011, Journal of Materials in Civil Engineering: Vol 23 Issue 3, pp. 230-240.

6. Experimental and theoretical study on the strain rate and temperature dependence of mechanical behaviour of Kevlar fibre. Wang, Y and Xia, Y.M. 1999. 1999, Composites: Part A (30), pp. 1251-1257.

7. GOM. 2007. ARAMIS User Information - Hardware. Braunschweig, Germany : s.n., 2007. Technical Manual.

8. 2007. ARAMIS User Manual - Software. Braunschweig, Germany : s.n., 2007. Technical Manual.

9. Gomuc, Reha. 2004. Explicit Finite Element Modeling of Multilayer Composite Fabric for Gas Turbine Engine Containment Systems Part 4: Model Simulation for Ballistic Tests, Engine Fan Blade-Out, and Generic Engine. Washington, D.C. : Federal Aviation Administration, 2004. Technical Journal.

10. Ivanov, Ivelin and Tabiei, Ala. 2004. Loosely woven fabric model with viscoelastic crimped fibres for ballistic impact simulations. Online : International Journal for Numerical Methods in Engineering, 2004.

11. LS-DYNA. 2007. Keyword User's Manual: Version 971. Livermore, CA : Livermore Software Technology Corp., 2007.

12. Material and Geometrically Nonlinear Woven Composite Micro-Mechanical Model with Failure for Finite Element Simulations. Tabiei, A and Ivanov, I. 2004. 2004, Int J Non-Linear Mech, pp. 175-188.

13. Pereira, J Michael and Revilock, Duane M. 2004. Explicit Finite Element Modeling of Multilayer Composite Fabric for Gas Turbine Engine Containment Systems Part 2: Ballistic Impact Testing. Washington D.C. : Federal Aviation Administration, 2004. Technical Report.

14. Rajan, et al. 2009. Explicit Finite Element Modeling of Multilayer Composite Fabric for Gas Turbine Engine Containment Systems, Phase II Part1: Fabric Material Tests and Modeling. Washington D.C. : U.S. Department of Transportation: Federal Aviation Administration, 2009.

15. Rajan, S D, et al. 2004. Explicit Finite Element Modeling of Multilayer Composite Fabric for Gas Turbine Engine Containment Systems Part 1: Static Tests and Modeling. Washington D.C. : Federal Aviation Administration, 2004. Technical Report.

16. Rajan, S. D., et al. 2007. Explicit Finite Element Modeling of Multi-layer Composite Fabric for Gas Turbine Engine Containment Systems – Phase 3 Interim Report, Fabric Material Tests. Washington, D.C. : Federal Aviation Administration, 2007. Technical Report.

17. Revilock, Duane M and Pereira, J Michael. 2007. FAA Development Of Reliable Modeling Methodologies For Fan Blade Out Containment Analysis Part 2: Ballistic Impact Testing. Washington, D.C. : Federal Aviation Administration, 2007. Technical Report.

18. Simmons, Jeffery, Erlich, David and Shockey, Donald. 2004. Explicit Finite Element Modeling of Multilayer Composite Fabric for Gas Turbine Engine Containment Systems Part 3: Model Development and Simulation of Experiments. Washington D.C. : Federal Aviation Administration, 2004. Technical Report.

19. Stahlecker, Zach K. 2007. The Development of a Fabric Material Model for use in Modeling Engine Containment Systems. Arizona State University : M.S. Thesis, 2007.

20. Vaidya, Aditya S. 2010. Improvement in Modeling Techniques for Fabric-Based Aircraft Engine Containment Systems. Tempe, AZ : Arizona State University, 2010. Masters Thesis.

21. Vaidya, Aditya S. 2011. Improvement in Modeling Techniques for Fabric-Based Engine Aircraft Containment. Arizona State University : M.S. Thesis, 2011.

22. Zhu, Deju. 2009. Experimental Study and Finite Element Modeling of Woven Fabrics. Tempe, AZ : Arizona State University, 2009. Doctoral Dissertation.

APPENDIX A

MATLAB ROUTINE TO PROCESS DATA FROM PENETRATOR TESTING

```
%%%%%%%%%%%%%%%%%%%%%%%%%%%%%%%%%%%%%%%%%%%%%%%%%%%%%%%%%%%%%%%%%
%%%%%%%%%%
% Process raw data
% modified by Jonathan Fein
%%%%%%%%%%%%%%%%%%%%%%%%%%%%%%%%%%%%%%%%%%%%%%%%%%%%%%%%%%%%%%%%%
%%%%%%%%%
clear all;
% input data files
File = 'DL04_0522';

f1=strcat(File,'.dat');  % First Input file name
f2=strcat(File,'-smoothed.dat');
f3=strcat(File,'-interpolated.dat');
f4=strcat(File,'-results.dat');

gage_length= 8;
% width = 0.75;
% thickness = 0.145;

Area_yarn =1.78e-4; % area of one yarn, in^2
Num_yarn = 34; % number of yarn
Area = Area_yarn*Num_yarn; % crossing area of specimen
%   Area = width * thickness;

Alldata = load(f1);
time1=Alldata(:,1);
stroke1=Alldata(:,2);
load1=Alldata(:,3);

load1 = load1-load1(1);
stroke1 = stroke1-stroke1(1);

%n=4;
load = smooth5(load1');   % smooth the data points of load and
stroke/displacement
stroke = smooth5(stroke1');

newdata=zeros(max(size(load)),3);
newdata(1:end,1) = load(:,1);
newdata(1:end,2) = stroke(:,1);
newdata(1:end,3) = time1(:,1);

% write a file recording new processed data
fid2 = fopen(f2,'w');
fprintf(fid2,'%12.8d  %12.8d  %12.8d\n',newdata');
fclose(fid2);

[maxload, coun1]=max(load);
dispmaxload = stroke(coun1);

fid3 = fopen(f4,'w');
fprintf(fid3,'Specimen name,        %12s \n',File);%
fprintf(fid3,'Maximum load, f,lb   %12.4f \n',maxload);%
fprintf(fid3,'Disp. at max load, in %12.4f \n',dispmaxload);%
```

```
function xx = smooth5(x)

xx(1) = x(1);
xx(2) = x(2);

for j= 3:max(size(x))-2
xx(j) = 1/5*(x(j-2)+x(j-1)+x(j)+x(j+1)+x(j+2));
end

xx(max(size(x))-1) = x(max(size(x))-1);
xx(max(size(x))) = x(max(size(x)));


xx = xx';
```

APPENDIX B

KEYWORD CARDS FOR REPRESENTATIVE FAA NUMERICAL MODEL

```
*CONTACT_AUTOMATIC_SURFACE_TO_SURFACE
$#    ssid      msid     sstyp     mstyp    sboxid    mboxid       spr       mpr
         1         2         3         3
$#      fs        fd        dc        vc       vdc    penchk        bt        dt
     0.100     0.100                        20.000
$#     sfs       sfm       sst       mst      sfst      sfmt       fsf       vsf

$#    soft    sofscl    lcidab    maxpar     sbopt     depth     bsort    frcfrq
         2
$#  penmax    thkopt    shlthk     snlog      isym     i2d3d    sldthk    sldstf
                   0
$#    igap    ignore
*CONTACT_AUTOMATIC_SURFACE_TO_SURFACE
$#    ssid      msid     sstyp     mstyp    sboxid    mboxid       spr       mpr
         3         2         3         3
$#      fs        fd        dc        vc       vdc    penchk        bt        dt
     0.100     0.100                        20.000
$#     sfs       sfm       sst       mst      sfst      sfmt       fsf       vsf

$#    soft    sofscl    lcidab    maxpar     sbopt     depth     bsort    frcfrq
         2
$#  penmax    thkopt    shlthk     snlog      isym     i2d3d    sldthk    sldstf
                   0
$#    igap    ignore

*CONTACT_AUTOMATIC_SURFACE_TO_SURFACE
$#    ssid      msid     sstyp     mstyp    sboxid    mboxid       spr       mpr
         4        11         3         3
$#      fs        fd        dc        vc       vdc    penchk        bt        dt
     0.100     0.100                        10.000
$#     sfs       sfm       sst       mst      sfst      sfmt       fsf       vsf

$#    soft    sofscl    lcidab    maxpar     sbopt     depth     bsort    frcfrq
         2
$#  penmax    thkopt    shlthk     snlog      isym     i2d3d    sldthk    sldstf
                   0
$#    igap    ignore

*CONTACT_AUTOMATIC_SURFACE_TO_SURFACE
$#    ssid      msid     sstyp     mstyp    sboxid    mboxid       spr       mpr
         4        12         3         3
$#      fs        fd        dc        vc       vdc    penchk        bt        dt
     0.100     0.100                        10.000
$#     sfs       sfm       sst       mst      sfst      sfmt       fsf       vsf

$#    soft    sofscl    lcidab    maxpar     sbopt     depth     bsort    frcfrq
         2
$#  penmax    thkopt    shlthk     snlog      isym     i2d3d    sldthk    sldstf
                   0
$#    igap    ignore
*CONTACT_AUTOMATIC_SURFACE_TO_SURFACE
$#    ssid      msid     sstyp     mstyp    sboxid    mboxid       spr       mpr
         5        11         3         3
$#      fs        fd        dc        vc       vdc    penchk        bt        dt
     0.100     0.100                        10.000
$#     sfs       sfm       sst       mst      sfst      sfmt       fsf       vsf

$#    soft    sofscl    lcidab    maxpar     sbopt     depth     bsort    frcfrq
         2
$#  penmax    thkopt    shlthk     snlog      isym     i2d3d    sldthk    sldstf
                   0
$#    igap    ignore

*CONTACT_AUTOMATIC_SURFACE_TO_SURFACE
$#    ssid      msid     sstyp     mstyp    sboxid    mboxid       spr       mpr
         5        12         3         3
$#      fs        fd        dc        vc       vdc    penchk        bt        dt
     0.100     0.100                        10.000
$#     sfs       sfm       sst       mst      sfst      sfmt       fsf       vsf
```

```
$#    soft    sofscl    lcidab    maxpar     sbopt     depth     bsort    frcfrq
         2
$#  penmax    thkopt    shlthk     snlog      isym     i2d3d    sldthk    sldstf
                   0
$#    igap    ignore

*CONTACT_AUTOMATIC_SURFACE_TO_SURFACE
$#    ssid      msid     sstyp     mstyp    sboxid    mboxid       spr       mpr
         5         4         3         3
$#      fs        fd        dc        vc       vdc    penchk        bt        dt
     0.200     0.200                        10.000
$#     sfs       sfm       sst       mst      sfst      sfmt       fsf       vsf

$#    soft    sofscl    lcidab    maxpar     sbopt     depth     bsort    frcfrq
         2
$#  penmax    thkopt    shlthk     snlog      isym     i2d3d    sldthk    sldstf
                   0
$#    igap    ignore

*CONTACT_AUTOMATIC_SURFACE_TO_SURFACE
$#    ssid      msid     sstyp     mstyp    sboxid    mboxid       spr       mpr
         3         1         3         3
$#      fs        fd        dc        vc       vdc    penchk        bt        dt
     0.200     0.200                        20.000
$#     sfs       sfm       sst       mst      sfst      sfmt       fsf       vsf

$#    soft    sofscl    lcidab    maxpar     sbopt     depth     bsort    frcfrq
         2
$#  penmax    thkopt    shlthk     snlog      isym     i2d3d    sldthk    sldstf
                   0
$#    igap    ignore

*CONTROL_TIMESTEP
0.,0.75

*CONTROL_TERMINATION
3.0E+00,0,0.000E+00,0.000E+00,0.000E+00

*CONTROL_SHELL
$ WRPANG   ESORT   IRNXX  ISTUPD  THEORY   BWC   MITER   PROJ
   20,        0,     -1,     0,      2,      1,     1,     0

*CONTROL_ACCURACY
$ osu   inn
   1,    2

*CONTROL_ENERGY
$ hgen    rwen    slnten   rylen
  2,    2,   2,   2

*CONTROL_CONTACT
$   slsfac    rwpnal    islchk    shlthk    penopt    thkcng     orien
               0.000                   1
$   usrstr    usrfrc     nsbcs    interm     xpene     ssthk      ecdt   tiedprj

$    sfric     dfric       edc       vfc        th     th_sf    pen_sf

$   ignore    frceng   skiprwg    outseg   spotstp   spotdel   spothin

*DATABASE_BINARY_D3PLOT
$       dt
      0.05         0

*DATABASE_MATSUM
$       dt    binary
      0.05

*DATABASE_GLSTAT
$       dt
      0.05
```

```
*DATABASE_EXTENT_BINARY
$  neiph   neips   maxint    strflg    sigflg    epsflg    rltflg   engflg
     0,     18,      1,        1,        0,        0,        0,       0
$  cmpflg   ieverp   beamip   dcomp   shge   stssz   n3thdt
     1,      0,         0,        0,      1,       0,       0

*CONTACT_TIEBREAK_NODES_ONLY
1,1,4,3
0.2,0.2,0,0,20.0
0,0,0,0
50e-5,100e-5,2,2

*CONTACT_TIEBREAK_NODES_ONLY
2,2,4,3
0.1,0.1,0,0,20.0
0,0,0,0
5e-5,10e-5,2,2

*MAT_USER_DEFINED_MATERIAL_MODELS
$      mid        ro        mt       lmc       nhv    iortho     ibulk        ig
         2   7.48E-5        48        32        20         1         1         1
$    ivect     ifail    itherm    ihyper      ieos
         0         1
$     aopt      maxc        xp        yp        zp        a1        a2        a3
         3
$       v1        v2        v3        d1        d2        d3      beta
   -0.2588         0    0.9659
$       Ex        Ey   Excrfac   Eycrfac Exsoftfac Eysoftfac   Eunlfac  Ecompfac
      4.68      4.68      0.06      0.20      -2.2      -5.6       1.5     0.005
$      Gyz       Gzx      Gxy1      Gxy2      Gxy3  gammaxy1  gammaxy2     ecrpx
      0.05      0.05    6.0e-4    6.0e-3    5.0e-2     0.250     0.350    0.0070
$    ecrpy     emaxx     emaxy   sigpost    efailx    efaily      C(E)      P(E)
    0.0025    0.0223    0.0201     0.010       0.2       0.2     0.005      40.0
$     C(e)      P(e)      dfac    fail_e      NONE      NONE      NONE      NONE
     0.005      40.0       0.3      0.35

*HOURGLASS
$     hgid       ihq        qm       ibq        q1        q2        qb        qw
         2         4       0.1         0       0.0       0.0       0.1       0.1

*SECTION_SHELL
1,2,8.333E-01,1.000E+00,0.000E+00,0.000E+00,0
0.022,0.022,0.022,0.022,0.000E+00

*PART
projectile
11,11,11,11,11,0

*PART
projectile
12,12,12,12,12,0

*PART
fabric1
1,1,2,0,1,0

*PART
ring
2,2,1,1,2,0

*PART
fabric2
3,1,2,0,1,0

*PART
fabric_flat1
4,1,2,0,1,0

*PART
```

```
fabric_flat2
5,1,2,0,1,0

*INITIAL_VELOCITY_GENERATION
$ id   styp  omega   vx   vy   vz
   11,   2,    0.,03.700,  0,  0
$  xc   yc   zc   nx   ny   nz   phase
    0,   0,   0,   1,   0,   0,   0

*INITIAL_VELOCITY_GENERATION
$ id   styp  omega   vx   vy   vz
   12,   2,    0.,03.700,  0,  0
$  xc   yc   zc   nx   ny   nz   phase
    0,   0,   0,   1,   0,   0,   0
```

APPENDIX C

LS-DYNA KEYWORD DESCRIPTION FOR MAT234 *MAT_VISCOELASTIC_LOOSE_FABRIC

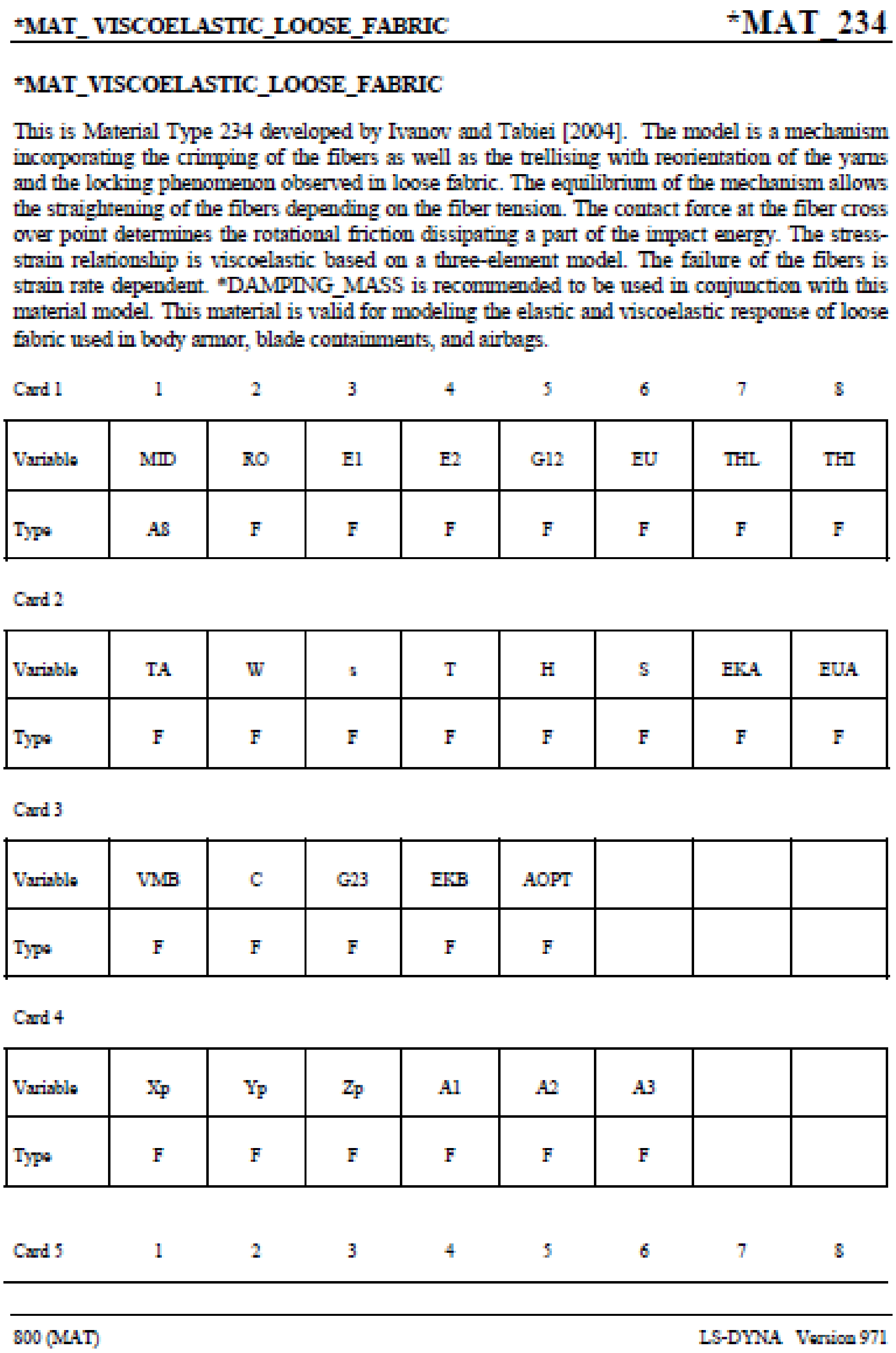

***MAT_ VISCOELASTIC_LOOSE_FABRIC** ***MAT_234**

*MAT_VISCOELASTIC_LOOSE_FABRIC

This is Material Type 234 developed by Ivanov and Tabiei [2004]. The model is a mechanism incorporating the crimping of the fibers as well as the trellising with reorientation of the yarns and the locking phenomenon observed in loose fabric. The equilibrium of the mechanism allows the straightening of the fibers depending on the fiber tension. The contact force at the fiber cross over point determines the rotational friction dissipating a part of the impact energy. The stress-strain relationship is viscoelastic based on a three-element model. The failure of the fibers is strain rate dependent. *DAMPING_MASS is recommended to be used in conjunction with this material model. This material is valid for modeling the elastic and viscoelastic response of loose fabric used in body armor, blade containments, and airbags.

Card 1	1	2	3	4	5	6	7	8
Variable	MID	RO	E1	E2	G12	EU	THL	THI
Type	A8	F	F	F	F	F	F	F

Card 2

Variable	TA	W	s	T	H	S	EKA	EUA
Type	F	F	F	F	F	F	F	F

Card 3

Variable	VMB	C	G23	EKB	AOPT			
Type	F	F	F	F	F			

Card 4

Variable	Xp	Yp	Zp	A1	A2	A3		
Type	F	F	F	F	F	F		

Card 5	1	2	3	4	5	6	7	8

800 (MAT) LS-DYNA Version 971

Variable	V1	V2	V3	D1	D2	D3		
Type	F	F	F	F	F	F		

VARIABLE	DESCRIPTION
MID	Material identification. A unique number or label not exceeding 8 characters must be specified.
RO	Mass density.
E1	E_1, Young's modulus in the yarn axial-direction.
E2	E_2, Young's modulus in the yarn transverse-direction.
G12	G_{12}, Shear modulus of the yarns.
EU	Ultimate strain at failure.
THL	Yarn locking angle.
THI	Initial brade angle.
TA	Transition angle to locking.
W	Fiber width.
S	Span between the fibers.
T	Real fiber thickness.
H	Effective fiber thickness.
S	Fiber cross-sectional area.
EKA	Elastic constant of element "a".
EUA	Ultimate strain of element "a".
VMB	Damping coefficient of element "b".
C	Coefficient of friction between the fibers.

VARIABLE	DESCRIPTION
G23	transverse shear modulus.
Ekb	Elastic constant of element "b"
AOPT	Material axis option

Remarks:

The parameters of the Representative Volume Cell (RVC) are: the yarn span, s, the fabric thickness, t, the yarn width, w, and the yarn cross-sectional area, A. The initially orthogonal yarns (see Fig. 2a) are free to rotate (see Fig. 2b) up to some angle and after that the lateral contact between the yarns causes the locking of the trellis mechanism and the packing of the yarns (see Fig. 2c).The minimum braid angle, $\theta_{\min}$, can be calculated from the geometry and the architecture of the fabric material having the yarn width, w, and the span between the yarns, s:

$$\sin(2\theta_{\min}) = \frac{w}{s}$$

The other constrain angles as the locking range angle, θ_{lock}, and the maximum braid angle, $\theta_{\max}$, (see Fig) are easy to be determined then:

$$\theta_{lock} = 45° - \theta_{\min}\ ,\quad \theta_{\max} = 45° + \theta_{lock}$$

The material behavior of the yarn can be simply described by a combination of one Maxwell element without the dashpot and one Kelvin-Voigt element. The 1-D model of viscoelasticity is shown in the following figure. The differential equation of viscoelasticity of the yarns can be derived from the model equilibrium as in the following equation:

$$\left(K_a + K_b\right)\sigma + \mu_b\dot{\sigma} = K_a K_b \varepsilon + \mu_b K_a \dot{\varepsilon}$$

The input parameters for the viscoelasticity model of the material are only the static Young's modulus E_1, the Hookian spring coefficient (EKA) K_a, the viscosity coefficient (VMB) μ_b, the static ultimate strain (EU) $\varepsilon_{\max}$, and the Hookian spring ultimate strain (EUA) $\varepsilon_{a\max}$. The other parameters can be obtained as follows:

$$K_b = \frac{K_a E_1}{K_a - E_1}$$

$$\varepsilon_{b\max} = \frac{K_a - E_1}{K_a}\varepsilon_{\max}$$

Applying the Eq. (18) for the fill and the warp yarns, we obtain the stress increments in the yarns, $\Delta\sigma_f$ and $\Delta\sigma_w$. The stress in the yarns is updated for the next time step:

$$\sigma_f^{(n+1)} = \sigma_f^{(n)} + \Delta\sigma_f^{(n)}\,, \quad \sigma_w^{(n+1)} = \sigma_w^{(n)} + \Delta\sigma_w^{(n)} \tag{38}$$

We can imagine that the RVC is smeared to the parallelepiped in order to transform the stress acting on the yarn cross-section to the stress acting on the element wall. The thickness of the membrane shell element used should be equal to the effective thickness, t_e , that can be found by dividing the areal density of the fabric by its mass density. The in-plane stress components acting on the RVC walls in the material direction of the yarns are calculated as follows for the fill and warp directions:

$$\sigma_{f11}^{(n+1)} = \frac{2\sigma_f^{(n+1)} S}{s\,t_e}\,, \quad \sigma_{w11}^{(n+1)} = \frac{2\sigma_w^{(n+1)} S}{s\,t_e}$$

$$\sigma_{f22}^{(n+1)} = \sigma_{f22}^{(n)} + \alpha E_2\,\Delta\varepsilon_{f22}^{(n)}\,, \quad \sigma_{w22}^{(n+1)} = \sigma_{w22}^{(n)} + \alpha E_2\,\Delta\varepsilon_{w22}^{(n)}$$

$$\sigma_{f12}^{(n+1)} = \sigma_{f12}^{(n)} + \alpha G_{12}\,\Delta\varepsilon_{f12}^{(n)}\,, \quad \sigma_{w12}^{(n+1)} = \sigma_{w12}^{(n)} + \alpha G_{12}\,\Delta\varepsilon_{w12}^{(n)}$$

where E_2 is the transverse Young's modulus of the yarns, G_{12} is the longitudinal shear modulus, and α is the lateral contact factor. The lateral contact factor is zero when the trellis mechanism is open and unity if the mechanism is locked with full lateral contact between the yarns. There is a transition range, $\Delta\theta$ *(TA)*, of the average braid angle θ in which the lateral contact factor, α, is a linear function of the average braid angle. The graph of the function $\alpha(\theta)$ is shown in Fig. 4.

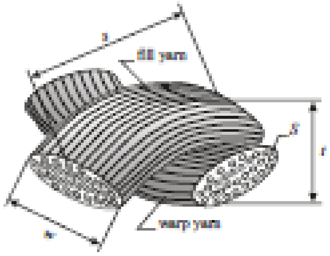

Fig. 1. Representative Volume Cell (RVC) of the model

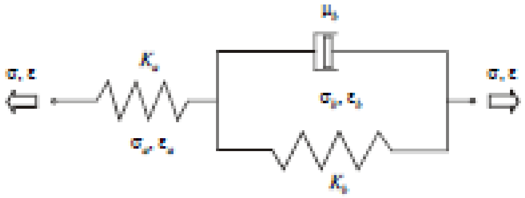

Fig. 2. Three-element viscoelasticity model

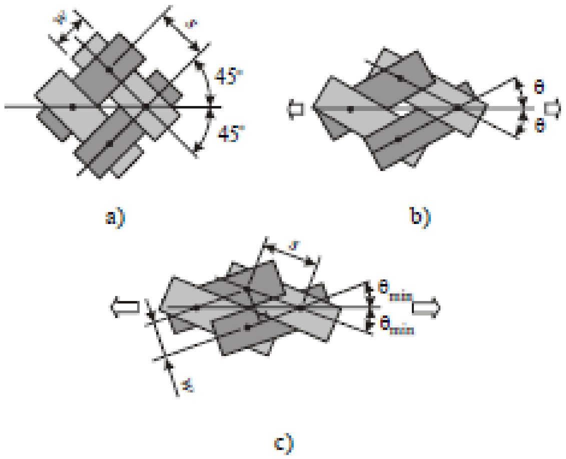

Fig. 3. Plain woven fabric as trellis mechanism: a) initial state; b) slightly stretched in bias direction; c) stretched to locking.

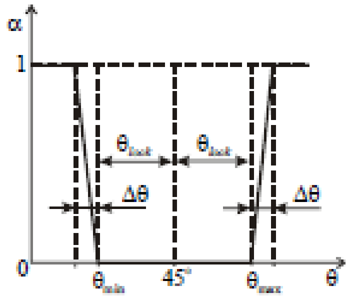

Fig. 4. The lateral contact factor as a function of average braid angle θ.